Interface Defeat of Long Rods Impacting Oblique Silicon Carbide

Charles E. Anderson, Jr.
Thilo Behner
Timothy J. Holmquist
Nikki L. King
Dennis L. Orphal

Contract: W56HZV-06-C-0194

SwRI® Report 18.12544/029

Prepared for:

US Army RDECOM-TARDEC
RDTA-RS
Warren, MI 43897-5000

February 2011

REPORT DOCUMENTATION PAGE	*Form Approved* OMB No. 0704-0188

1. REPORT DATE *(DD-MM-YYYY)* 28-02-2011	**2. REPORT TYPE** Technical	**3. DATES COVERED** *(From - To)* July 2009 – February 2011

4. TITLE AND SUBTITLE Interface Defeat of Long Rods Impacting Oblique Silicon Carbide	**5a. CONTRACT NUMBER** W56HZV-06-C-0194
	5b. GRANT NUMBER
	5c. PROGRAM ELEMENT NUMBER
6. AUTHOR(S) Charles E. Anderson, Jr.[1], Thilo Behner[2], Timothy J. Holmquist[3], Nikki L. King[1], and Dennis L. Orphal[4]	**5d. PROJECT NUMBER** 18.12544
	5e. TASK NUMBER
	5f. WORK UNIT NUMBER
7. PERFORMING ORGANIZATION NAME(S) AND ADDRESS(ES) [1]Southwest Research Institute, P. O. Drawer 28510, San Antonio, TX 78228-0510; [2]Fraunhofer Institut fur Kurzzeitdynamik (Ernst-Mach-Institut), Eckerstr. 4, 29104 Freiburg, Germany [3]Southwest Research Institute, 5353 Wayzata Blvd, Minneapolis, MN 55416 [4]International Research Associates, Inc., 4450 Black Ave, Pleasanton, CA 94566	**8. PERFORMING ORGANIZATION REPORT NUMBER** 18.12544/029
9. SPONSORING/MONITORING AGENCY NAME(S) AND ADDRESS(ES) US Army Tank-Automotive Research, Development, and Engineering Center, Warren, MI 48397-5000	**10. SPONSOR/MONITOR'S ACRONYM(S)** RDECOM-TARDEC/RDTA-RS
	11. SPONSORING/MONITORING AGENCY REPORT NUMBER

12. DISTRIBUTION AVAILABILITY STATEMENT

Approved for Public Release; Unlimited Distribution

13. SUPPLEMENTARY NOTES

The views, opinion, and/or findings contained in this report are those of the authors and should not be construed as an official Department of the Army position, policy, or decision, unless so designated by other documents.

14. ABSTRACT

Test data for gold rods impacting unconfined silicon carbide targets are reported. This work focuses on the dwell phenomenon exhibited by silicon carbide for targets at obliquity. Experiments are presented for obliquities of 30°, 45°, and 60°, with and without cover plates. Results are compared to normal impact.

15. SUBJECT TERMS

silicone carbide, penetration velocity, dwell, interface defeat, buffer, ceramics, obliquity

16. SECURITY CLASSIFICATION OF:			**17. LIMITATION OF ABSTRACT**	**18. NUMBER OF PAGES**	**19a. NAME OF RESPONSIBLE PERSON** Frederick C. Rickert
a. REPORT Unlimited	**b. ABSTRACT** Unlimited	**c. THIS PAGE** Unlimited	None	138	**19b. TELEPHONE NUMBER (*Include area code*)** 586-282-3914

Table of Contents

Page

List of Figures

List of Figures (Cont'd)

List of Tables

1.0 Introduction

Southwest Research Institute (SwRI) has been investigating the penetration response of silicon carbide (SiC) since approximately 2003. Experimental work initially focused on an attempt to detect the presence of the so-called failure wave, which had been observed in flyer-plate impact experiments, e.g., Refs. [1-4]. There was an indication that a failure wave was observed in penetration experiments of SiC [5], but results from two different research efforts were combined to reach this conclusion. Therefore, a research effort was undertaken to validate the findings of Ref. [5] using a single set of consistent experiments [6-8]. A series of reverse ballistic experiments were conducted with impact velocities between 2.0 and 6.2 km/s [9]. Gold rods were suspended and SiC-N targets were launched at a suspended gold penetrator. Position versus time and rod length versus time was determined by flash radiography. Although no evidence of a failure wave was found over the velocity range studied [10], the experimental data provided fundamental information on the penetration and consumption velocities of a gold rod penetrating silicon carbide [9].

Next, SwRI investigated penetration of intact and predamaged ceramic, including SiC powder [11-12]. Further experimental work was conducted to address questions raised by results of these experiments [13-15]. These efforts also provided data that permitted examination of numerical simulations of penetration into SiC [16-17].

During this time, interest developed in obtaining a better understanding of dwell and interface defeat. Hauver, *et al.*, were the first to investigate dwell with long rods [18-22], although the phenomenon of dwell had been observed by Wilkins while conducting small-arms experiments [23]. Dwell occurs when a high-velocity projectile flows out radially with no significant penetration. Dwell can occur on a target surface as well as inside a target. Interface defeat is dwell that occurs on a well-defined boundary, either the initial target surface or an interior boundary between two different materials. Dwell and interface defeat can be partial or complete; however, interface defeat is generally reserved for cases where the projectile is complete (or almost completely) eroded at the interface.

As the impact velocity is increased, there is a point at which dwell is not maintained and penetration occurs; this impact velocity is called the dwell-penetration transition velocity, V_t, and is a function of the projectile materials, the projectile configuration, impact velocity, and the target material and configuration. The phenomenon of interface defeat, and in particular, the transition velocity from dwell to penetration, is not well understood.

Hauver, *et al*.'s work focused on heavily confined targets, as did Lundberg, *et al.* [24-29]. It was decided to examine unconfined targets, i.e., no side/radial plate and no prestress, with a focus to establish the dwell-penetration transition velocity, and thus, the maximum surface stress the ceramic can resist before the on-set of penetration. This transition stress becomes, in essence, a "material property" of the ceramic. The transition stress is an important material characteristic that can be used to compare one ceramic to another. Experiments were again conducted in a reverse ballistics mode using a gold penetrator [30-33]. It was recognized that elimination of the stress associated with the impact shock could increase the dwell-penetration transition velocity [30-31], so experiments were also conducted with copper buffers [32-33].

Holmquist, *et al*. [34], provide a summary of the experimental results and supporting numerical simulations.[1]

Stable dwell, using the 1.0-mm diameter Au rod, was possible for impact velocities up to approximately 825 m/s on bare SiC ceramic; the transition impact velocity increased to approximately 1550 m/s when a copper buffer was used.

All results to date were experiments conducted at normal obliquity. Thus, a test series was designed to investigate the influence of impact obliquity on the transition velocity. Obliquity angles ranged from 30° to 60°, the impact velocities varied between 900 m/s and 1650 m/s for bare and buffered ceramics. The results are summarized and compared to normal obliquity experiments.

In addition to defining a more precise transition velocity for bare (no copper buffer) ceramic, the effect of scale size on the dwell-transition velocity was examined [15], first reported by Andersson, *et al*. [29]. The results are consistent with the observations by Andersson, *et al.* [29].

---

[1] Overlapping the study of dwell and interface defeat of SiC, Anderson, et al. [35-36] determined the transition velocities of bare and buffered borosilicate glass targets. Although different materials, the experimental studies on SiC and borosilicate glass are complementary.

2.0 Experimental Setup

2.1 Test Setup

Figure 1 shows the test setup for the reverse ballistic experiments. All tests were performed with a powder gun. Interface defeat and penetration were observed with five 180-kV flash X-rays arranged rotationally symmetric in the plane of impact. Additionally, a high-speed video camera monitored the impact process optically. That camera took video sequences with an interframe time of 2 µs and an exposure time per frame of 0.5 µs.

The ceramic samples were SiC-N cylinders (density $\rho_t = 3.2$ g/cm^3) from BAE Systems, Advanced Ceramics Division (formerly CERCOM), with a diameter of 20 mm and an oblique section of either 30°, 45° or 60° (Fig. 2). All different obliquities maintained the equivalent volume of the standard right circular cylinder ceramic with a centerline length of 35 mm.

The pure gold rods had a diameter of 1.0 mm and a length of 70 mm (density $\rho_p =$ 19.3 g/cm^3; hardness 65 HV5; ultimate tensile strength of 220 MPa and elongation 30 %). The front buffers were made from copper (E-Cu-57) and were glued to the front face with an epoxy resin. The bonding gap was below measuring accuracy (< 10 µm). The buffers covered the full front face and had a height of 2 mm perpendicular to the surface; e.g., for the 60° obliquity, the buffer had a line-of-sight thickness of 4 mm.

As the time measurements for the flash X-ray pictures are very accurate (up to better than ±5 ns), the uncertainty of the velocities determined from the X-ray pictures is due to the error in the position measurement, which is ±0.1 mm to ±0.15 mm.

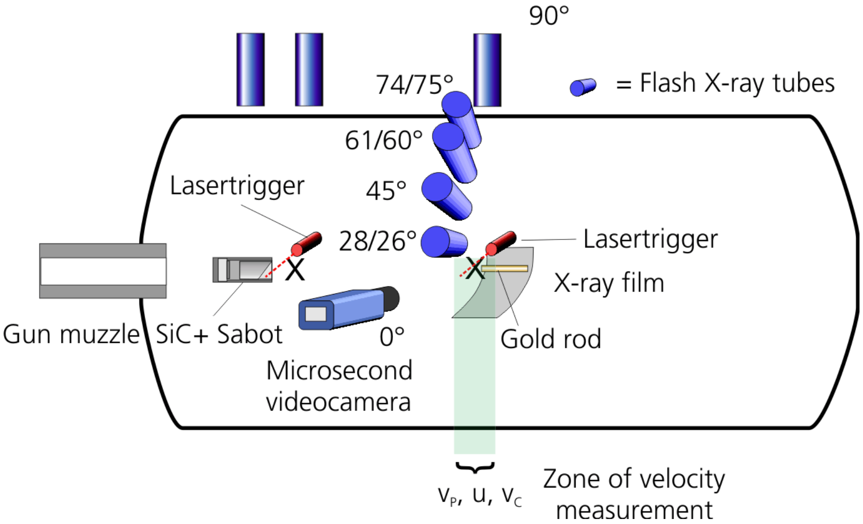

Figure 1. Test setup inside blast chamber.

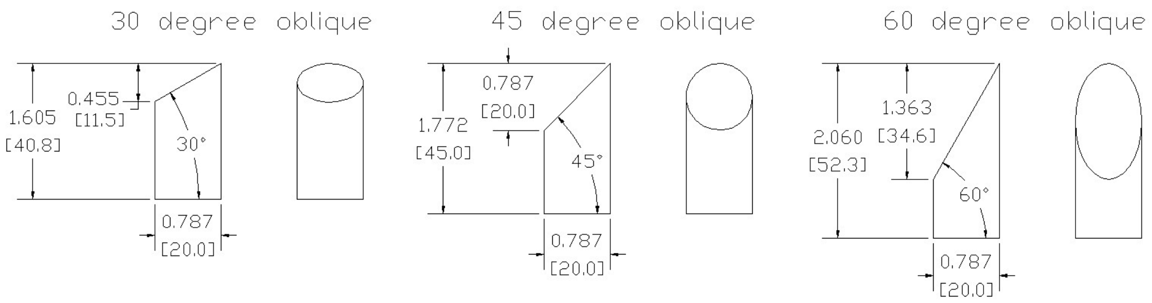

(a) Target dimensions (dimensions in inches with mm in brackets).

(b) Photograph of targets with cover plates.

Figure 2. Target configurations.

2.2 Sabot Design

The sabot design used for launching the ceramic consists of an inner one-piece polycarbonate sleeve, into which the ceramic is inserted (see the left image in Fig. 3). A four-piece separating outer polycarbonate sleeve (second image in Fig. 3) surrounds the inner polycarbonate sleeve. The middle image is a rubber isolator to help cushion the inner polycarbonate layer during launch. This is followed by the pusher plate and then the obturator (far right image). The assembled sabot, after separation of the outer sleeve, is seen in the left flash X-ray shadowgraph in Fig. 4. The purpose of the inner sleeve is to avoid additional yaw of the oblique ceramic during free flight conditions. The right X-ray shadowgraph in Fig. 4 shows the effect of a sabot design without an inner sleeve. Due to aerodynamic drag, a 60° target (in this case made of aluminum) develops a yaw angle of 60° after the sabot parts separate.

Figure 3. Sabot design.

Figure 4. Flight stability with (left) and without (right) inner polycarbonate sleeve.

3.0 Experimental Results

3.1 Experimental Data

An example of the flash X-ray data is shown in Fig. 5. Time “0” is the time that the rod reaches the cover plate, or if no cover, the ceramic surface. It is straightforward to calculate the time of impact onto the cover plate from the measured rod distance divided by the impact velocity.

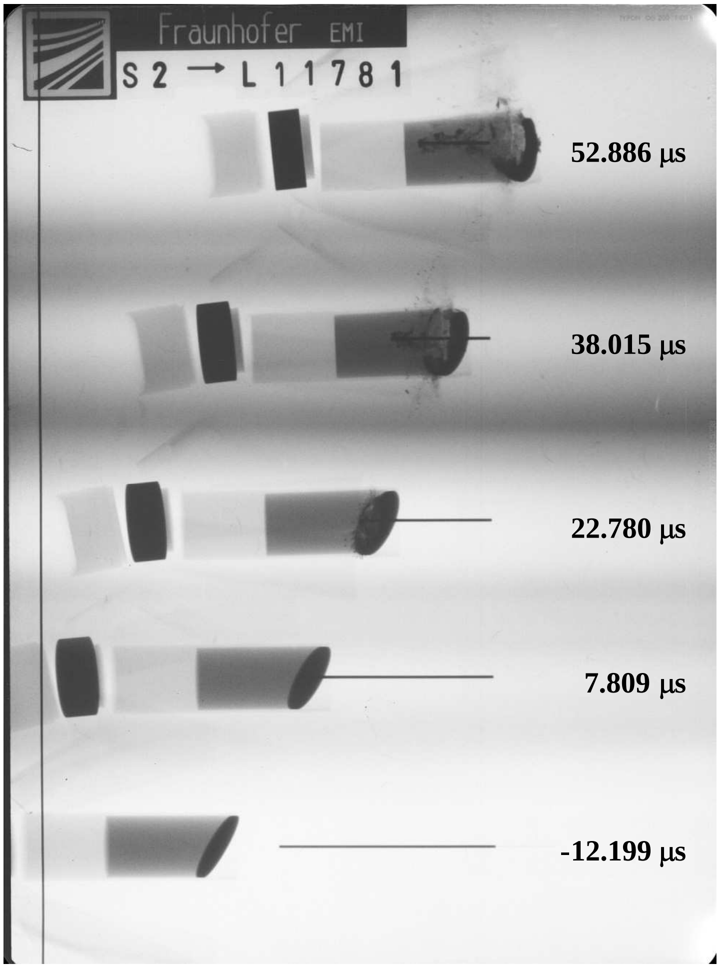

Figure 5. Example of flash X-ray data.

Measurements from the flash X-rays were done according to Fig. 6. Since S_1, S_2 and S_3 are independent measurements, a consistency check is that $S_2 + S_3 = S_1$. Penetration depth is measured from the rear of the ceramic target, as shown in Fig. 6.

All experiments are listed by obliquity angle in Table 1. Test results are sorted by increasing impact velocity v_p for each group. For each test, the yaw angle of the target is given in Table 1. Because the X-rays are positioned in an arc around the suspended rod (see Fig. 1), it is possible to calculate the direction and distance of an off-centered impact, designated “oc” in Table 1 (and shown in Fig. 7).

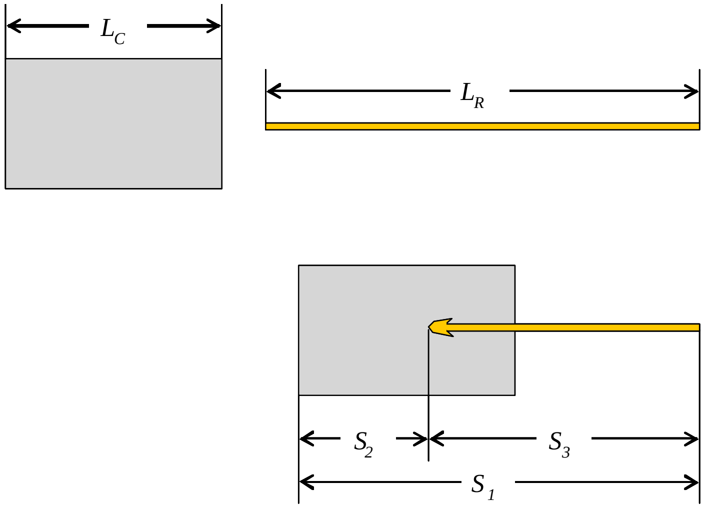

Figure 6. Definitions for X-ray measurements.

Table 1. Experimental Results

Exp.	Target [°]	Yaw [°]	oc [mm]	v_p [km/s]	u [km/s]	v_c [km/s]	t_D [μs]	L_{eff} [mm]
11790	30	2.4	1.9	1.419	-	1.327	>39	34.3
11784[a]	30	7.0	2.2	1.433	0.616	-	29	33.9
11783	30	1.9	4.4	1.479	0.718	0.743	28	32.8
11791[b]	30	2.5	2.0	1.481	0.596	0.871	4	33.9
11793	30	1.5	3.1	1.499	0.649	-	27	33.7
11781	30	1.5	3.9	1.514	0.594	0.663	5	35.0
11794	30	0.9	1.8	1.529	-	1.429	>39	34.1
11796	30	2.6	3.5	1.529	0.773	0.776	12	34.6
11780	30	6.1	2.8	1.548	0.813	0.752	7	33.7
11795	30	3.0	0.0	1.552	0.713	-	11	35.0
11779	30	6.9	2.2	1.588	0.915	0.666	4	33.9
11821	45	2.5	4.5	1.434	0.709	0.677	19	32.3
11805	45	0.6	4.5	1.522	-	1.439	>34	30.7
11798	45	0.7	3.5	1.535	0.453	-	24	31.5
11802	45	1.7	0.9	1.545	0.654	0.888	11	34.2
11797	45	2.0	2.4	1.568	0.740	-	23	32.7
11818	45	3.0	3.9	1.593	-	1.464	>35	31.1
11930	45 bare	2.1	1.0	0.928	-	0.904	76	34.7
11928	45 bare	1.9	3.1	1.015	-	1.087	46	32.2
11933	45 bare	2.1	2.1	1.024	-	1.041	38	33.2
11932	45 bare	3.1	0.5	1.070	-	1.076	42	34.5
11931	45 bare	2.0	1.0	1.128	0.538	0.582	25	34.1
11929	45 bare	0.8	2.5	1.191	0.570	0.605	23	32.5
11934	45 bare	0.5	1.6	1.292	0.555	0.724	12	33.4

---

a: experiment with high yaw

b: cover plate separated before impact

Table 1 (Cont'd). Experimental Results

Exp.	Target [°]	Yaw [°]	oc [mm]	v_p [km/s]	u [km/s]	v_c [km/s]	t_D [μs]	L_{eff} [mm]
11819	60	1.6	2.3	1.430	0.670	0.789	7	36.3
11804	60	1.1	2.2	1.497	0.748	0.711	12	31.6
11803	60	0.7	1.3	1.522	0.580	0.918	10	33.0
11800	60	1.0	4.3	1.537	0.636	-	19	27.6
11801	60	0.8	4.9	1.548	0.663	-	21	26.9
11799	60	0.7	0.9	1.570	0.692	0.852	17	33.7
11817	60	2.4	2.4	1.569	0.896	0.694	9	37.7
11820[c]	60	2.8	1.3	1.613	0.581	0.926	5	33.0
11807	60 bare	2.7	2.4	0.921	-	0.923	76	32.1
11808	60 bare	2.8	3.0	0.932	-	0.920	75	30.7
11809	60 bare	4.0	2.6	1.008	-	0.989	70	33.8
11810	60 bare	6.4	1.9	1.067	-	1.019	66	37.0
11812	60 bare	4.4	3.1	1.162	-	1.106	60	37.9
11814	60 bare	4.6	3.9	1.408	-	1.330	50	33.7
11815	60 bare	3.2	0.9	1.515	0.757	0.745	20	33.7
11822[d]	60 bare	2.7	1.7	1.650	0.815	-	22	32.3
11811[e]	0 bare	0.0	4.4	0.883	-	0.873	64[+]	35.0
11816	0 bare	1.1	2.2	0.978	0.276	0.670	26	35.0

c: 4 mm thick cover plate (8 mm LOS thickness) – see Section 4.4
d,e: polycarbonate cover on ceramic – see Section 4.4
+: complete dwell with 13.1 mm shorter rod due to erosion in PC cover (Section 4.4)

Due to the obliquity of the target, off-centered impacts affect the time of impact, as well as the calculated penetration depth. The off-centered impacts are shown schematically in Fig. 7, where the off-centered distance d_{oc} can be positive or negative, depending upon whether it is to the left or right (as shown in the figure) of the centerline. The adjustment to the impact time, Δt_{adj} is given by:

$$\Delta t_{adj} = \frac{d_{oc}}{\mathrm{v}_p} \tag{1}$$

The times listed in Table A-1 in the Appendix account for the adjusted time. The penetration depth P is calculated from the length of the ceramic, L_C, and the distance measured from the rear of the target (S_2), but modified by the off-centered hit distance:

$$P = L_C - S_2 - d_{oc} = L_{eff} - S_2 \tag{2}$$

where the effective length of the ceramic, L_{eff}, is given by $L_C - d_{oc}$. L_{eff} is listed in Table 1.[2]

The measured penetration depths, as adjusted by Eqn. (2), along with the adjusted flash X-ray times are listed in Tables A-2 through A-4 for the three impact obliquities. The penetration depths and impact times did not need to be adjusted for Table A-5 since these were 0° impacts. The position-time and rod length-time results for the Fig. 5 flash X-ray data are shown in Fig. 8.

---

[2] Due to yaw, which is a rotation about the target center of mass, the effective length (L_{eff}) of the ceramic target from hit point to rear side of the target also varies with the off-center location. This yaw effect was approximately accounted for in determination of d_{oc}.

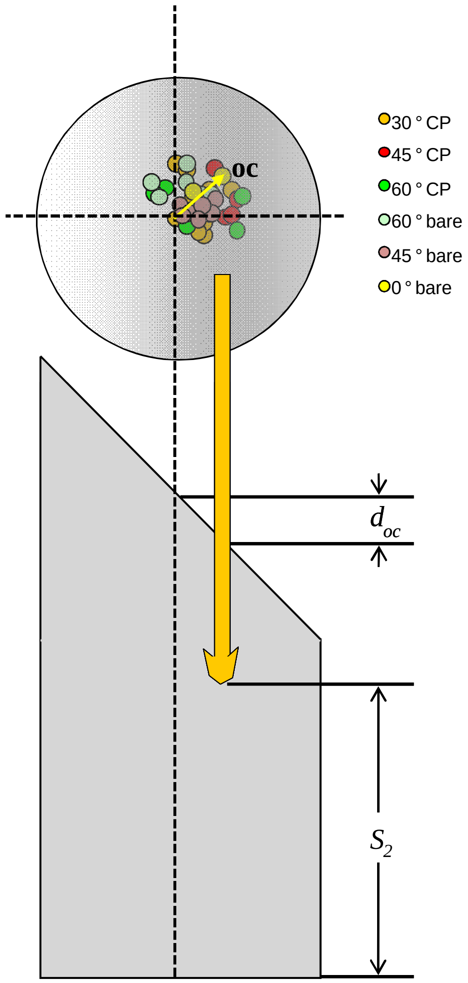

Figure 7. Schematic of off-centered impact.

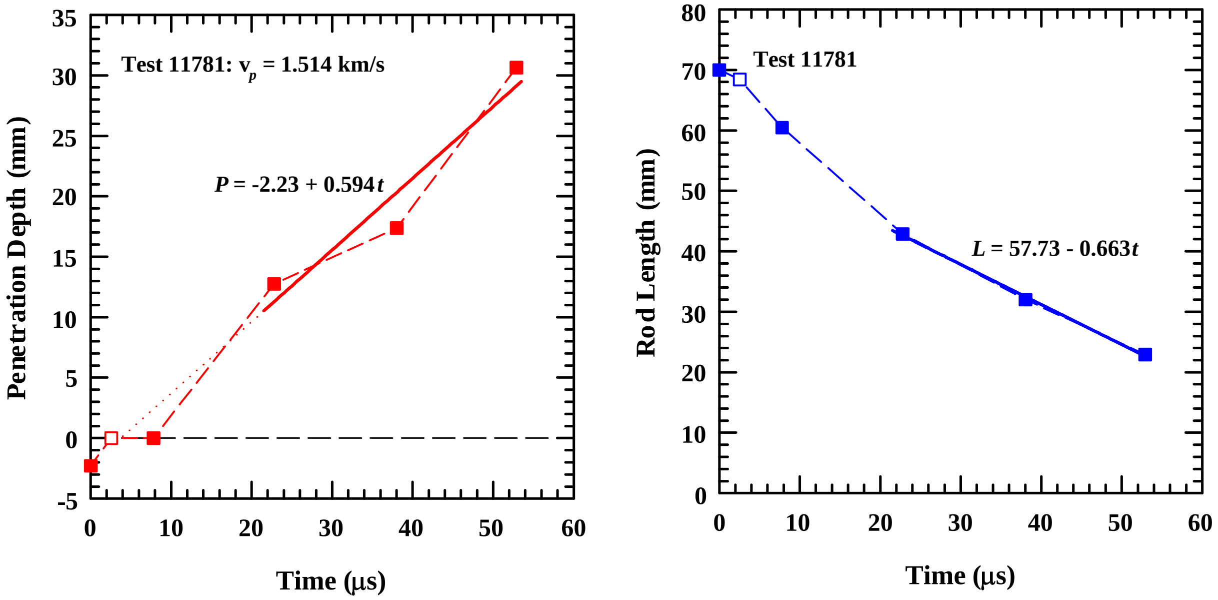

(a) Penetration-time data. **(b) Rod length-time data.**

Figure 8. Example of data from flash X-rays.

The time to penetrate the copper buffer is estimated from hydrodynamic theory:

$$u_{hydro} = \frac{\mathrm{v}_p}{1+\sqrt{\rho_t/\rho_p}} \tag{3}$$

$$\Delta t_{\mathrm{Cu}} = \frac{h_{\mathrm{Cu}}}{u_{hydro}} \tag{4}$$

with h_{Cu} the line-of-sight thickness of the buffer and ρ_t and ρ_p the target and projectile densities, respectively. This time is depicted as the open square in Fig. 8(a). Of course, it is understood that this is only an estimate since the presence of the ceramic surface can and will affect the penetration velocity when the projectile nose is within a couple of diameters of the interface.[3]

The amount of rod that is eroded while penetrating the copper buffer can also be estimated from hydrodynamic theory. The length of the rod after penetration through the Cu buffer is:

$$L_{rod} = L_R - \Delta t_{\mathrm{Cu}}\left(\mathrm{v}_p - u_{hydro}\right) \tag{5}$$

where L_R is the initial length of the rod. The point (Δt_{Cu}, L_{rod}) is plotted as the open symbol in Fig. 8(b).

Penetration velocity, u, and the consumption velocity, v_c, were calculated from the position-time data and the rod length-time data, respectively, using linear regression. The slopes of the linear regression results provide u and v_c. The dashed lines connect consecutive points in Fig. 8, and the solid lines indicate the time interval over which the estimates for u and v_c were made. The values for u and v_c for each experiment are listed in Table 1.

For experiments where there is a dwell-to-penetration transition, an estimate of the dwell time is made. For some experiments where there was only one X-ray with penetration, t_D had to be estimated from the dwell progression in the X-ray images. For many of the experiments, the dwell time t_D can be estimated with the help of the linear regression equation for the penetration depth P into the ceramic versus time t:

$$P = a + bt \tag{6}$$

where fit parameter b represents penetration velocity u. Dwell time t_D is then calculated from the axis intercept a and the time necessary for penetrating the Cu buffer Δt_{Cu} as:

$$t_D = -a/b - \Delta t_{\mathrm{Cu}} \tag{7}$$

An example of the procedure is shown in Fig. 9; the dotted line represents the extrapolation of the regression line back to the ceramic surface. The estimated time for penetrating the Cu buffer is 3.09 μs. There is a flash X-ray at 22.26 μs, showing no penetration into the ceramic. However, (22.3 – 3.1 =) 19.2 μs probably underestimates the dwell time. Application of Eqn. (7) gives an estimate of (27.5 – 3.1 =) 24.4 μs, which is the value listed in Table 1 (with the various approximations that have been made, we report dwell times to the nearest microsecond).

---

[3] The initial penetration velocity, because of the shock pressure, will be higher than the hydrodynamic penetration velocity. On the other hand, as the projectile nose nears the very hard ceramic surface, the penetration resistance will increase, thereby decreasing the penetration velocity below that of the hydrodynamic velocity. These two effects are offsetting. Further, the buffer thickness is only a few rod diameters thick. Therefore, it is believed that Eqns. (3) and (4) provides a reasonable estimate for the rod nose to reach the ceramic surface.

Another feature is denoted in Fig. 9(b). Rod length cannot always be estimated from the flash X-rays because the Cu cover plate makes observation of the projectile-ceramic interface difficult to observe (and sometimes the tail of the projectile is hidden by the cover plate for the last X-ray image). But the rod length can be estimated as a function of time during dwell, since the rod consumption rate should be the same as the impact velocity, i.e., $v_c = v_p$. Thus, the change in length, ΔL, of the rod between successive X-ray images (during dwell) is:

$$\Delta L = v_p \Delta t_{flash} \tag{8}$$

where the time interval between successive X-ray flashes is Δt_{flash}. The open symbols in Fig. 9(b) denote calculated values of rod length, in contrast to lengths measured (solid symbols) on the flash radiograph.

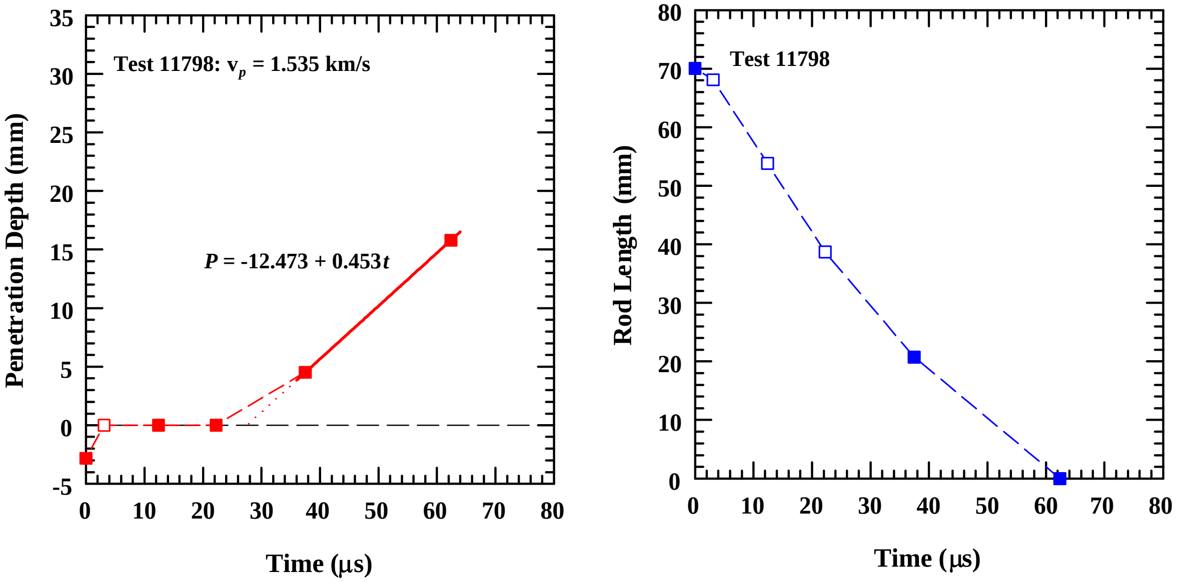

(a) Penetration vs. time.

(b) Rod length vs. time.

Figure 9. Example of measurements from the flash radiographs (45° target).

Sometimes, the flash radiography captures the onset of penetration after some significant penetration has already occurred, as shown in Fig. 8. Application of Eqn. (7) results in a dwell time of ~1 μs, which is less than observed experimentally. For those cases, the time of the last X-ray showing no penetration is used for the estimated dwell time (after adjusting for Δt_{Cu}). For the experiment in Fig. 8, this gives a dwell time of (7.8 – 2.6 =) ~5 μs.

There are three experiments in which dwell was reasonably long and it was only in the last X-ray that penetration was observed. These are three bare 45° experiments, all at a relatively low impact velocity (~1 km/s); one of these tests is shown in Fig. 10. An estimate of the penetration velocity as a function of impact velocity for bare SiC was determined from 60 experiments between 1.21 km/s to 6.24 km/s [15]:

$$u = -0.3662 + 0.7165 v_p \tag{9}$$

As the depth of penetration P_{last} is known at time t_{last}, then an estimate of the time t' for the onset of penetration (which also is the dwell time, t_D) is given by:

$$t' = t_{last} - \frac{P_{last}}{u} \tag{10}$$

where u is calculated from Eqn. (9). Admittedly, t' is a very "crude" estimate for t_D since Eqn. (9) is being extrapolated to lower impact velocities. The dotted line in Fig. 10 shows the estimated dwell time.

Graphical display of the data, similar to Figs. 8 and 9, are provided in the Appendix for each experiment.

Due to the limited number of data pairs for penetration after dwell and due to the sometimes relatively loose structure of the ceramic – caused by cracking during dwell and penetration –, results for u and v_c can vary for the same impact velocity quite substantially. This scatter is of physical origin and not caused by measurement errors. The accuracy of the values for u and v_c are therefore not directly comparable with the precision known from standard penetration experiments. Additionally, as already observed in penetration of ceramics [15], the penetration rate can vary approximately ±65 m/s (one standard deviation) about a mean value. This, apparently, is the nature of brittle materials (in contrast to ductile materials).

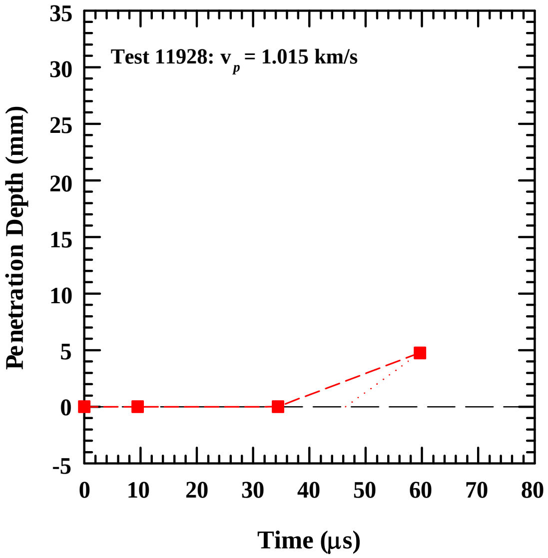

Figure 10. Example of estimate for t_D for penetration at the last X-ray flash.

3.2 Diagnostic and Experimental Specifics

The oblique target design resulted in several effects that were first detected during the initial experiments with the 30° and 45° targets. Contrary to a normal target, the cover plate for the oblique target partially obscures the view on the ceramic in the X-ray pictures. As the orientation of the target had to be optimized for the high-speed camera (to get a near frontal view of the rod hitting the surface), firing times of the X-rays were adjusted to achieve a clear image of the late penetration/dwell phase. The sequence of X-ray firings before and after the change to facilitate data collection is shown in Fig. 11.

For many experiments, the point of impact is the origin of a strong radial crack, which subsequently separates the edge of the ceramic from the ceramic body, as shown in Fig. 12. This phenomenon has been observed for both bare and cover plate experiments for impact velocities above 1.4 km/s. As mentioned in Refs. [33,15], cracks appear also for a normal target but in a symmetric manner. Here, for the oblique targets, the stress situation inside the ceramic is more asymmetric and may result in the specified crack pattern.

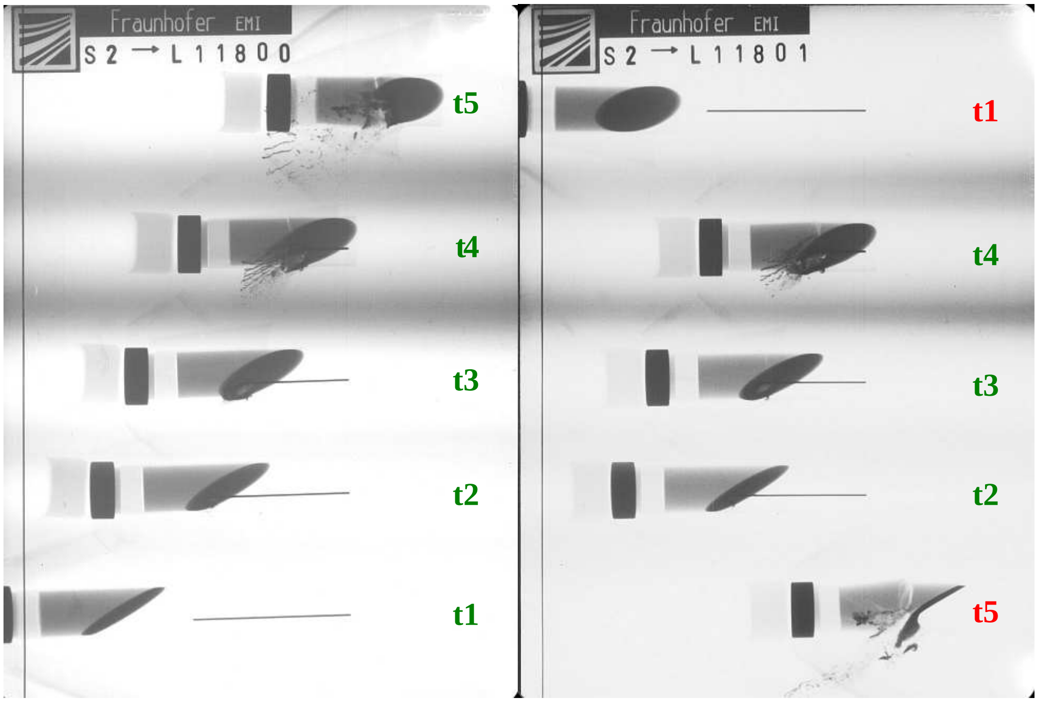

Figure 11. Left: standard X-ray sequence. Right: X-ray sequence with improved late-phase visibility.

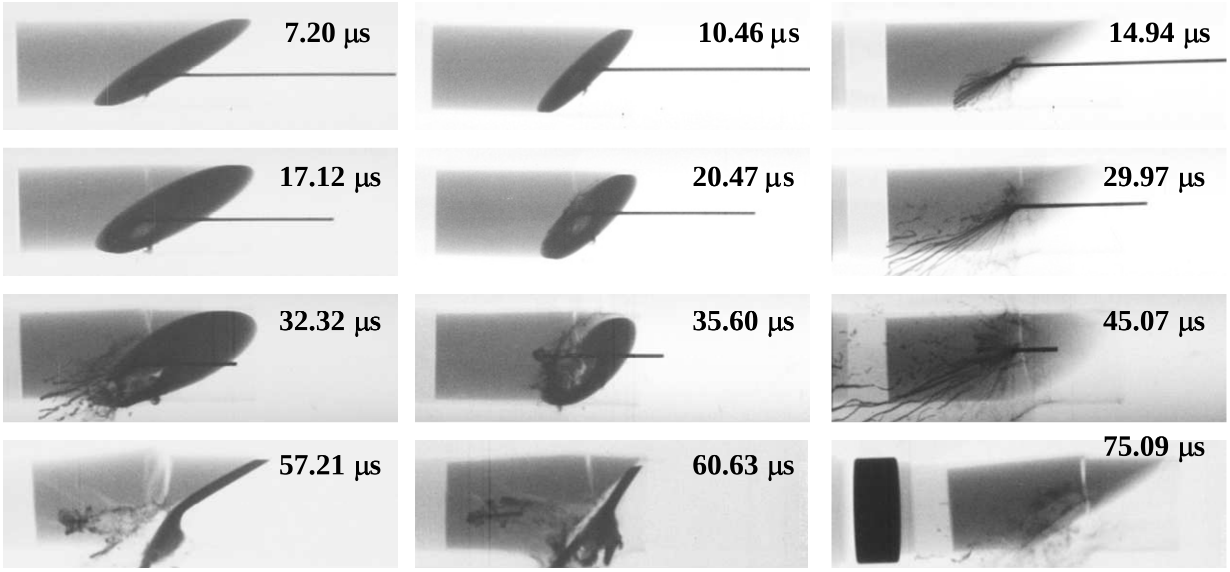

Figure 12. Crack development for Exp. 11801, 11821 and 11814 (from left to right). The edge of the ceramic separates from the ceramic body.

3.3 Visualization of Dwell

Dwell can be detected by either X-ray images or very high-speed optical images. When dwell occurs, the rod is diverted on the ceramic surface into characteristic chips/strips. For oblique impacts, the rod is diverted in a cone-like shape. This effect can best be seen for the bare targets as the cover plate reduces visibility. Figures 13 and 14 show an example of complete dwell visualized with the X-ray images (Fig. 13) and with the optical images (Fig. 14) for Experiment 11809, a bare target experiment.

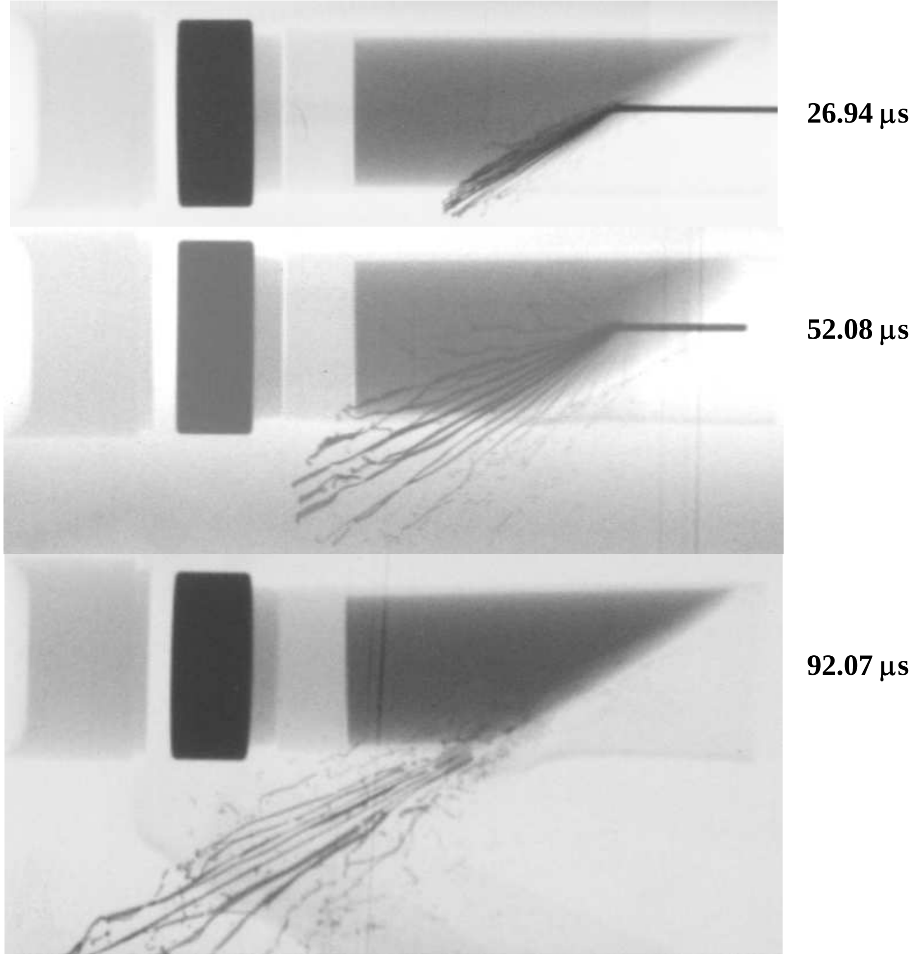

Figure 13. X-ray visualization of complete dwell for Exp. 11809 (v_p = 1.008 km/s).

For cases of partial dwell, X-ray images show at least one image where there is penetration into the ceramic (e.g., in Fig. 11 for time t5). The optical images stop showing the characteristic strips once penetration starts; additionally, ceramic dust is generated and begins to obscure the images.

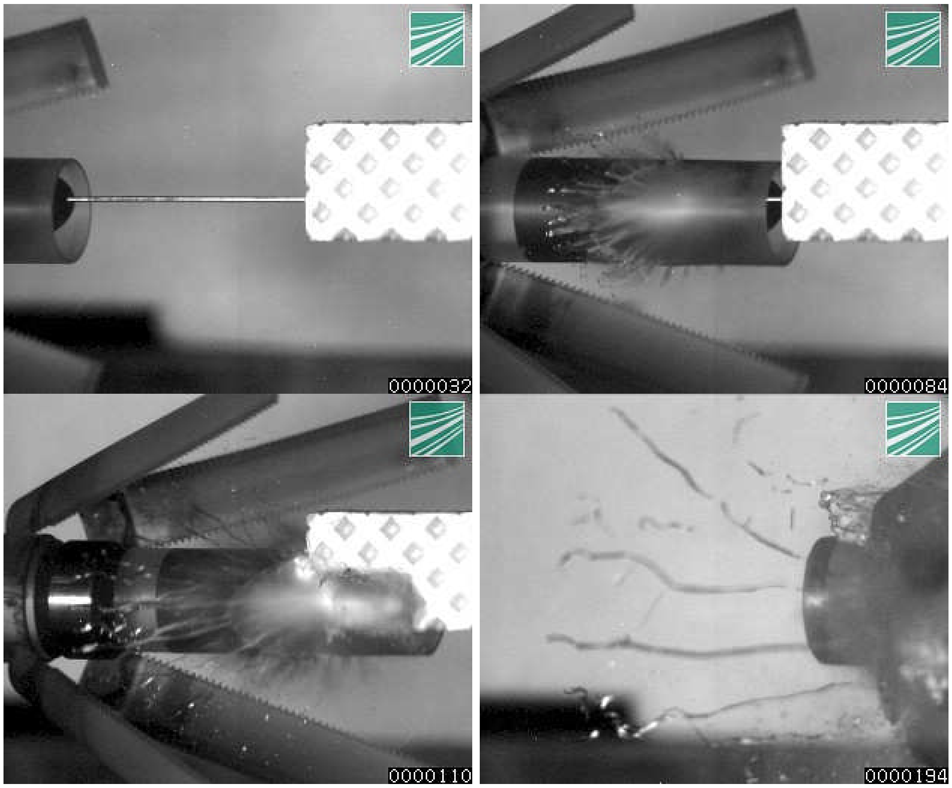

Figure 14. Optical visualization of complete dwell for Exp. 11809 (v_p = 1.008 km/s).

4.0 Analysis

4.1 Normal Impact Data

Experiments in Refs. [33,15] investigated the interface defeat ability of a normal (0°) SiC cylinder with and without a buffer attached to the front face. For a bare ceramic, stable dwell was possible for impact velocities up to approximately 0.825 km/s. With a copper buffer, the transition velocity from dwell to penetration increased to nearly ~1.55 km/s. The estimated dwell times t_D versus impact velocity are shown in Fig. 15 for three target types: bare ceramic, 4-mm-thick buffer, and 2-mm-thick buffer. The dashed line in the figure provides an estimate of the dwell time for total interface defeat of the 70-mm-long rod.[4] Arrows connect some data points with the dashed line. For these experiments, the rod was dwelling at the time of the last X-ray flash, so the arrow denotes how much additional time was required for total interface defeat.

The dwell-penetration transition velocity is defined as the impact velocity below which there is dwell and above which the rod penetrates. There is considerable uncertainty in the transition velocity for the bare target because the impact velocities for the bare targets are spaced quite far apart. For the buffered experiments though, the transition zones from dwell to penetration are very narrow. The transition velocity for the 2-mm-thick buffer is 1.570 ± 0.016 km/s; and for the 4-mm-thick buffer, it is 1.540 ± 0.018 km/s (shown as the shaded rectangle centered on 1.54 km/s).[5]

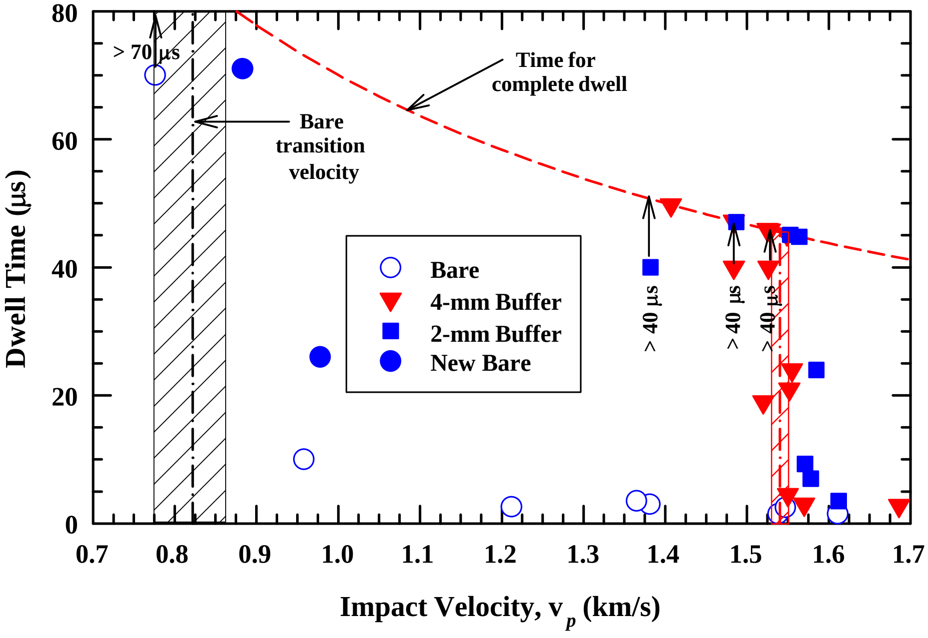

Figure 15. Dwell time vs. impact velocity for normal impact (0° obliquity), previous results [33,15].

---

[4] The calculation ignores rod erosion through the Cu buffer. At an impact velocity of 1.5 km/s, it is estimated that 1.35 mm of rod is eroded while penetrating the 2-mm-thick Cu buffer, and double that for the 4-mm-thick buffer.

[5] No distinction is made in Fig. 15 between a small cylindrical buffer and a full cover plate; however, there is an indication (albeit data are very limited) that a small-diameter buffer performs slightly better than a cover plate [15]. But, in general, the full cover plate combines performance with simplicity.

Two new experiments were conducted at 0° (Table 1) to provide a better estimate on the transition velocity for bare targets. These data are plotted in Fig. 16, and it is seen that the bare transition velocity increased from the original estimate of ~0.825 km/s to 0.920 ± 0.035 km/s because of better data resolution.

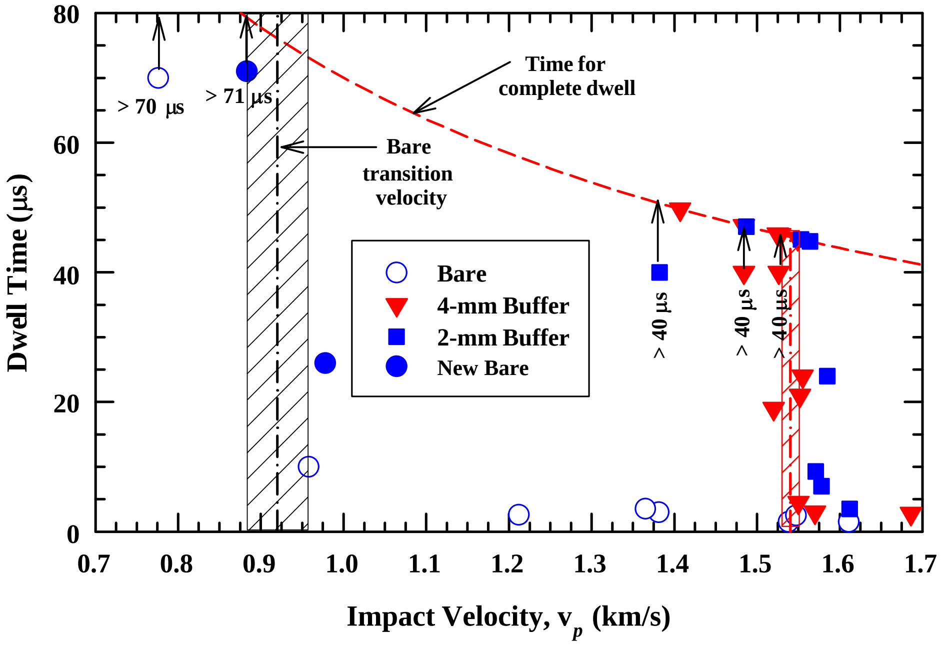

Figure 16. Dwell time vs. impact velocity for normal impact (0° obliquity) with revised estimate of bare transition velocity.

4.2 Cover Plate Experiments

The dwell times of the oblique cover plate (CP) experiments for the three obliquities are compared to the 0° cover plate experiments in Fig. 17 (the scale of the x-axis has been greatly expanded compared to Fig. 16). The inverted open triangles represent the dwell times for the 4-mm-thick buffer experiments at normal (0°) obliquity (the solid inverted triangles in Fig. 16). The hatched box, centered on 1.540 km/s, denotes the velocity interval for the transition from interface defeat to penetration at 0^{o} obliquity. Only the transition interval for the 4-mm-thick buffer is plotted here, since at obliquity the cover plates have a line-of-sight thickness greater than 2 mm.

Observations will be discussed for each of the impact obliquities.

- 30^{o} cover plate (solid diamonds in Fig. 17): Two of the experiments had extended dwell times of at least 39 µs; the arrows denote how much additional time was required for total interface defeat. Ignoring the datum with high yaw and the datum where the CP separated during launch, the onset of penetration with less than ~10 µs of dwell occurs at about the same impact velocity as the 0^{o} CP dwell-penetration transition velocity. However, it is observed that the target sometimes cannot support total interface defeat at velocities below the 0^{o} CP transition velocity, although there is extended dwell of 25-30 µs.

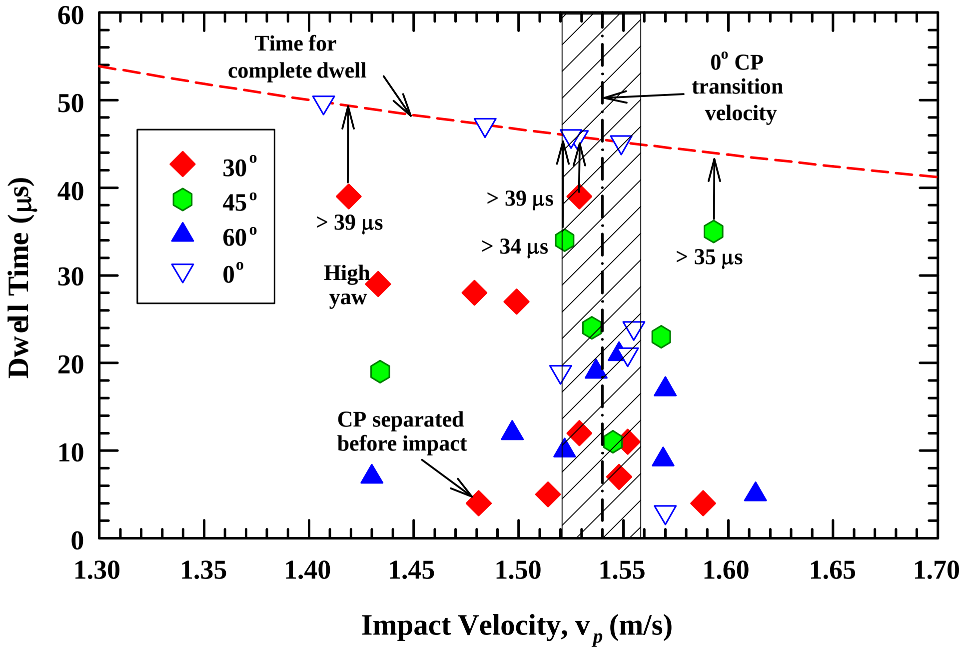

Figure 17. Dwell time vs. impact velocity for oblique experiments (all targets with cover plate).

- 45° cover plate (solid hexagons in Fig. 17): Results for the 45° CP experiments are somewhat similar to the 30° obliquity case. There are two experiments where dwell is still on-going at ~35 µs (the time of the last flash X-ray is 66 µs, but from these images, it can only be inferred that there was complete interface defeat). One of these data points is at a relatively high impact velocity (~1.60 km/s). In the 0° CP transition region, the 45° target, on average, dwells somewhat longer than the 30° CP targets. However, there is one experiment at ~1.43 km/s where dwell persisted only for 19 µs.
- 60° cover plate (solid upright triangles in Fig. 17): There are no extended dwell times for the 60° CP oblique targets (solid upright triangles). The longest dwell time is ~20 µs, and most experiments have significantly less dwell times.

The oblique cover plate experiments show that there is no increase in the transition velocity compared to the normal CP target. While the 30° and 45° CP targets achieve dwell times where most of the rod is eroded, the 60° CP target can only achieve dwell for about half the rod length.

These results were surprising and unexpected. As there were several 45° and 60° targets remaining, it was decided to examine the dwell transition times for bare (no cover plate) targets. The results are discussed in the next section.

4.3 Experiments without Cover Plate

Results for the 45° oblique targets, with and without the cover plate, are shown in Fig. 18. For comparison, the results for the bare 0° experiments, along with the dwell transition velocity for targets with a 4-mm-thick cover plate at 0°, are shown. It is seen that extended periods of

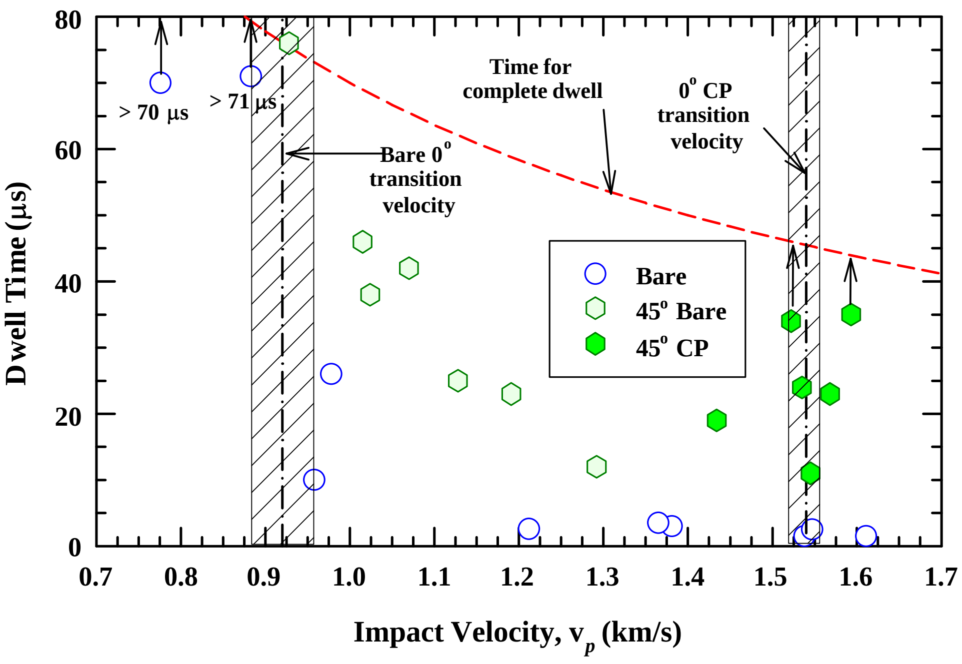

Figure 18. Dwell times vs. impact velocity for 45° oblique targets, with and w/o cover plate.

dwell can exist for the bare 45° target for impact velocities of a couple hundred meters per second higher than for normal impact. But dwell times decrease as the impact velocity increases from approximately 1.1 km/s to 1.3 km/s (but still with longer dwell times than at 0°).

There are two experiments with the 45° CP that had extended periods of dwell, denoted with the arrows in Fig. 18 (the last X-ray images are slightly greater than 60 µs, well after the target has collided with the Styrofoam holder). The cover plate appears to extend the dwell transition time over a bare 45° target. With the limited data, the average dwell time for impact velocities between 1.4 and 1.6 km/s is approximately 25 µs, but with significant deviations about this average.

The center set of flash X-rays in Fig. 12 shows the formation of a radial crack for the 45° CP experiment at 1.43 km/s (with 19 µs of dwell). It is conjectured that the formation of the radial crack combined with the presence of the cover plate results in the degraded dwell performance of the 45° target at the higher impact velocities.

Results are shown in Fig. 19 for the 0° bare and 60° bare and CP targets. The results for the bare 0° experiments, along with the dwell transition velocity for targets with a 4-mm-thick CP at 0°, are shown. The 60° bare targets exhibit total interface defeat up to an impact velocity of approximately 1.4 km/s. The data are extremely limited (one data point), but the dwell performance of the bare 60° target is as good as the dwell performance of the 60° CP targets. (The datum at 1.65 km/s will be discussed in the next subsection.) Overall, it can be said that the bare 60° target performs better than the 60° CP target.

X-ray images of experiments with and without a cover plate are compared in Fig. 20 for a nominal impact velocity of 1.42 km/s. A radial crack appears for the bare target at an impact velocity of 1.42 km/s, but not at lower impact velocities. Since this is approximately the impact velocity where dwell performance begins to decrease, whether bare or with a cover plate, it is suggestive that radial cracking reduces the dwell capability.

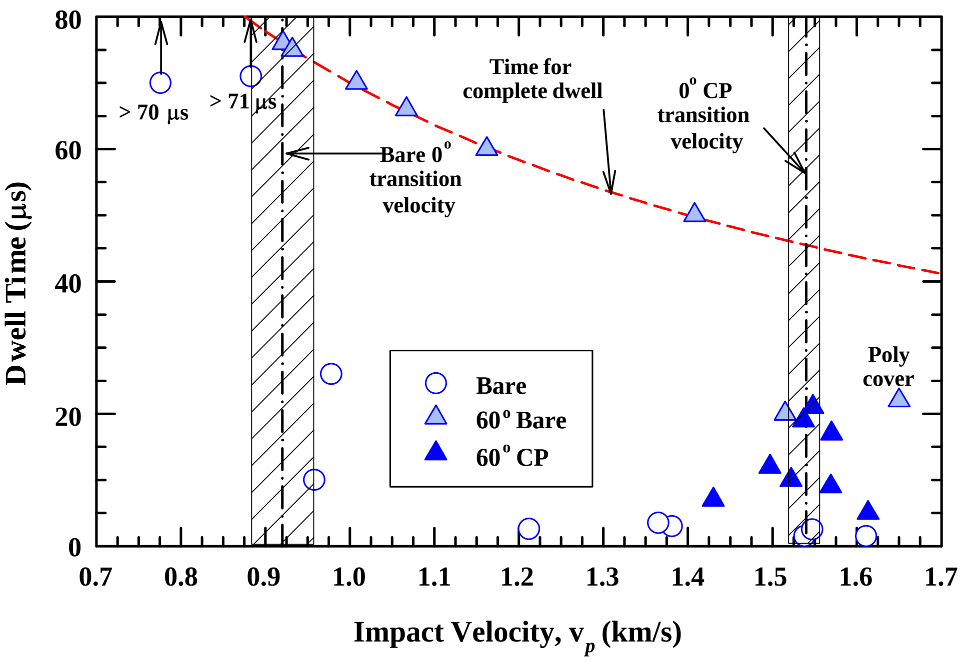

Figure 19. Dwell times vs. impact velocity for 60° oblique targets, with and w/o cover plate.

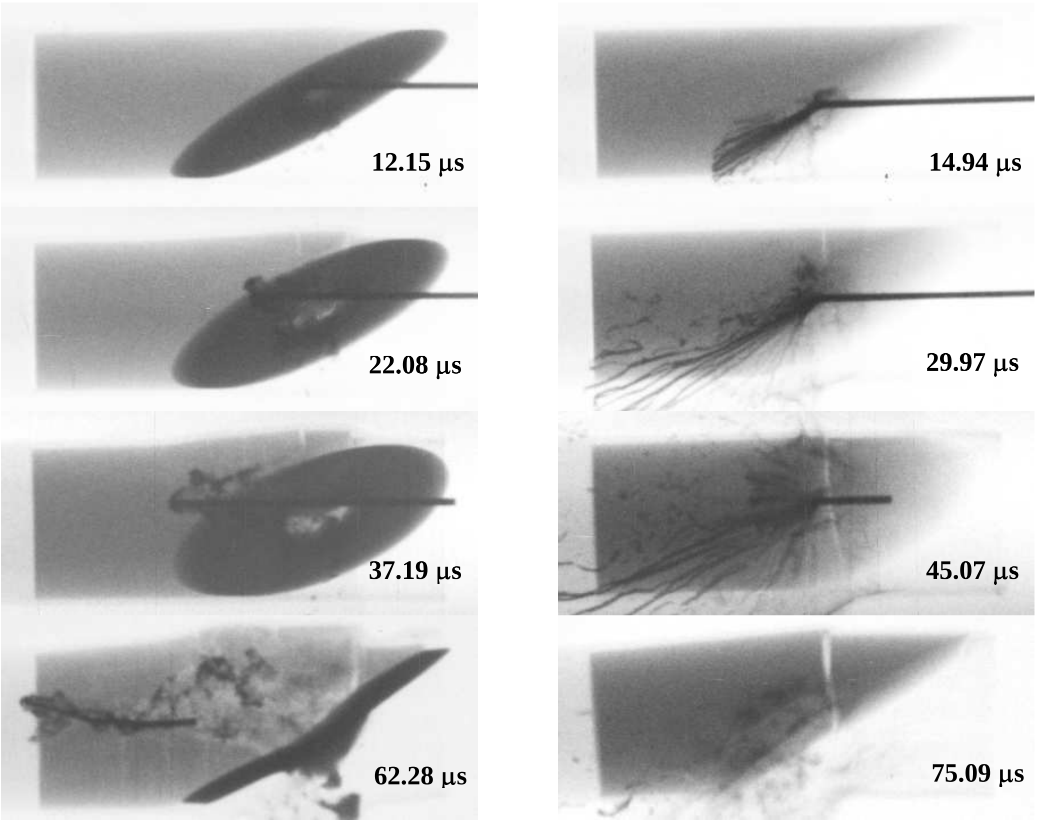

Exp. 11819: v_p = 1.430 km/s – 5 μs dwell

Exp. 11814: v_p = 1.408 km/s – 50 μs dwell (complete dwell)

Figure 20. Comparison of dwell performance at 60° target with $v_p \approx$ 1.42 km/s.

4.4 Special Experiments

Prior to summarizing the results further, and speculating on some of the mechanics that might be involved, there were three experiments that had different target configurations than the other experiments. The results of these experiments are described in this subsection.

One of the 0° targets had a polycarbonate cover, as shown in Fig. 21. Time zero is impact on the polycarbonate cover. The rod forms a hydrodynamic head as it penetrates the polycarbonate, as seen in the image at 31.40 μs. Assuming hydrodynamic theory, Eqn. (3), and using the densities of polycarbonate and gold, the penetration velocity should be 0.707 km/s. As the polycarbonate has a thickness of 30 mm, this would mean that the rod would impact the ceramic surface at 42.4 μs, and the rod will have eroded 7.5 mm.

However, the rod actually penetrates a little slower than 0.707 km/s, presumably due to the strength of the polycarbonate. The penetration depth at 31.40 μs is 19.3 mm, which then gives a penetration velocity of 0.615 km/s. Thus, the rod impacts the ceramic interface at 48.8 μs after impact on the front surface of the polycarbonate. The rod will have eroded 13.1 mm while going through the polycarbonate. This number is listed in a footnote to Table 1.

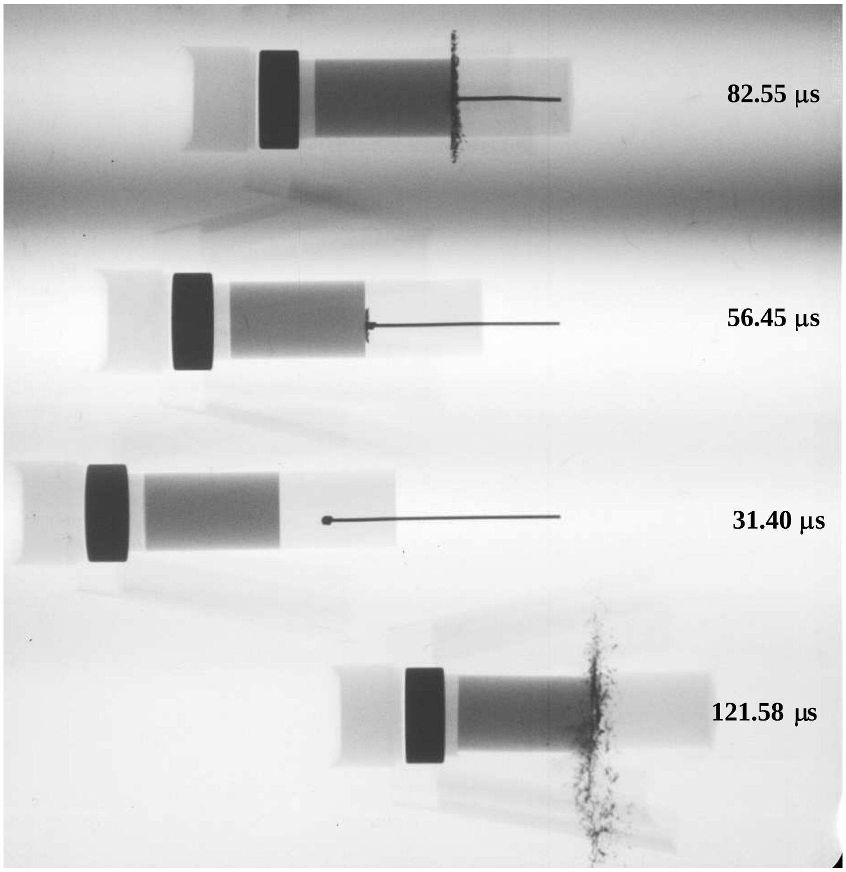

Figure 21. Exp. 11811: normal impact at 0.883 km/s with polycarbonate cover.

One of the 60° targets was fitted with a thicker 4-mm cover plate (line-of-sight thickness of 8 mm). The impact velocity was 1.613 km/s. The sequence of flash X-rays are shown in the left-hand side of Fig. 22. It is estimated that there might be 5 μs of dwell, although there is a lot

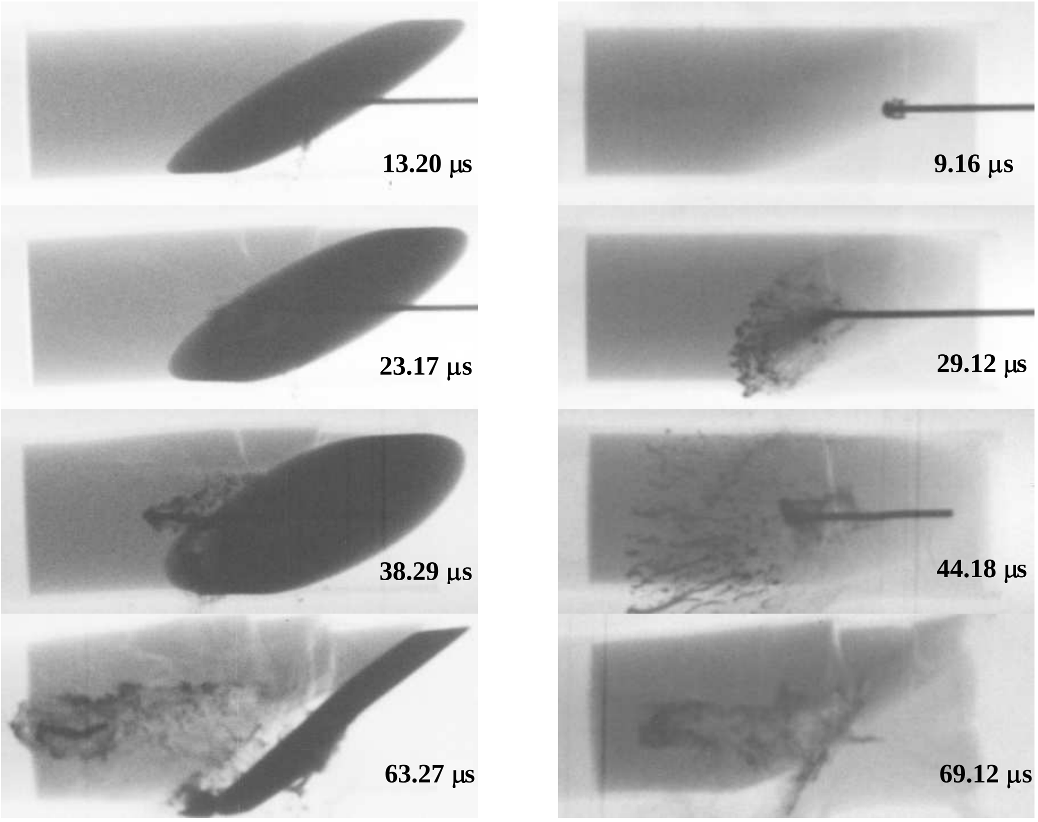

Exp. 11820: $v_p = 1.613$ km/s – 5 µs dwell **Exp. 11822: $v_p = 1.650$ km/s – 22 µs dwell**

Figure 22. Comparison of dwell performance at 60° target with $v_p \approx 1.63$ km/s.

of uncertainty because the rod-target interface is initially shadowed by the cover plate. Regardless, the extra line-of-sight thickness of the cover plate does not change the overall results.

There was a second 60° target that was fitted with a polycarbonate cover in such a way that the complete target resembled a cylinder, as shown in Fig. 23 (the two pieces are separated, with a space in between). This target was counted as a bare target since it did not have a cover plate, although the projectile had to penetrate the polycarbonate layer prior to interacting with the ceramic. The objective was to remove the impact shock and perhaps provide ramp loading to the ceramic.

Figure 23. Target (left) and polycarbonate cover (right).

The sequence of flash X-rays is shown in the right-hand-side of Fig. 22. The penetrator forms a mushroom tip while penetrating the polycarbonate, as can be seen in the image at 9.16 µs. The depth of penetration into the polycarbonate is 12.9 mm, giving a penetration velocity of 1.41 km/s (a little higher than the hydrodynamic calculation). Thus, it takes 14.2 µs for the rod to reach the ceramic interface, and 3.4 mm of the rod will have eroded. It is estimated that the rod began to penetrate the ceramic 36.5 μs after initial impact with the polycarbonate. Therefore, dwell persisted for approxiamtely 22 μs (Table 1).

For Exp. 11822, which is at 1.650 km/s, there is a slight increase in dwell time compared to lower impact velocities. Comparing both experiments shown in Fig. 22, the polycarbonate cover performs better than the thick copper plate. Although the data is limited to one experiment, this might be a suitable approach for an improved target design for oblique targets, possibly with a flat hit zone on or before the cover plate.

4.5 Accuracy of Calculated Penetration and Consumption Velocities

It has already been indicated that limited data are available to estimate the penetration and consumption velocities, either because of extended dwell and/or a portion of the rod being hidden by the cover plate. This results in some uncertainty in the accuracy of the calculated values. However, it was shown in Ref. [33-34] that the sum of the penetration and consumption velocities equals the impact velocity, i.e.,

$$u + \mathrm{v}_c = \mathrm{v}_p \tag{11}$$

because the gold rod has very little strength [35]. Equation (11) was also shown to hold for penetration into borosilicate glass [35].

The sum of the penetration and consumption velocities are plotted versus the impact velocities for the three sets of oblique experiments in Figs. 24-26. The dashed line at 45° in each figure represents Eqn. (11). The various symbols are indentified in the legends, with a distinction being made between targets that had cover plates (CP) or were bare. Also, a distinction is made for targets where there was total interface defeat, in contrast to dwell (or little dwell) and penetration. Of course, u is zero for targets with dwell, so that the plotted point is derived from the consumption velocity. The last three digits of the test number, as listed in Table 1, are placed by their respective data points.

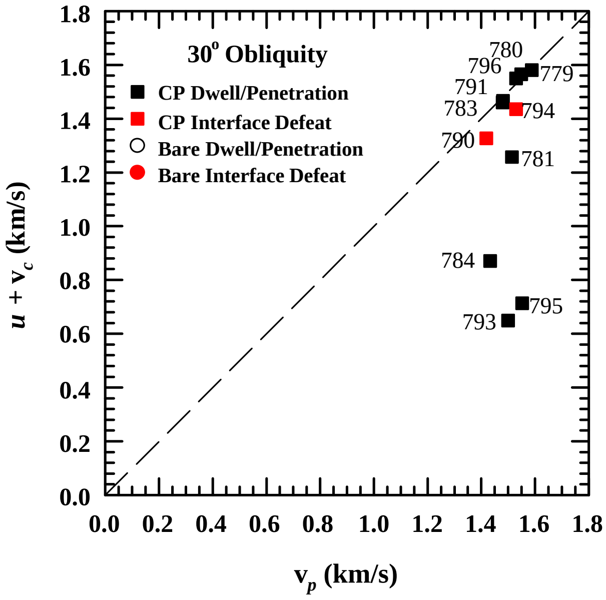

Figure 24. $u + \mathrm{v}_c$ **vs.** v_p **for 30° oblique targets.**

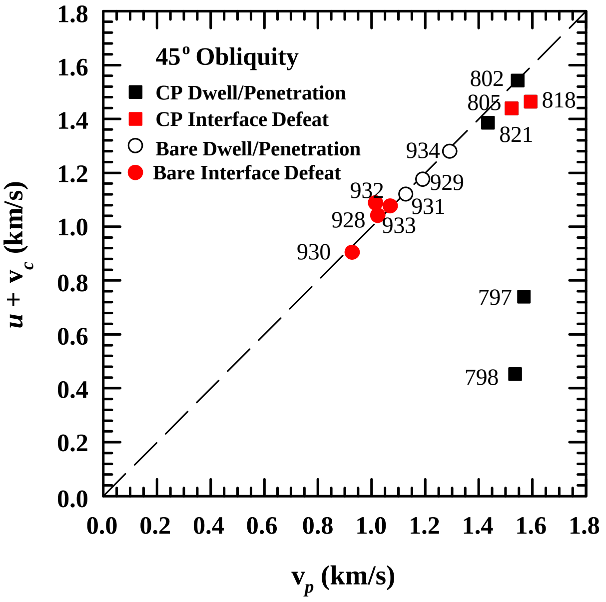

Figure 25. $u + \mathrm{v}_c$ **vs.** v_p **for 45° oblique targets.**

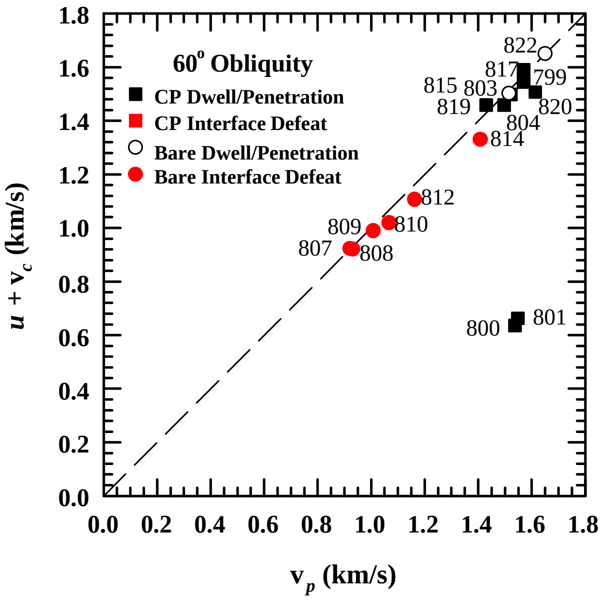

Figure 26. $u + v_c$ vs. v_p for 60° oblique targets.

Most of the data fall on or very close to the 45° line, attesting to the accuracy of the measurements. In each graph there are several points that fall considerably below the 45° line, for example, experiments 795, 797, and 801 (and other experiments nearby). Values of *u* are estimated from the penetration-time data, but there is no estimate for v_c because the length of the rod could not be determined between two successive flash X-rays (and hence, the consumption velocity). We will return to these data in the paragraph below.

For the experiments where there is interface defeat, $u = 0$; and it is observed that $v_c \neq v_p$, but rather is slightly less than v_p. It was discussed in Ref. [33] that there could be a very low penetration rate that is not measureable in the time frame of the experiments.

For experiments where *u* was estimated from the measured penetration-time data, but v_c could not be estimated, the calculated *u* can be compared to other penetration data. Figure 27, from Ref. [15], shows the penetration velocity as a function of impact velocity for a variety of SiC-N targets. The SiC-N targets consisted of intact ceramic (bare or contained in a sleeve), predamaged ceramic (TS and TS-2) where the ceramic has non-contiguous cracks generated by thermal shock, and *in-situ* comminuted (TS/CL) ceramic where a thermally shocked ceramic then had six load/unload cycles up to 1.7 GPa. The TS/CL, TS, TS-2, and the intact sleeved SiC specimens were encased in a 7075-T6 aluminum sleeve with a 3-mm-thick cover plate. Experiments were also conducted with 0.75-mm-diameter rods and 1.00-mm-diameter rods onto bare SiC-N targets. Within scatter, aside from the dependence on impact velocity, there is no difference in the penetration velocity for the various SiC-N specimens. The dashed line represents a linear regression through all the data, and the dotted lines represent 1.5 standard deviations (1.5 σ) about the mean response.

The data in Fig. 27 are replotted in Fig. 28, but only for the velocity range between 1.4 km/s and 1.7 km/s. Five data points from Fig. 27 are within the velocity range of Fig. 28, and these are plotted with the same symbols as in Fig. 27. The penetration velocities for all the oblique experiments (except those experiments that had total interface defeat) are plotted in Fig. 28. The last three digits of the test number, for identification purposes, have been placed next to some of

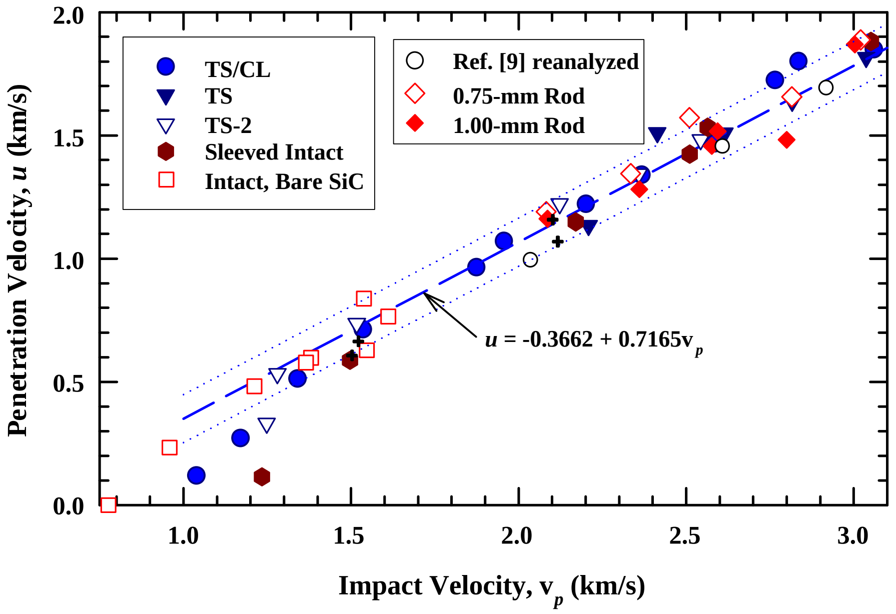

Figure 27. Penetration velocity vs. impact velocity for SiC-N (from Ref. [15])

the data points. Generally, all the penetration velocities lie within or very near the 1.5-σ band. The penetration velocities for experiments 11779 and 11803 lie just outside the 2-σ scatter band. Only experiments 11798 and 11820 have calculated penetration velocities considerably outside the 2-σ uncertainty or scatter band of the data. These results attest to the accuracy of the experimental data.

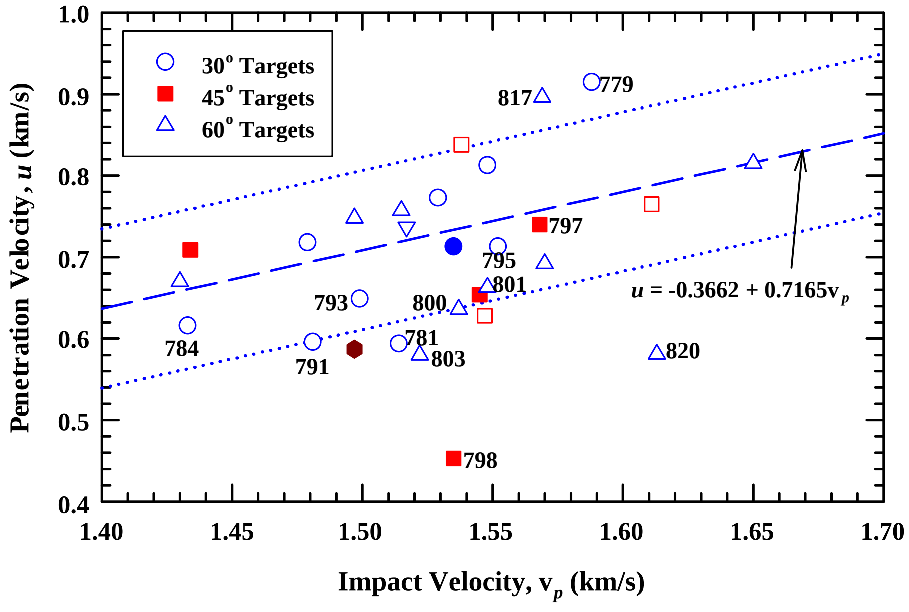

Figure 28. Comparison of outlier data with previous data.

4.6 Summary of Oblique Dwell Experiments

A comparison of the dwell times for the bare 0°, 45° and 60° targets is shown in Fig. 29. *Obliquity increases dwell time for bare SiC targets, and the larger the target obliquity the higher the impact velocity for which the ceramic can sustain significant dwell.*

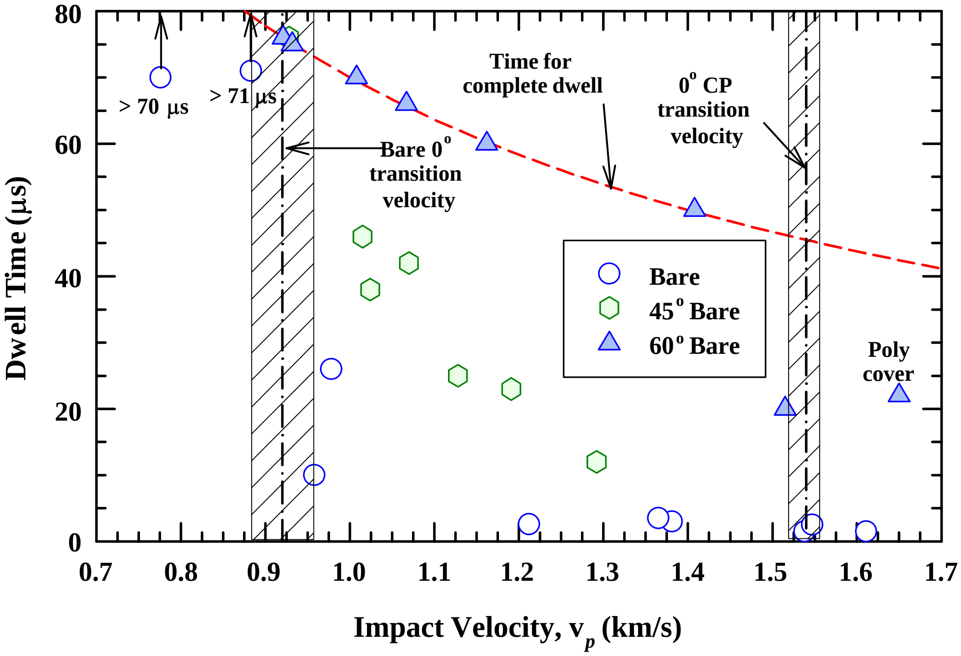

Figure 29. Dwell time vs. impact velocity for normal and oblique bare targets (no cover plate).

All the oblique data are plotted in Fig. 30. It is hazardous to infer too much from such a limited, and in many places, sparse data set. Nevertheless, the following general conclusions appear to be warranted, with the caveat that these conclusions could be revised with further data.

Cover plates assist in extending dwell times for all target obliquities compared to bare, normal targets. However; as impact obliquity increases to 60°, the effect of the cover plate is diminished and may even be detrimental to potential performance. Sustained dwell (but not necessarily interface defeat) occurs for oblique bare targets at impact velocities greater than the bare 0° transition velocity. Furthermore, the time of sustained dwell for the bare targets increases with impact obliquity.

For targets with cover plates, interface defeat for 30° and 45° oblique targets can be achieved for the same impact velocity as for 0° targets. However, transition interval for normal impact is ± 0.018 km/s; this transition interval is a zone where there is significant dwell, but not all experiments achieved interface defeat. The lower boundary of the transition velocity interval for the 30° and 45° oblique targets decreases from approximately 1.525 km/s to 1.425 km/s. Within this velocity interval, dwell times can vary significantly. Some of the 30° oblique targets have very low dwell times (similar variability may be present for the 45° oblique targets, but there were not a sufficient number of experiments to observe the variation seen in the 30° oblique experiments).

As the impact obliquity increases to 60°, time-of-dwell performance for the targets with cover plates decreases dramatically. It is conjectured that the formation of the radial crack, particularly at impact velocities above approximately 1.4 km/s, is detrimental to achieving interface defeat. Cone cracks are seen in X-ray and photographic images for 0° oblique targets [33], and rod material flows along these cracks, but interface defeat is still observed. The combination of obliquity and the cover plate, combined with the generation of the radial crack, appears to be detrimental to achieving interface defeat at the higher impact velocities. The length of time that the rod can dwell is probably sensitive to timing/formation of the radial crack.

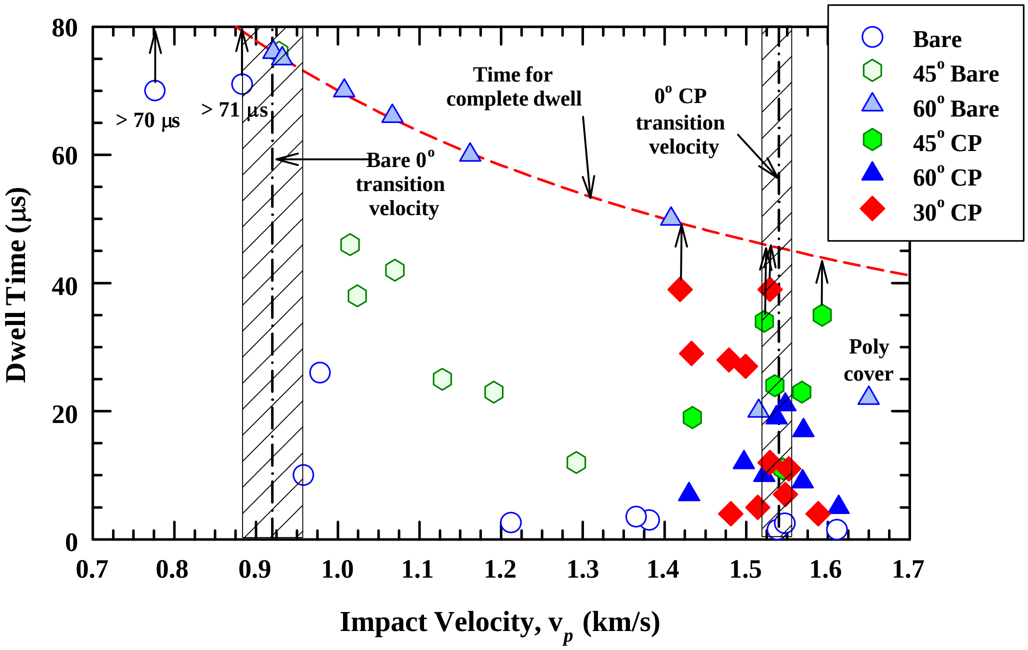

Figure 30. Dwell time vs. impact velocity for bare and cover plate targets at 45° and 60° obliquity.

One experiment exists, with the polycarbonate buffer (and no copper buffer), that has a sustained dwell time of 22 μs. The presence of the polycarbonate may have changed the timing of formation of the radial crack, resulting in increased dwell performance.

If it is assumed during dwell that the ceramic can sustain a maximum value for the Bernoulli stress, Σ_t, at the transition velocity v_t, then the following equation applies for normal impact:

$$\Sigma_t = \frac{1}{2}\rho_p v_t^2 \tag{12}$$

where ρ_p is the density of the gold projectile. The Bernoulli stress normal to the surface for an oblique target is given by:

$$\Sigma = \frac{1}{2}\rho_p \left(v_p \cos\theta\right)^2 \tag{13}$$

where v_p is the impact velocity. If the transition stresses are the same for normal and oblique targets, then this would imply that the transition velocity for a θ° oblique bare target should be:

$$\left[v_t\right]_\theta = \frac{\left[v_t\right]_0}{\cos\theta} \tag{14}$$

where the subscript on the brackets refers to the obliquity angle θ, and $[v_t]_0$ is the transition velocity at 0°

Immediately, it is seen that Eqn. (14) does not apply to the cover plate targets, as there is no increase in the transition velocity for oblique cover plate targets; i.e., Eqn. (14) applies only to bare targets. Equation (14) is plotted in Fig. 31 for bare targets, with 0.90 km/s for the transition velocity at 0°. Also plotted (solid squares) are the transition velocities for 45° and 60°. Although interface defeat is not observed for the 45° target, there is extended dwell up to approximately 1.1 km/s. There is interface defeat at approximately 1.4 km/s for the 60° oblique targets. It is seen that Eqn. (14) overpredicts the transition velocities as a function of obliquity. Admittedly, the mechanics is not as simple as represented by Eqn. (14) because the bare normal target experiences the impact shock, which is much larger than the Bernoulli stress. Also, the stagnation stress for oblique targets is considerably more complicated than for a normal target.

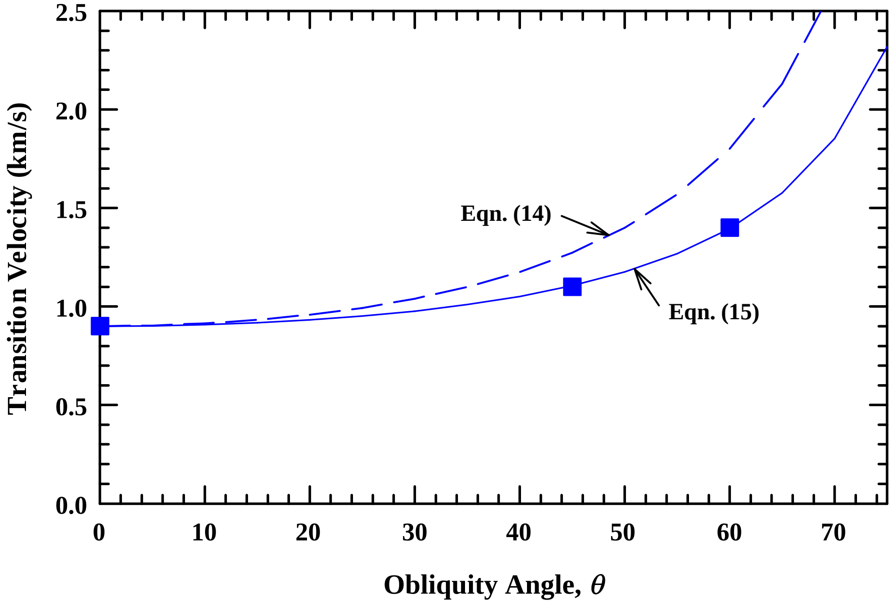

Figure 31. Transition velocity vs. target obliquity angle.

An alternate expression for the transition velocity is given by Eqn. (15), where an obliquity factor f is introduced to reduce the $\cos\theta$ dependence:

$$[v_t]_\theta = (1 - f)[v_t]_0 + f\,\frac{[v_t]_0}{\cos\theta} \qquad (15)$$

The obliquity factor f is adjusted to match the data point at 60° ($f = 0.55$). Results are shown in Fig. 31. It is not suggested that Eqn. (15) represents the appropriate mechanics, but the results suggest that the transition velocity for a bare ceramic could be increased by increasing the obliquity angle. This is certainly an intriguing possibility.

5.0 Conclusions

Unconfined SiC ceramics at three obliquity angles—30°, 45°, and 60°—were examined for their interface defeat ability against gold rod impact and compared with existing normal (0°) impact experiments.

From the tests, the following observations were made:

- Cover plates extend dwell times for all target obliquities compared to bare, normal targets.
- Oblique ceramics with an attached copper cover plate show a decrease in dwell performance compared to a 0° ceramic with cover plate. The performance degradation is most apparent for the 60° obliquity. Compared to the bare 60° targets, dwell time performance stagnates at around the same values. This is in remarkable contrast to the findings for the normal (0°) targets of [33,15] where the transition velocity was nearly doubled with an attached cover plate.
- Sustained dwell (but not necessarily interface defeat) occurs for oblique bare targets at impact velocities greater than the bare 0° transition velocity.
- The time of sustained dwell for bare targets increases with impact obliquity.
- A simple model that describes the increase in dwell potential as a function of target obliquity predicts the strongest increase for obliquity angles greater than 60°.
- At the impact point, the development of a radial crack in the ceramic can be observed for both bare and cover-plated oblique SiC above impact velocities of around 1.4 km/s. This crack may be the root of the reduction in dwell performance of the ceramic.
- Results from one experiment (the 60° target with polycarbonate cover) potentially suggest that changes in the target design could result in better dwell performance.

More work is required to understand the mechanics of dwell for oblique targets. Numerical simulations combined with additional experiments would provide further understanding. The potential is significant, but more work is required if the potential is to be realized.

6.0 References

1. S. V. Rasorenov, G. I. Kanel, and V. E. Fortov. The fracture of glass under high pressure impulsive loading. *High Press. Res*, **6**: 225 – 232 (1991).
2. N. S. Brar, S. J. Bless, and Z. Rosenberg. Impact-induced failure waves in glass bars and plates. *J. Appl. Phys.*, **59**(26): 3396-3398 (1991).
3. N. Bourne, J. Millett, Z. Rosenberg, and N. Murray. On the shock induced failure of brittle solids. *J. Mech. Phys. Solid*, **46**(10): 1887-1908 (1998).
4. N. K. Bourne, J. C. F. Millet, and J. E. Field. On the strength of shocked glasses. *Proc. R. Soc. Lond. A*, **455**: 1275-1282 (1999).
5. A. A. Kozhushko, D. L. Orphal, A. B. Sinani, and R. R. Franzen. Possible detection of failure wave velocity using hypervelocity penetration experiments. *Int. J. Impact Engng.*, **23**(1-12): 467-475 (1999).
6. C. E. Anderson, Jr., D. L. Orphal, and D. W. Templeton. Reexamination of the requirements to detect the failure wave velocity in SiC using penetration experiments. ***Shock Compression of Condensed Matter–2003***, (M. D. Furnish, Y. M Gupta, and J. W. Forbes, Eds.), CP706, pp. 707-710, AIP, Melville, NY (2004).
7. Th. Behner, V. Hohler, C. E. Anderson, Jr., and D. L. Orphal. Accuracy and position requirements for penetration experiments to detect the effect of failure kinetics in ceramics. *Proc. 21st Int. Symp. Ballistics*, pp. 118-125, The Defense Science and Technology Organization, Australia (2004).
8. D. L. Orphal, C. E. Anderson, Jr., D. W. Templeton, Th. Behner, V. Hohler, and S. Chocron. "Using long-rod penetration to detect the effect of failure kinetics in ceramics. *Proc. 21st Int. Symp. Ballistics*, pp. 744-751, The Defense Science and Technology Organization, Australia (2004).
9. T. Behner, D. L. Orphal, V. Hohler, C. E. Anderson, Jr., R. L. Mason, and D. W. Templeton. Hypervelocity penetration of gold rods into SiC-N for impact velocities from 2.0 to 6.2 km/s. *Int. J. Impact Engng.*, **33**(1-12), 68-79 (2006).
10. C. E. Anderson, Jr., D. L. Orphal, T. Behner, V. Hohler, and D. W. Templeton. Re-examination of the evidence for a failure wave in SiC penetration experiments. *Int. J. Impact Engng.*, **33**(1-12), 24-34 (2006).
11. C. E. Anderson, Jr., T. Behner, D. L. Orphal, A. E. Nicholls, V. Hohler, and M. Wickert. Time-resolved penetration into pre-damaged, *in-situ* comminuted and compacted powder silicon carbide. SwRI Report 18.12544/001, prepared for U.S. Army RDECOM-TARDEC, AMSRD-TAR-R, Warren, MI, October (2007).
12. C. E. Anderson, Jr., T. Behner, D. L. Orphal, A. E. Nicholls, and D. W. Templeton. Time-resolved penetration into pre-damaged hot-pressed silicon carbide. *Int. J. Impact Engng.*, **35**(8), 661-673 (2008).
13. C. E. Anderson, Jr., T. Behner, D. L. Orphal, A. E. Nicholls, T. J. Holmquist, and M. Wickert. Long-rod penetration into intact and pre-damaged SiC ceramic. *Proc. 24th Int. Symp. Ballistics*, **2**: 822-829, DES*tech* Publications, Inc., Lancaster, PA (2008).
14. C. E. Anderson, Jr., T. Behner, D. L. Orphal, T. J. Holmquist, and A. E. Nicholls. Penetration experiments into intact and pre-damaged silicon carbide. SwRI Report 18.12544/020, prepared for RDECOM-TARDEC, RDTA-RS, Warren, MI, July (2010).

15. C. E. Anderson, Jr., Thilo Behner, Timothy J. Holmquist, Dennis L. Orphal, and Nikki L. King. Investigation of rod size effects and buffer geometry on penetration and interface defeat of gold rods into silicon carbide. SwRI Report 18.12544/025, prepared for RDECOM-TARDEC, RDTA-RS, Warren MI, September (2010).
16. C. E. Anderson, Jr., S. Chocron, and T. Behner. A constitutive model for *in-situ* comminuted silicon carbide. *J. Am. Cer. Soc.*, **92**(6): 1280-1286 (2009).
17. S. Beissel and G. R. Johnson. Influence of the third invariant in modeling the ballistic impact of silicon carbide. SwRI Report 18.12544/024, prepared for RDECOM-TARDEC, RDTA-RS, Warren, MI, August (2010).
18. G. E. Hauver and A. Melani. Behavior during penetration by long rods. *Proc. 2nd BRL Topical Symp.: Experimental Research and Modeling Support*, pp. 149-160, U. S. Army Ballistic Research Laboratory, Aberdeen Proving Ground, MD, 24 May (1988).
19. G. E. Hauver, P. H. Netherwood, R. F. Benck, W. A. Gooch, W. J. Perciballi, and M. S. Burkins. 1992. Variation of target resistance during long-rod penetration into ceramics. *Proc. 13th Int. Symp. Ballistics,* **3:** 257-264, National Defence Establishment, Sundyberg, Sweden (1992).
20. G. E. Hauver, P. H. Netherwood, R. F. Benck, and L. J. Kecskes, "Ballistic performance of ceramic targets. *Proc. 13th Army Symp. Solid Mech*., Plymouth, MA (1993).
21. G. E. Hauver, P. H. Netherwood, R. F. Benck, and L. J. Kecskes. Enhanced ballistic performance of ceramics. *Proc. 19th Army Science Conf.*, Orlando, FL (1994).
22. G. E. Hauver, E. J. Rapacki, Jr., P. H. Netherwood, and R. F. Benck, "Interface Defeat of Long-Rod Projectiles by Ceramic Armor," Army Research Laboratory Report, ARL-TR-3590, Aberdeen Proving Ground, MD (2005).
23. M. L. Wilkins. Second progress report of light armor program. Report No. UCRL-50349, Lawrence Livermore National Laboratory, Livermore, CA (1967).
24. P. Lundberg, L. Holmberg, and B. Janzon. An experimental study of long rod penetration into boron carbide at ordnance and hyper velocities. *Proc. 17th Int. Symp. Ballistics,* **3**: 251-258, South Africa Ballistics Organization, South Africa (1988).
25. P. Lundberg, R. Renstrom, and B. Lundberg, "Impact of metallic projectiles on ceramic targets: transition between interface defeat and penetration," *Int. J. Impact Engng.*, **24**(3): 259-275 (2000).
26. P. Lundberg, R. Renstrom, and L. Holmberg. An experimental investigation of interface defeat at extended interaction time. *Proc. 19th Int. Symp. Ballistics*, **3**: 1463-1469, RAUG Land Systems, Switzerland (2001).
27. P. Lundberg and B. Lundberg, "Transition between interface defeat and penetration for tungsten projectiles and four silicon carbide materials," *Int. J. Impact Engng.*, **31**(7): 781-792 (2005).
28. P. Lundberg, R. Renstrom, and B. Lundberg. Impact of conical tungsten projectiles on flat silicon carbide targets: transition from interface defeat to penetration. *Int. J. Impact Eng*., **32**(11): 1842-1856 (2006).
29. O. Andersson, P. Lundberg, and R. Renstrom. Influence of confinement on the transition velocity of silicon carbide. *Proc. 23rd Int. Symp. Ballistics*, **2**: 1273-1280, Gráficas Couche, Madrid, Spain (2007).
30. T. J. Holmquist, C. E. Anderson, Jr, and T. Behner. Design, analysis and testing of an unconfined ceramic target to induce dwell. *22nd Int Symp Ballistics*, **2**: 860–68, DES*tech* Publications, Inc., Lancaster, PA (2005).

31. T. Behner, C. E. Anderson, Jr., T. J. Holmquist, M. Wickert, and D. W. Templeton. “Interface defeat for unconfined SiC ceramics. *Proc. 24th Int. Symp. Ballistics*, **1**: 35-42, DES*tech* Publications, Inc., Lancaster, PA (2008).

32. T. J. Holmquist, C. E. Anderson, Jr., and T. Behner. The effect of a copper buffer on interface defeat. *Proc. 24th Int. Symp. Ballistics*, **2**: 721-728, DES*tech* Publications, Inc., Lancaster, PA (2008).

33. C. E. Anderson, Jr., T. Behner, T. J. Holmquist, D. L. Orphal, and M. Wickert. Dwell, interface defeat, and penetration of long rods impacting silicon carbide. SwRI Report 18.12544/008, prepared for RDECOM-TARDEC, AMSRD-TAR-R, Warren, MI, April (2009).

34. T. J. Holmquist, C. E. Anderson, Jr., T. Behner, and D. L. Orphal. The mechanics of dwell and post-dwell penetration. *Advances in Applied Ceramics*, **109**(9): 467-479 (2010).

35. C. E. Anderson, Jr., “Dwell and post-dwell penetration of long rods on borosilicate glass targets,” ***Shock Compression of Condensed Matter—2009***, (M. L. Elert, *et al*., Eds.), AIP Conf. Series 1195, pp. 1447-1452, AIP, Melville, NY (2009).

36. C. E. Anderson, Jr., T. Behner, Dennis L. Orphal, T. J. Holmquist, V. Hohler, and M. Wickert. Interface defeat of long rods impacting borosilicate glass: experimental results. SwRI Report 18.12544/009, prepared for RDECOM-TARDEC, AMSRD-TAR-R, Warren, MI, February (2009).

APPENDIX

The appendix contains the table with the position-time data of the rod penetration in the ceramic as well as the X-ray pictures for each of the experiments.

Table A-1. X-ray Times

EXP.	X-ray Tube Number				
	1	2	3	4	5
11779	-13.139	6.966	21.915	37.140	51.982
11780	-12.322	7.765	22.717	37.902	52.754
11781	-12.199	7.809	22.780	38.015	52.886
11783	-13.002	6.982	21.973	37.221	52.094
11784	-13.302	6.726	21.731	36.873	51.793
11790	-13.633	6.403	21.351	41.530	66.402
11791	-14.833	5.217	20.198	40.281	65.255
11793	-14.960	5.061	20.057	40.245	65.147
11794	-13.842	6.159	21.070	41.324	66.156
11795	-12.569	7.615	22.478	42.641	67.579
11796	-14.640	5.439	20.348	40.565	65.460
11797	-17.855	12.205	22.143	37.228	62.232
11798	-17.675	12.389	22.260	37.495	62.391
11799	-18.670	11.417	21.358	36.493	61.421
11800	-23.182	6.902	16.821	31.992	56.886
11801	57.205	7.195	17.120	32.316	-22.651
11804	56.312	6.410	16.303	31.440	-23.531
11805	61.720	11.619	21.503	36.640	-18.243
11807	92.701	2.659	27.596	52.696	-37.300
11808	97.877	7.766	32.722	57.909	-32.095
11809	92.067	1.993	26.940	52.081	-37.888
11810	97.506	7.343	32.348	57.515	-32.477
11811	121.579	31.396	56.447	81.547	-8.449
11812	84.228	14.116	39.095	54.263	-25.760
11814	75.087	14.944	29.967	45.066	-24.907
11815	77.465	17.305	32.314	47.409	-22.579
11816	115.597	25.563	50.596	75.906	-14.310
11817	63.556	13.417	23.406	38.629	-16.384
11818	62.968	12.971	22.953	38.063	-16.966
11819	62.280	12.146	22.077	37.189	-17.697
11820	63.269	13.199	23.165	38.285	-16.633
11821	60.629	10.461	20.472	35.603	-19.427
11822	69.125	9.156	29.118	44.181	-10.792

Table A-1. X-ray Times (Cont'd)

EXP	**X-ray Tube Number**				
	1	**2**	**3**	**4**	**5**
11928	102.016	11.963	36.882	62.077	-28.144
11929	84.411	14.558	39.375	54.582	-25.574
11930	94.662	4.675	29.556	54.688	-35.434
11931	94.991	15.085	39.836	59.971	-25.123
11932	91.495	11.354	36.311	56.290	-28.663
11933	101.169	11.064	35.974	61.135	-28.966
11934	94.964	14.931	39.846	55.067	-25.140
11935	84.725	24.723	49.618	64.819	-15.390

Table A-2. Position-Time Data for 30° Experiments

	30° CP				30° CP		
	t after imp. [µs]	Pen. depth [mm]	Rod length [mm]		*t* after imp. [µs]	Pen. depth [mm]	Rod length [mm]
11790	66.40	-	-	11794	66.16	-	-
	41.53	-	15.68		41.32	-	11.91
	21.35	-	43.04		21.07	-	38.96
	6.40	-	62.25		6.16	-	62.35
	-13.63	-2.30	70.10		-13.84	-2.30	70.13
11784	51.79	12.31	10.81	11796	65.46	-	-
	36.87	3.12	14.61		40.56	20.48	30.42
	21.73	-	-		20.35	4.85	46.10
	6.73	-	-		5.44	-	-
	-13.30	-2.30	70.05		-14.64	-2.30	70.16
11783	52.09	15.60	10.82	11780	52.75	-	-
	37.22	4.92	21.86		37.90	22.95	36.19
	21.97	-	-		22.72	10.61	47.60
	6.98	-	-		7.77	-	-
	-13.00	-2.30	70.01		-12.32	-2.30	70.06
11791	65.25	-	-	11795	67.58	-	-
	40.28	20.01	32.43		42.64	20.96	-
	20.20	8.05	49.92		22.48	6.58	43.72
	5.22	-	-		7.62	-	-
	-14.83	-2.30	7-		-12.57	-2.30	70.03
11793	65.15	23.14	0.76	11779	51.98	-	-
	40.25	6.98	-		37.14	27.78	41.08
	20.06	-	-		21.92	13.85	51.23
	5.06	-	-		6.97	-	-
	-14.96	-2.30	70.02		-13.14	-2.30	70.08
11781	52.89	30.65	22.92				
	38.02	17.37	32.01				
	22.78	12.75	42.88				
	7.81	-	-				
	-12.20	-2.30	69.98				

Table A-3. Position-Time Data for 45° Experiments

	45° CP				45° CP		
	t after imp. [µs]	Pen. depth [mm]	Rod length [mm]		*t* after imp. [µs]	Pen. depth [mm]	Rod length [mm]
11821	-19.43	-2.82	70.07	11802	-15.52	-2.82	70.05
	35.60	9.55	30.90		39.44	17.03	28.75
	20.47	-	-		24.25	7.09	42.25
	10.46	-	-		14.32	-	-
	60.63	27.29	13.97		64.33	-	-
11805	-18.24	-2.82-	70.04	11797	62.23	26.61	-
	36.64	-	19.32		37.23	8.11	22.85
	21.50	-	40.58		22.14	-	-
	11.62	-	55.39		12.20	-	-
	61.72	-	-		-17.85	-2.82	70.06
11798	62.39	15.79	-	11818	-16.97	-2.82	70.06
	37.49	4.51	20.73		38.06	-	16.54
	22.26	-	-		22.95	-	37.85
	12.39	-	-		12.97	-	53.39
	-17.68	-2.82	70.01		62.97	-	-
		45° bare				**45° bare**	
11930	-33.73	-	70.05	11931	-25.53	-	70.02
	56.40	-	18.92		59.56	18.61	21.67
	31.26	-	40.95		39.43	7.79	33.38
	6.38	-	63.57		14.68	-1.35	51.71
	96.37	-	-		94.58	-	-
11928	-30.61	-	70.00	11929	-25.35	-	70.17
	59.61	4.76	14.34		54.80	18.00	23.26
	34.41	-	31.34		39.59	9.33	32.46
	9.49	-	54.89		14.78	-	48.45
	99.55	-	-		84.63	-	-
11933	-28.32	-	69.98				
	61.78	8.73	15.79				
	36.62	-	31.33				
	11.71	-	55.34				
	101.81	-	-				
11932	-28.23	-	70.10				
	56.72	5.87	15.51				
	36.74	-	30.29				
	11.79	-	56.16				
	91.93	-	-				

Table A-4. Position-Time Data for 60° Experiments

	60° CP				60° CP		
	t after imp. [µs]	Pen. depth [mm]	Rod length [mm]		*t* after imp. [µs]	Pen. depth [mm]	Rod length [mm]
11819	-17.70	-4.00	70.09	11807	-37.30	-	70.12
	37.19	18.23	38.63		52.70	-	21.39
	22.08	8.11	50.55		27.60	-	44.33
	12.15	-	-		2.66	-	67.33
	62.28	-	-		92.70	-	-
11804	-23.53	-	70.15	11808	-32.10	-	70.02
	31.44	11.11	37.60		57.91	-	17.61
	16.30	-	-		32.72	-	40.88
	6.41	-	-		7.77	-	65.06
	56.31	29.72	19.92		97.88	-	-
11803	-20.18	-4.00	70.15	11809	-37.89	-	70.18
	34.79	14.97	35.70		52.08	-	17.88
	19.59	-	-		26.94	-	42.42
	9.67	-	-		1.99	-	66.41
	59.68	29.41	12.86		92.07	-	-
11800	56.89	21.44	8.61	11810	-32.48	-	70.09
	31.99	5.62	-		57.51	-	11.35
	16.82	-	-		32.35	-	36.46
	6.90	-	-		7.34	-	61.99
	-23.18	-4.00	70.03		97.51	-	-
11801	-22.65	-4.01	70.11	11812	-25.76	-	70.06
	32.32	4.94	-		54.26	-	10.09
	17.12	-	-		39.10	-	26.50
	7.20	-	-		14.12	-	54.26
	57.21	21.45	7.12		84.23	-	-
11799	61.42	29.12	7.12	11814	-24.91	-	69.90
	36.49	11.88	28.37		45.07	-	10.44-
	21.36	-	-		29.97	-	31.11
	11.42	-	-		14.94	-	52.54
	-18.67	-4.00	70.07		75.09	-	-
11817	-16.38	-4.00	70.10	11815	-22.58	-	69.97
	38.63	23.83	36.74		47.41	20.67	18.81
	23.41	10.19	47.31		32.31	9.25	30.05
	13.42	-	-		17.30	-	-
	63.56	-	-		77.46	-	-
11820	-16.63	-4.00	70.06	11822	-10.79	-	70.00
	38.29	17.15	33.57		44.18	6.25	23.33
	23.17	-	-		29.12	-	-
	13.20	-	-		9.16	-	-
	63.27	31.67	10.45		69.12	26.59	-

Table A-5. Position-Time Data for 0° Experiments

	0° bare		
	t after imp. [μs]	Pen. depth [mm]	Rod length [mm]
11811	-8.45	-	69.96
	81.55	-	28.36
	56.45	-	50.27
	31.40	-	61.78
	121.58	-	-
11816	-14.31	-	69.97
	75.91	13.66	10.05
	50.60	6.69	27.00
	25.56	5.97	49.83
	115.60	-	-

In the pages that follow, there are two figures for each experiment: the flash X-rays, and a graph of the penetration-time data and a graph of the rod length versus time data. Table A-1 provides the times of the flash X-rays. The experimental data points (solid symbols), with times adjusted so that time 0 is impact onto the target, are listed in Tables A-2, A-3, A-4, and A-5. Dashed lines are drawn to connect the data points. Open symbols denote values that have been calculated, as described in the main body of the report.

Solid lines denote the range over which a linear regression analyses were conducted to determine the penetration depth as a function of time, and rod length as a function of time. The slopes of these regression analyses provide the penetration velocity and the consumption velocity, respectively. Dotted lines represent the results of analyses to assist in estimating the time at which dwell transitioned to penetration, as described in the main body of the report.

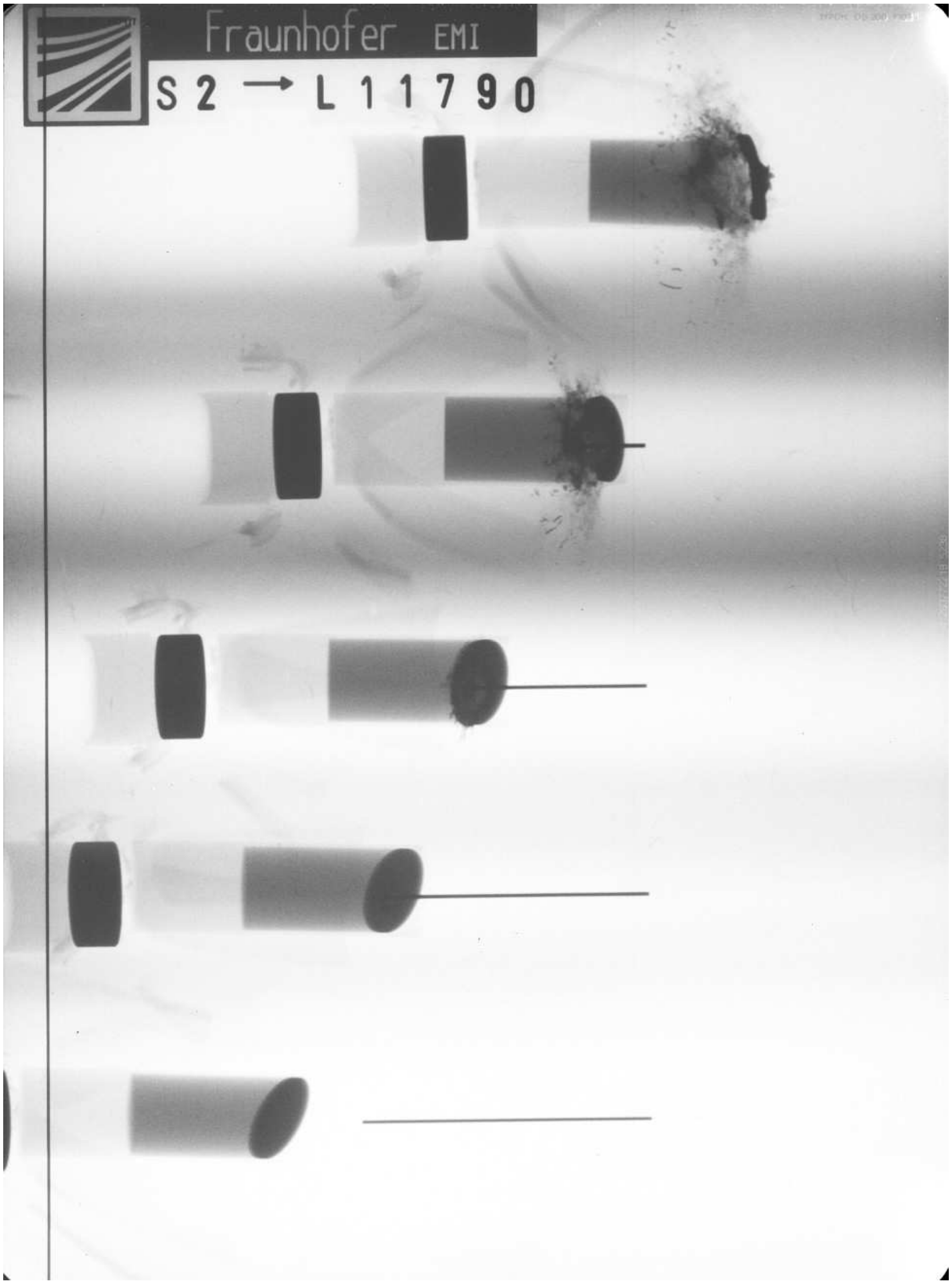

Figure A-1. X-ray picture for Exp. 11790: 30° with buffer, v_p = 1.419 km/s.

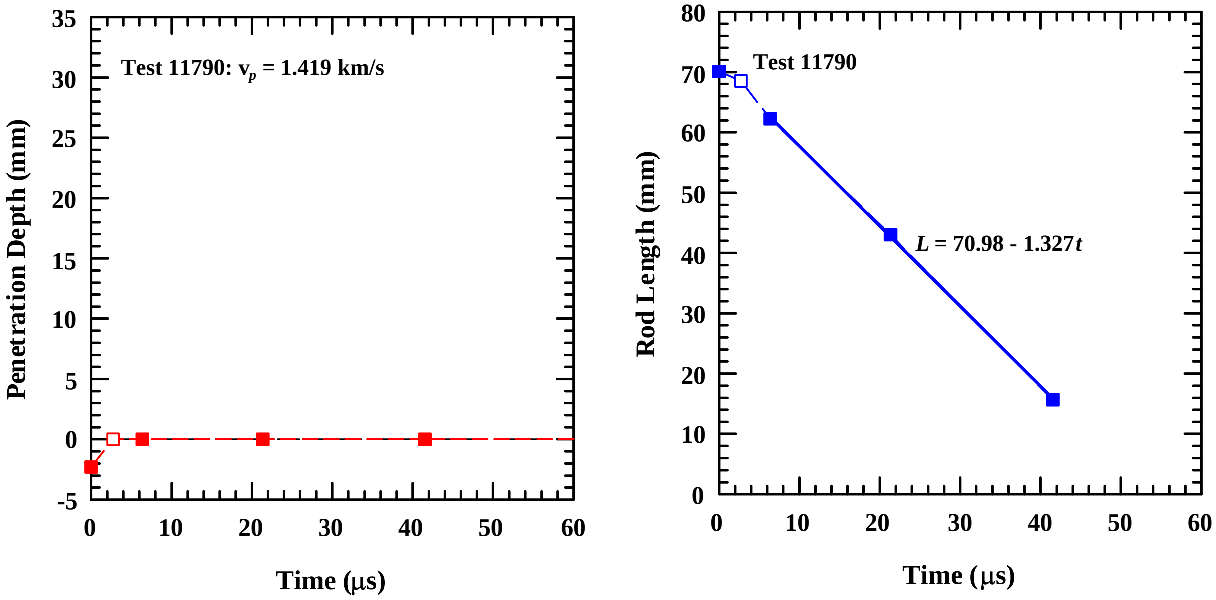

Figure A-2. Position and rod length vs. time for Exp. 11790: 30° with buffer, v_p = 1.419 km/s.

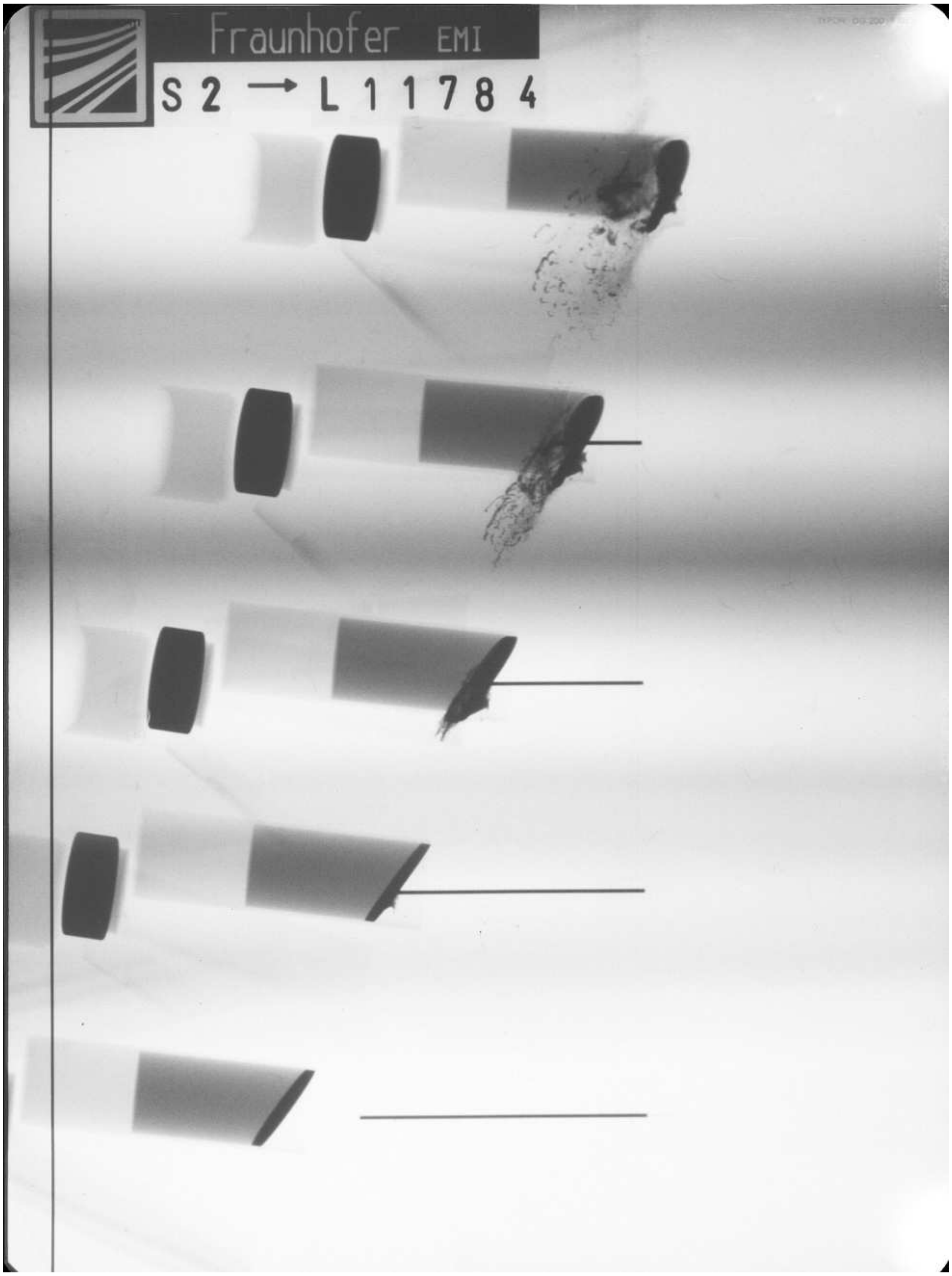

Figure A-3. X-ray picture for Exp. 11784: 30° with buffer, v_p = 1.433 km/s.

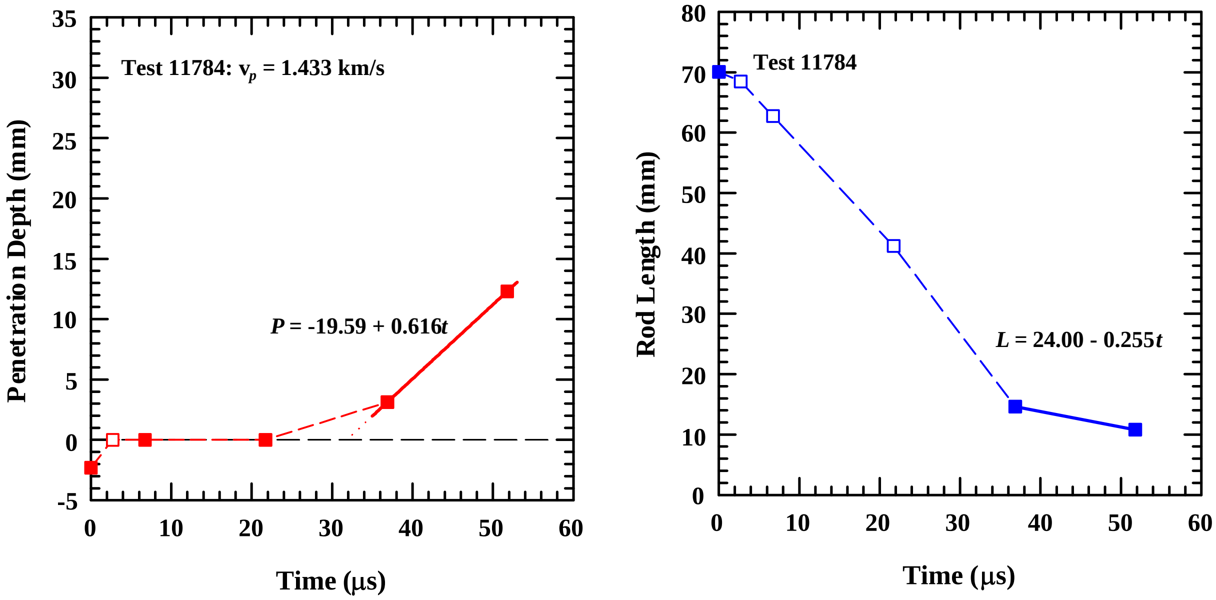

Figure A-4. Position and rod length vs. time for Exp. 11784: 30° with buffer, v_p = 1.433 km/s.

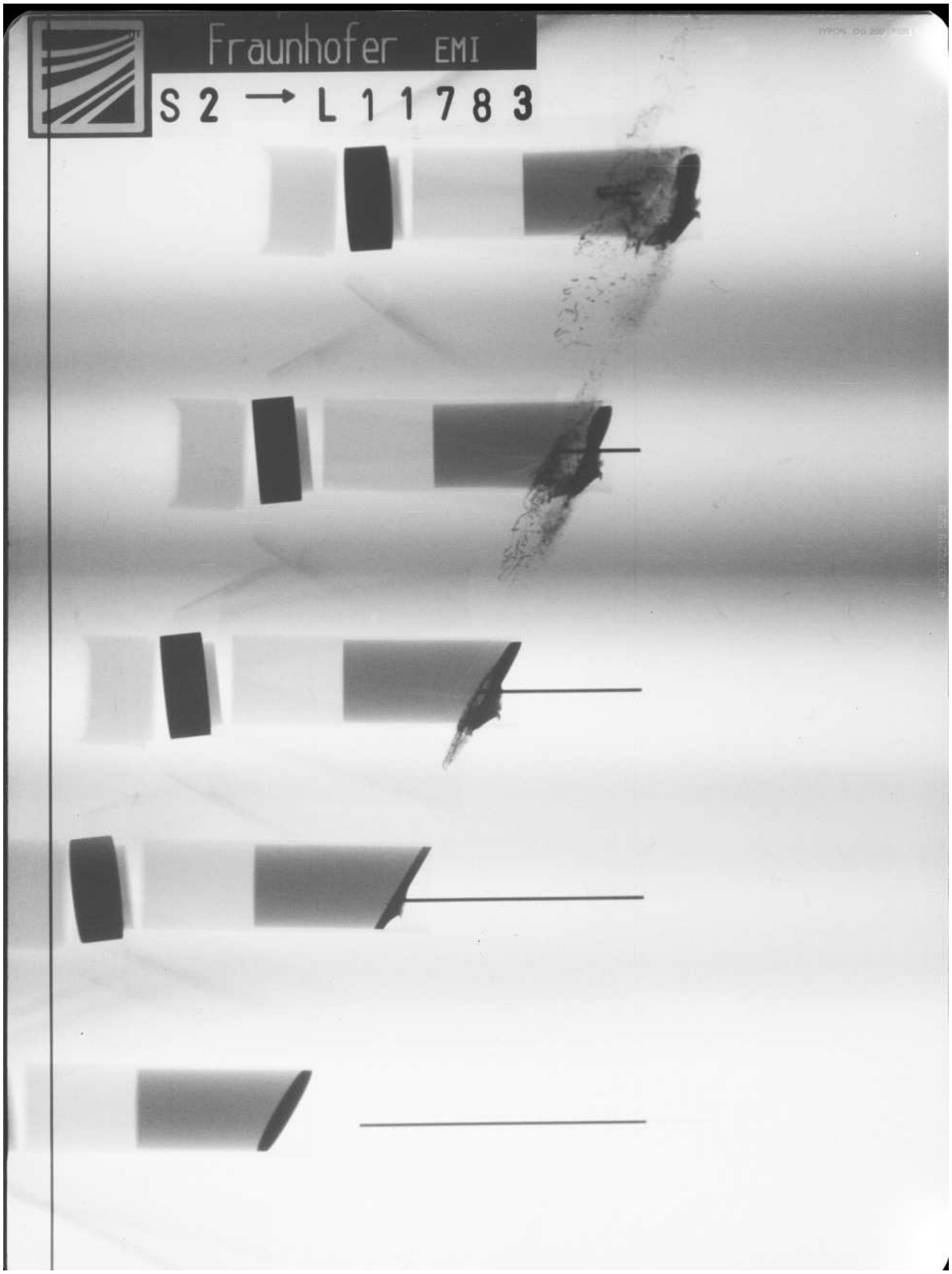

Figure A-5. X-ray picture for Exp. 11783: 30° with buffer, v_p = 1.479 km/s.

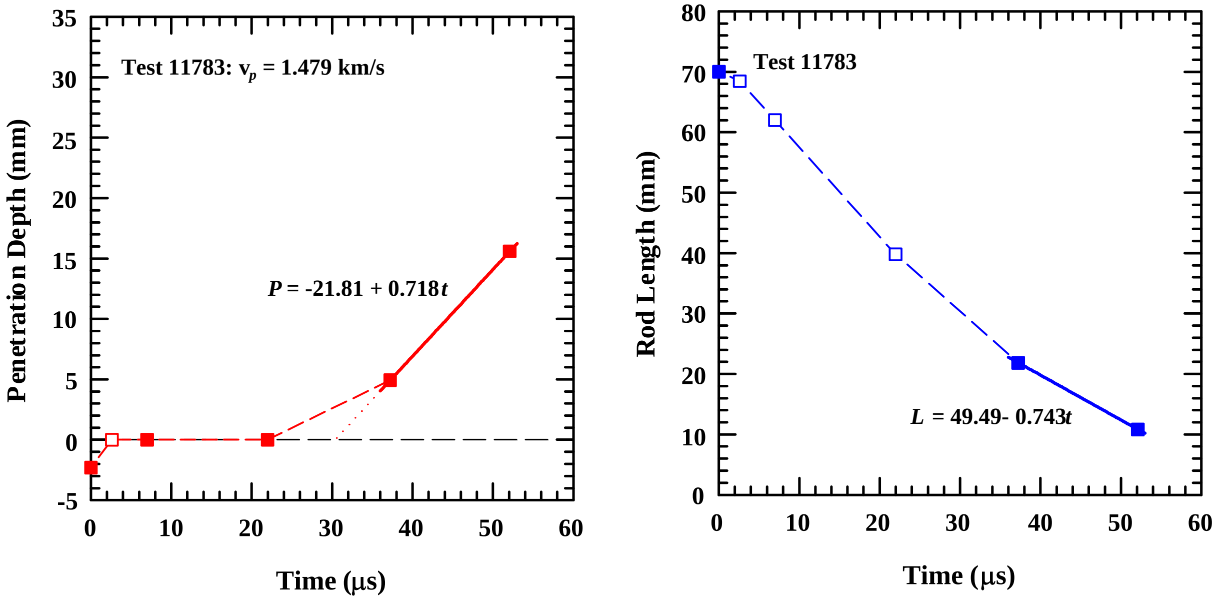

Figure A-6. Position and rod length vs. time for Exp. 11783: 30° with buffer, v_p = 1.479 km/s.

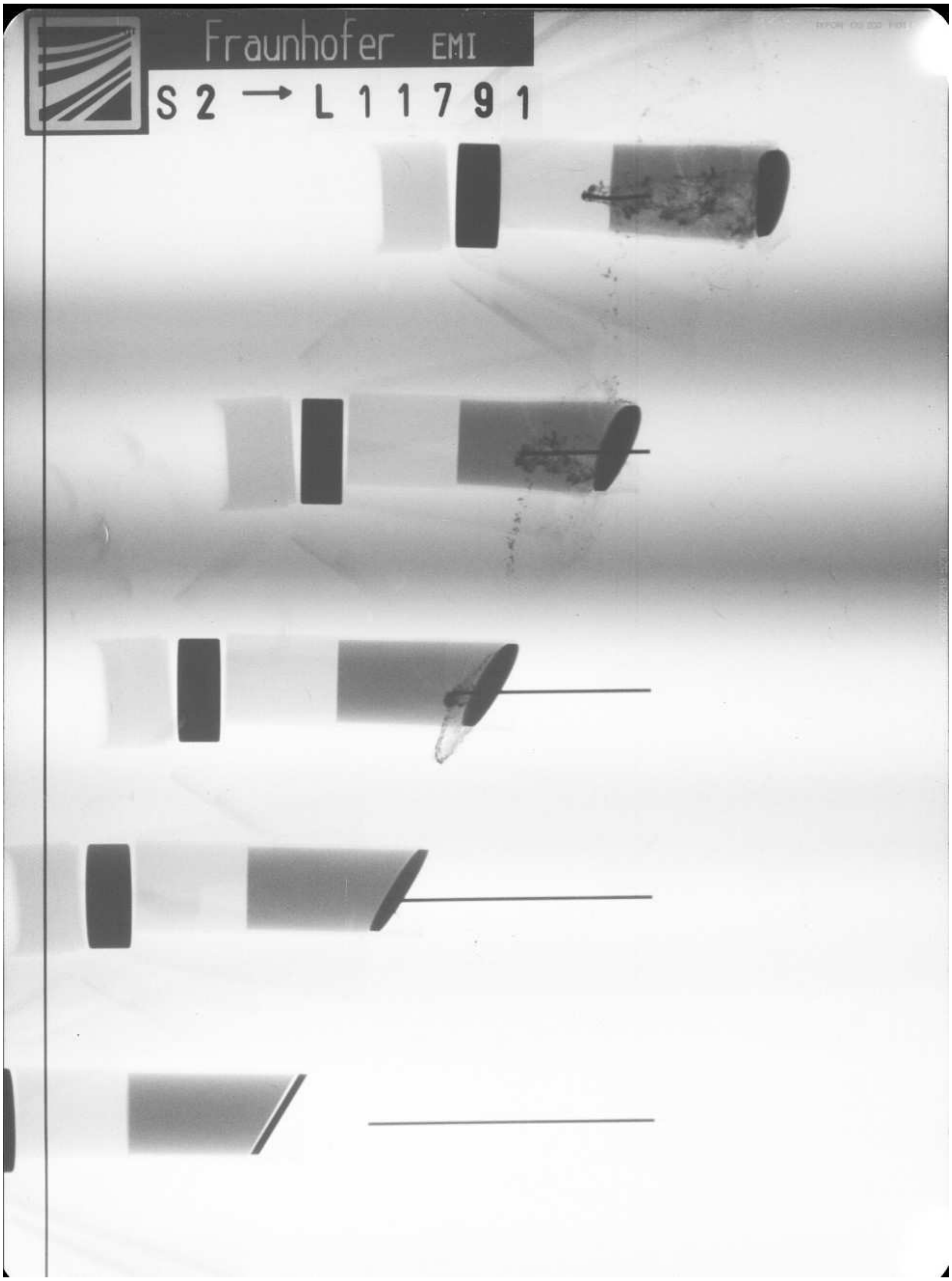

Figure A-7. X-ray picture for Exp. 11791: 30° with buffer, v_p = 1.481 km/s.

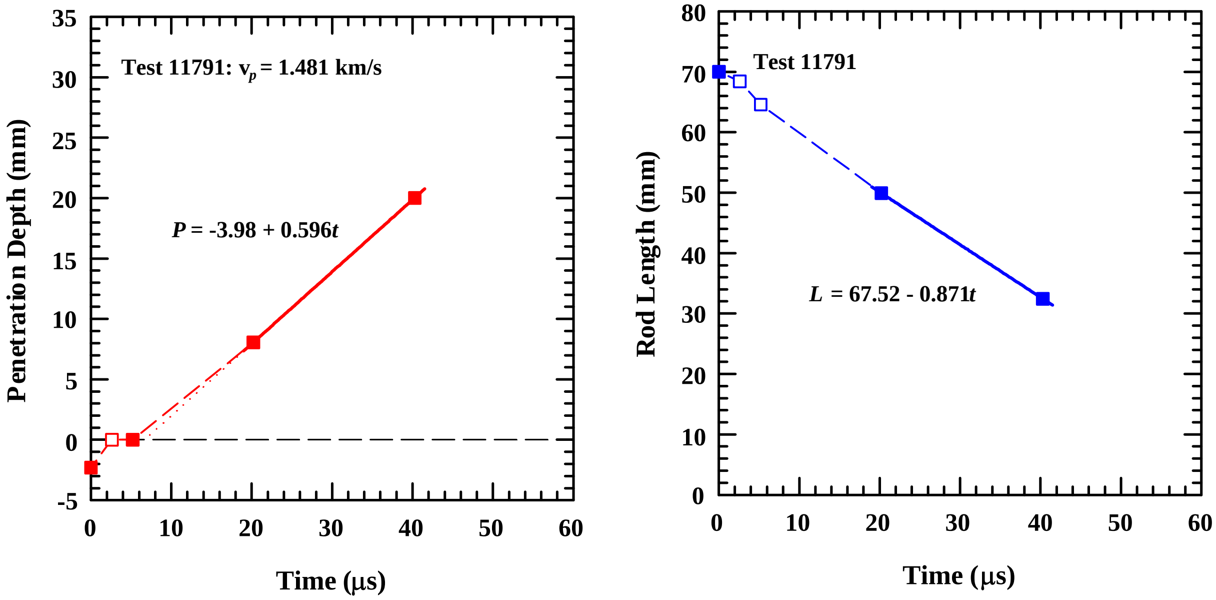

Figure A-8. Position and rod length vs. time for Exp. 11791: 30° with buffer, v_p = 1.481 km/s.

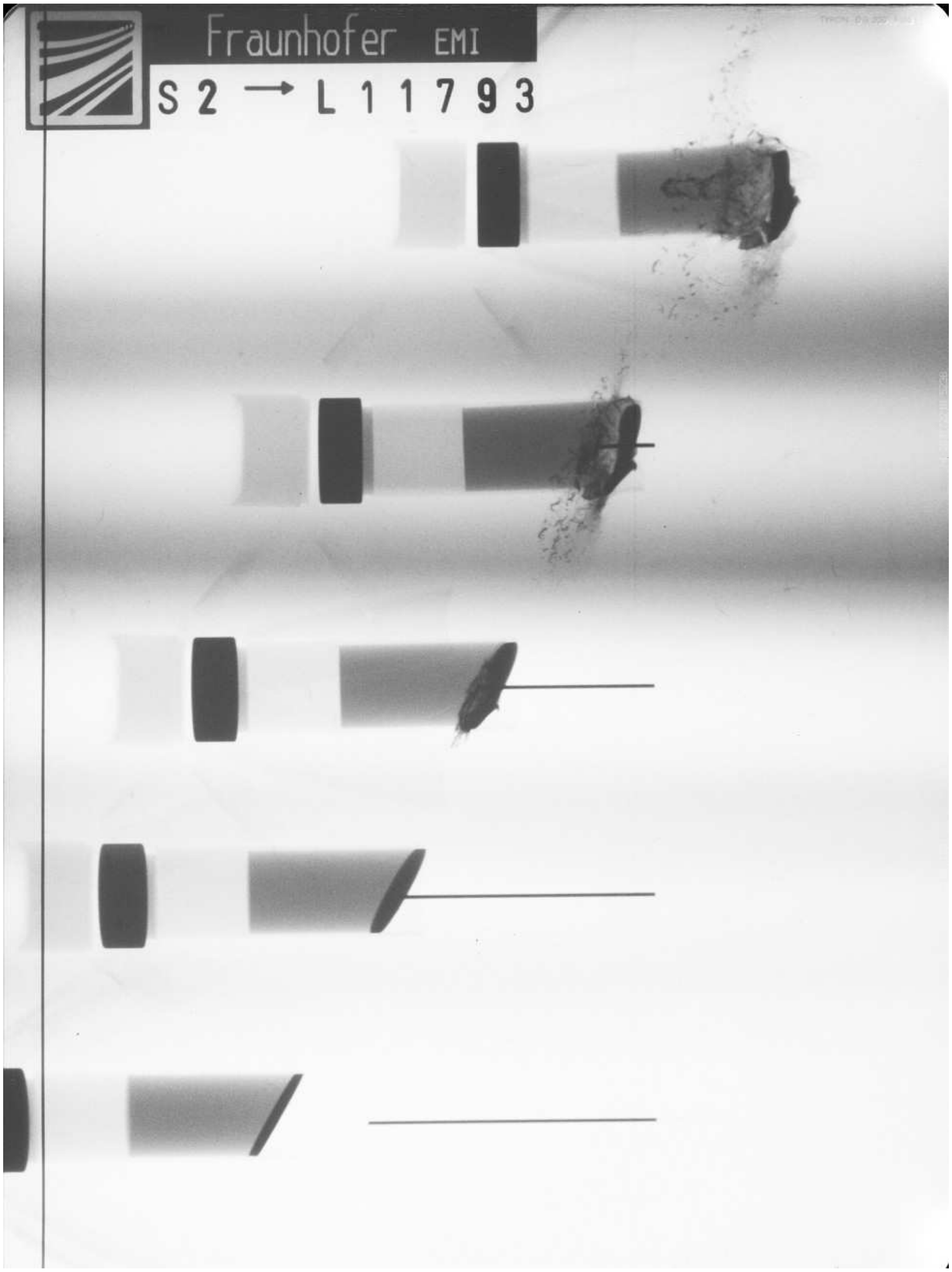

Figure A-9. X-ray picture for Exp. 11793: 30° with buffer, v_p = 1.499 km/s.

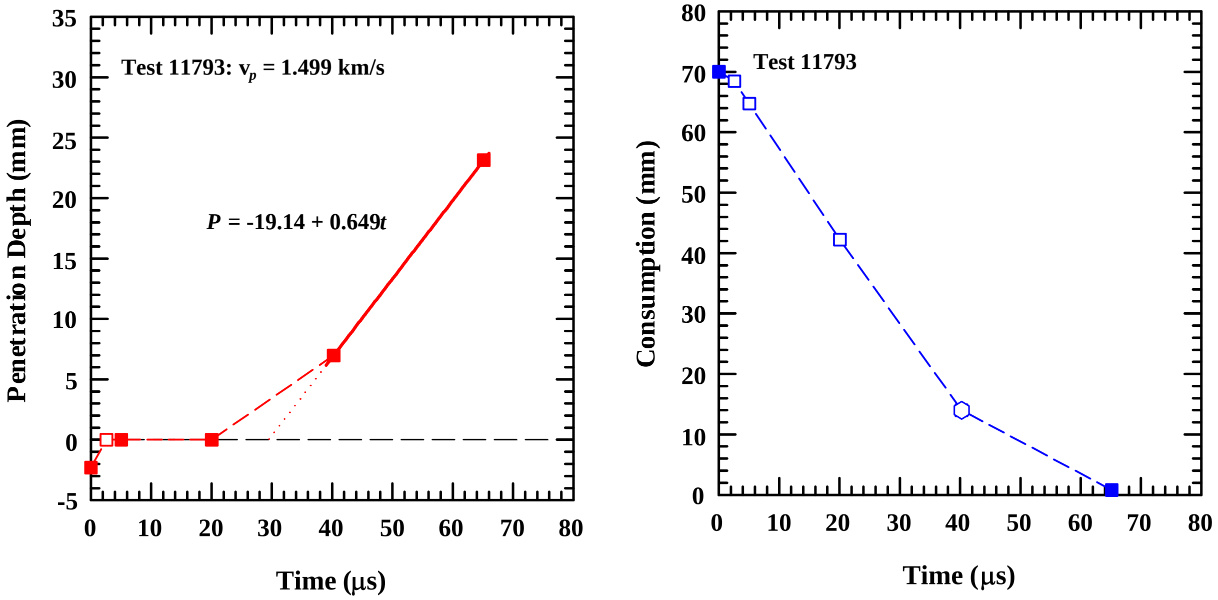

Figure A-10. Position and rod length vs. time for Exp. 11793: 30° with buffer, v_p = 1.499 km/s.

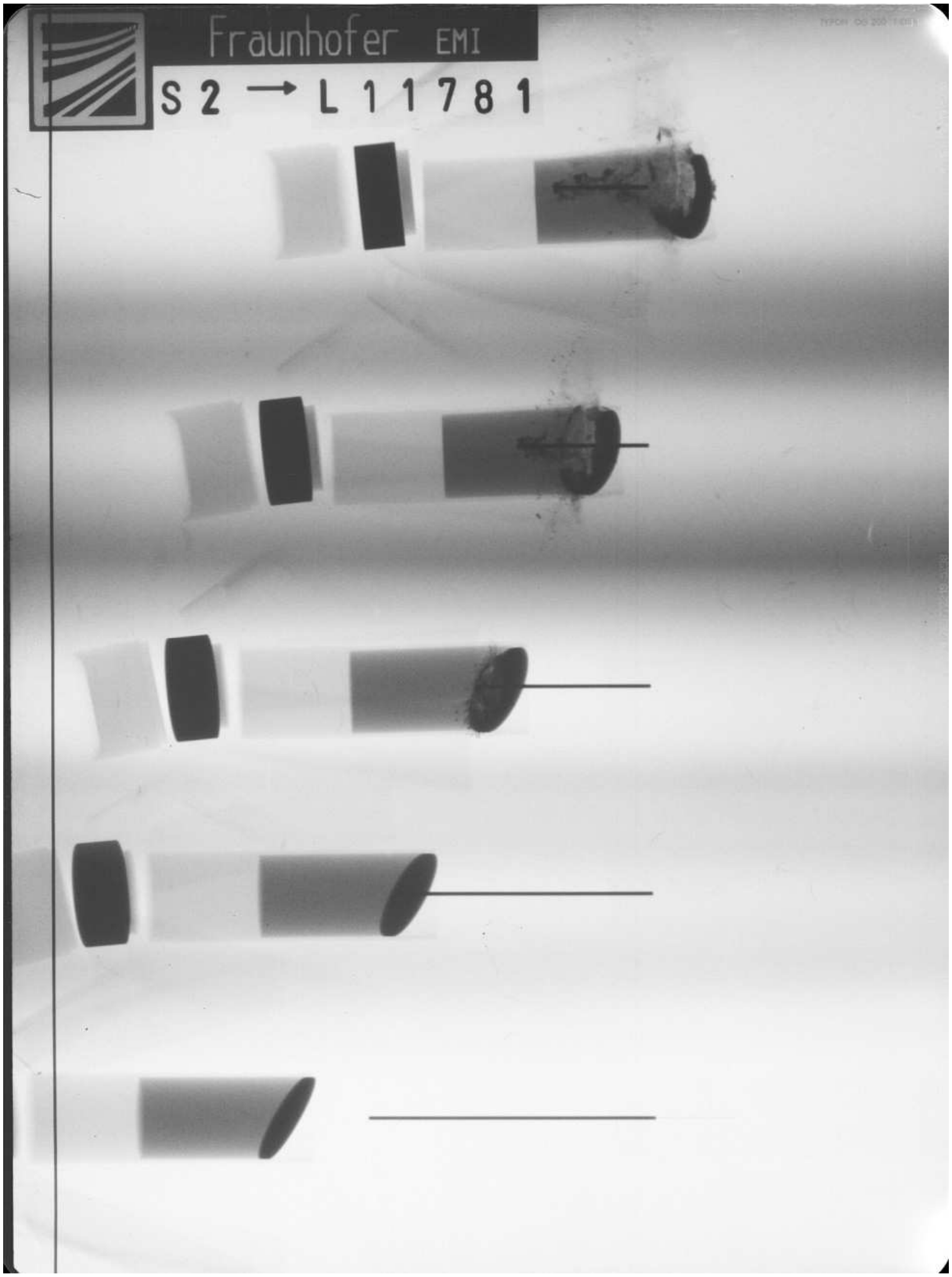

Figure A-11. X-ray picture for Exp. 11781: 30° with buffer, v_p = 1.514 km/s.

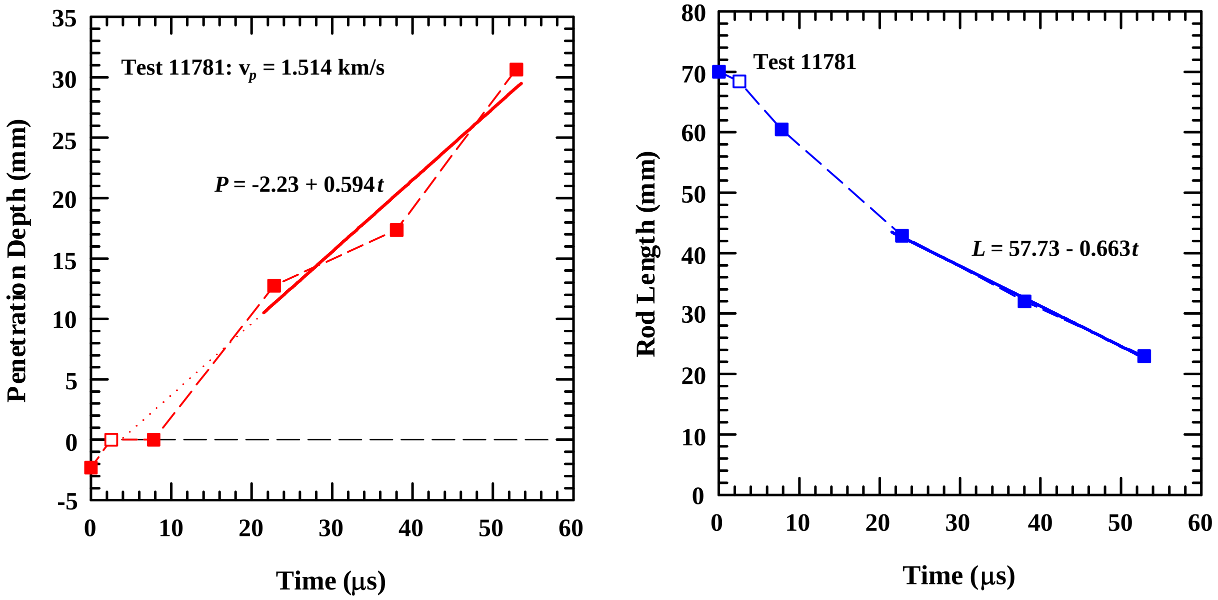

Figure A-12. Position and rod length vs. time for Exp. 11781: 30° with buffer, v_p = 1.514 km/s.

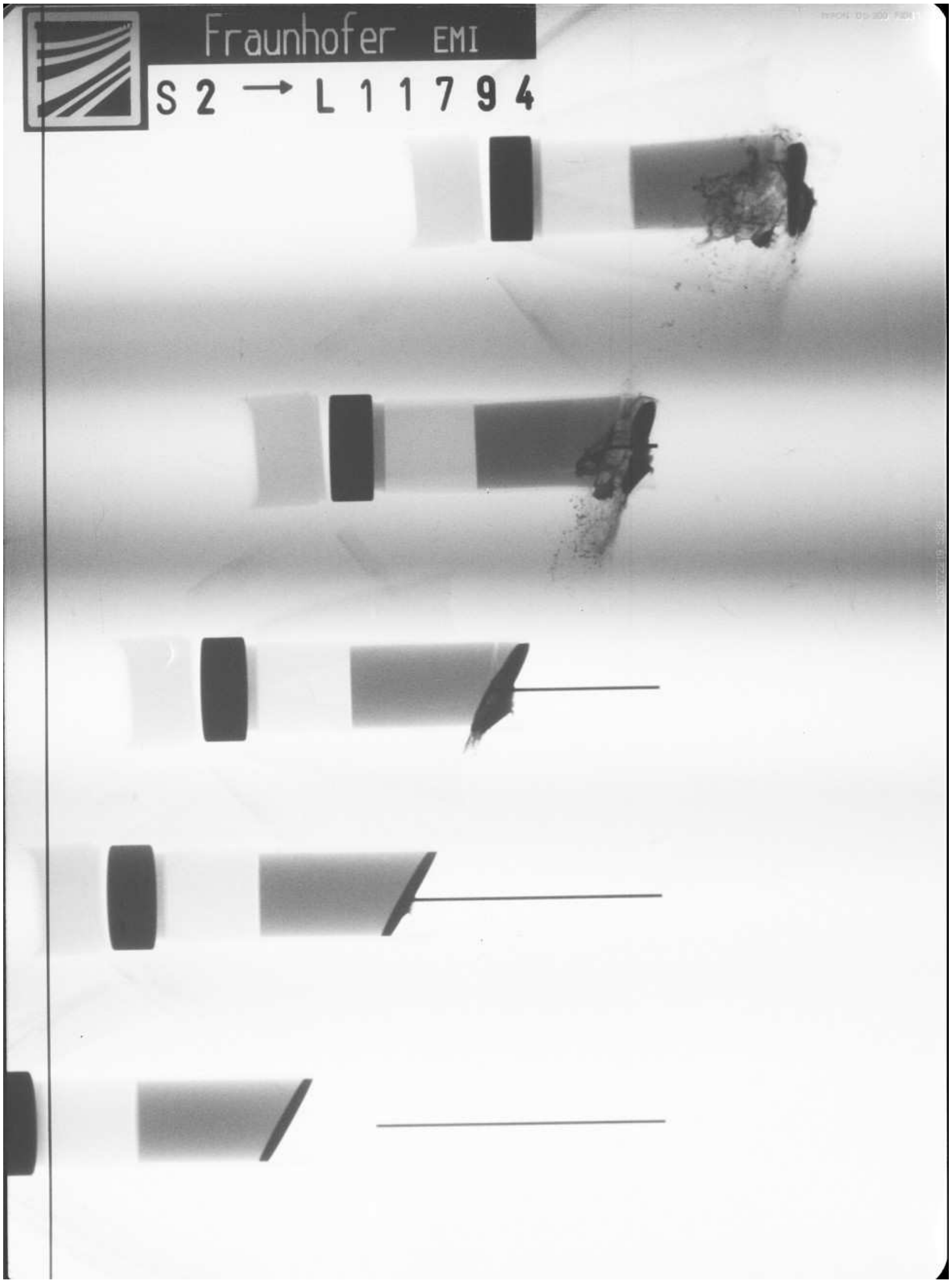

Figure A-13. X-ray picture for Exp. 11794: 30° with buffer, v_p = 1.529 km/s.

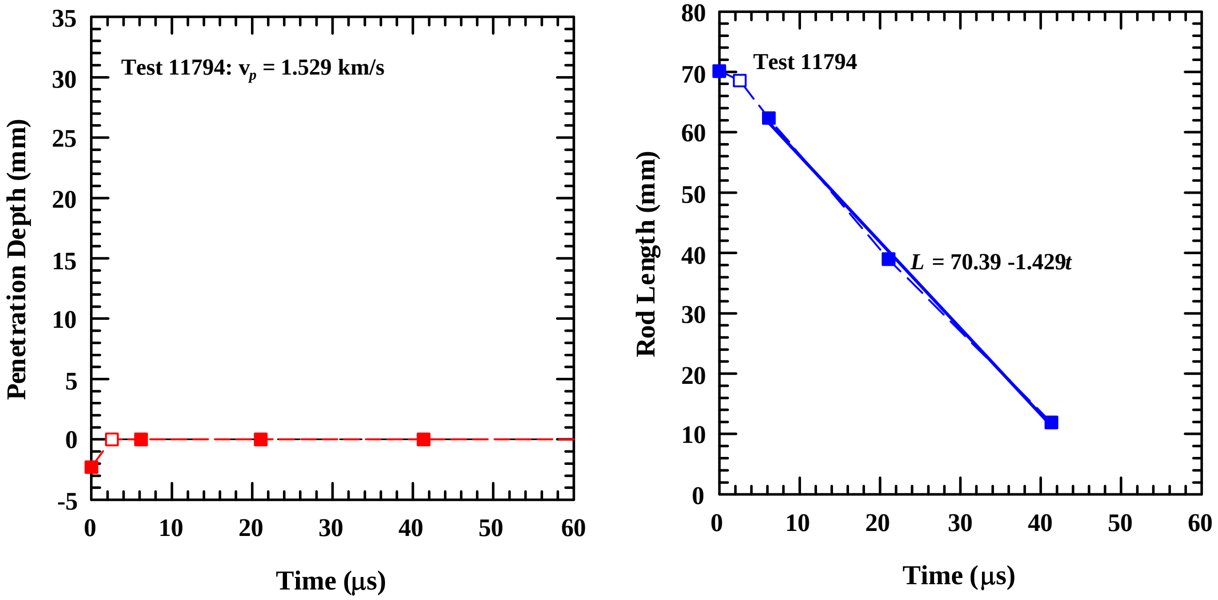

Figure A-14. Position and rod length vs. time for Exp. 11794: 30° with buffer, v_p = 1.529 km/s.

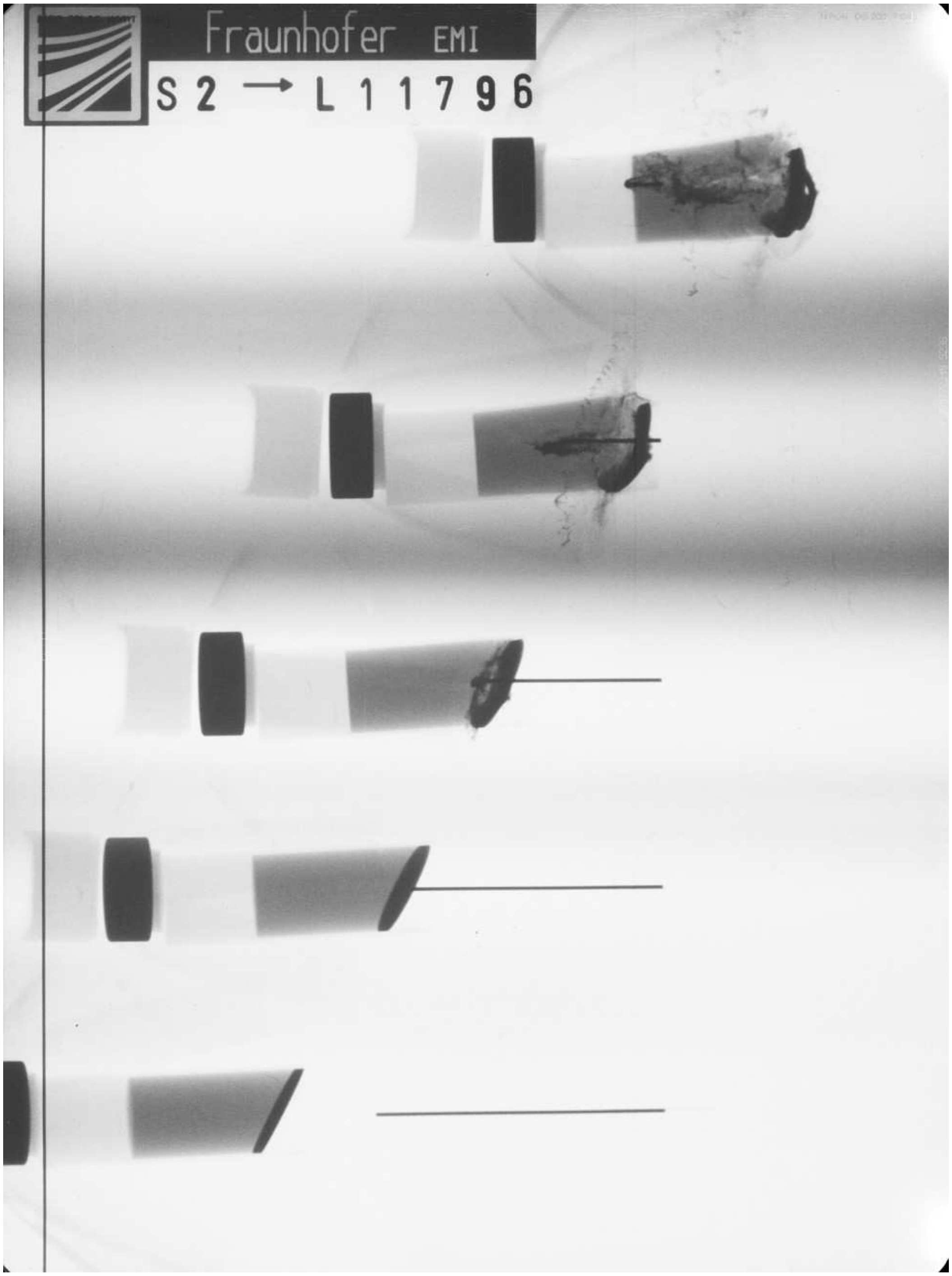

Figure A-15. X-ray picture for Exp. 11796: 30° with buffer, v_p = 1.529 km/s.

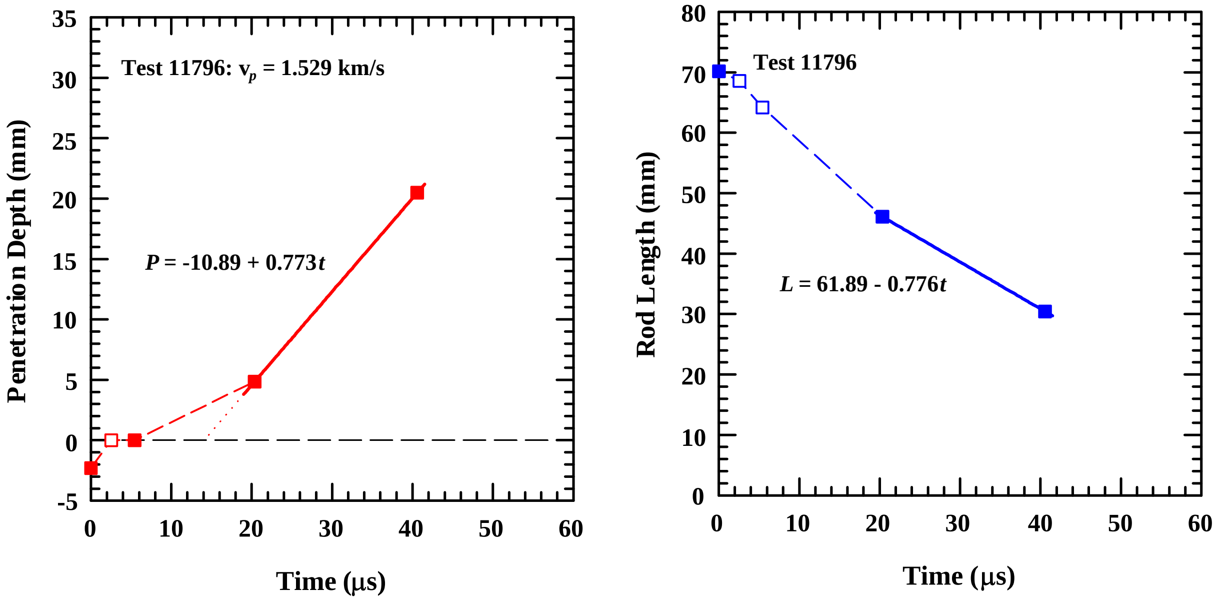

Figure A-16. Position and rod length vs. time for Exp. 11796: 30° with buffer, v_p = 1.529 km/s.

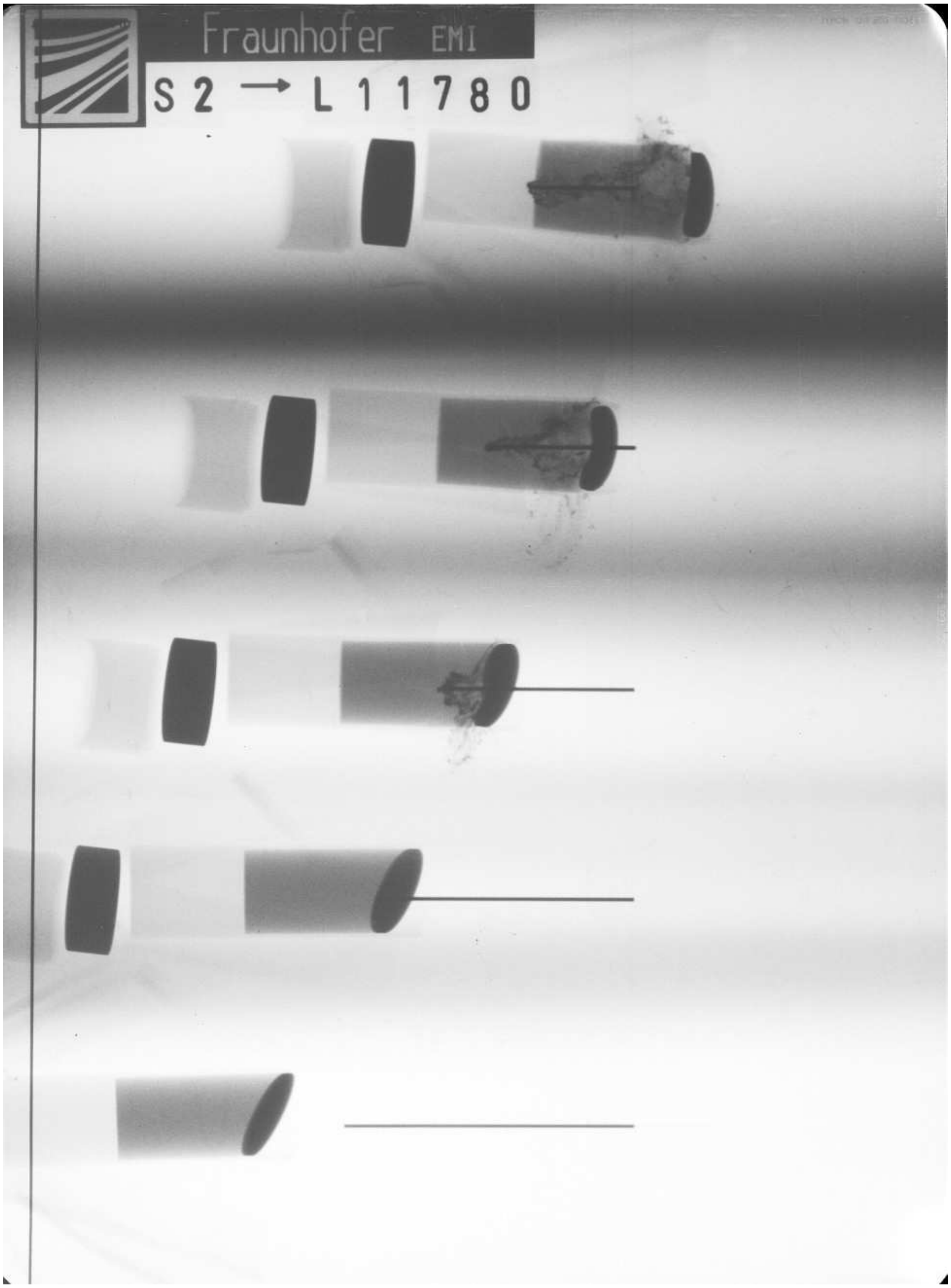

Figure A-17. X-ray picture for Exp. 11780: 30° with buffer, v_p = 1.548 km/s.

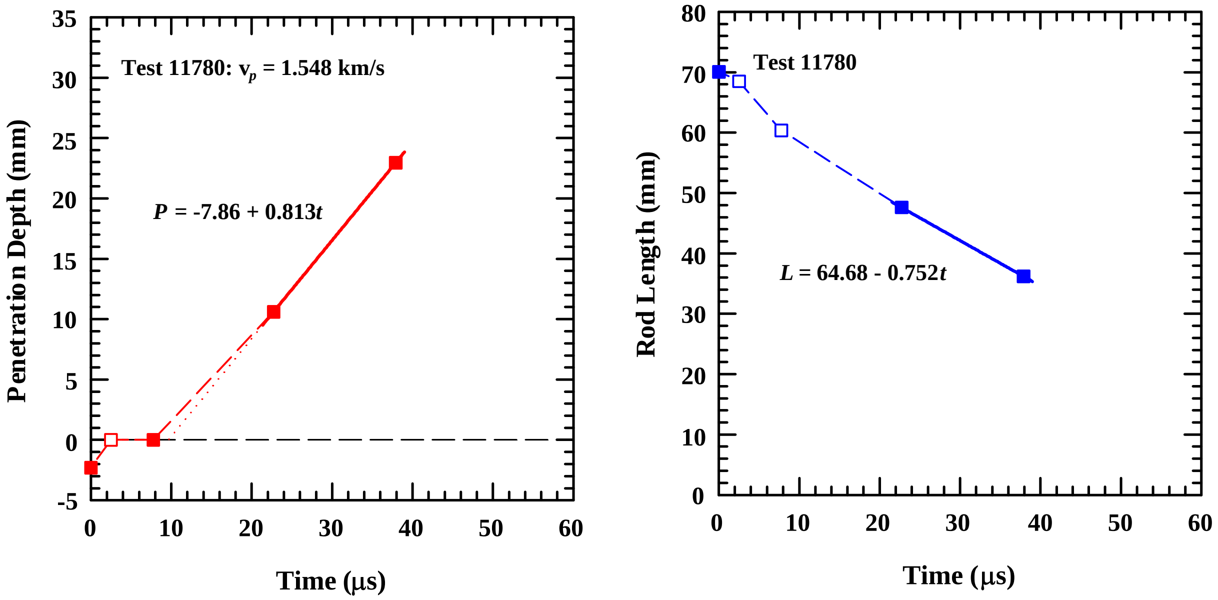

Figure A-18. Position and rod length vs. time for Exp. 11780: 30° with buffer, v_p = 1.548 km/s.

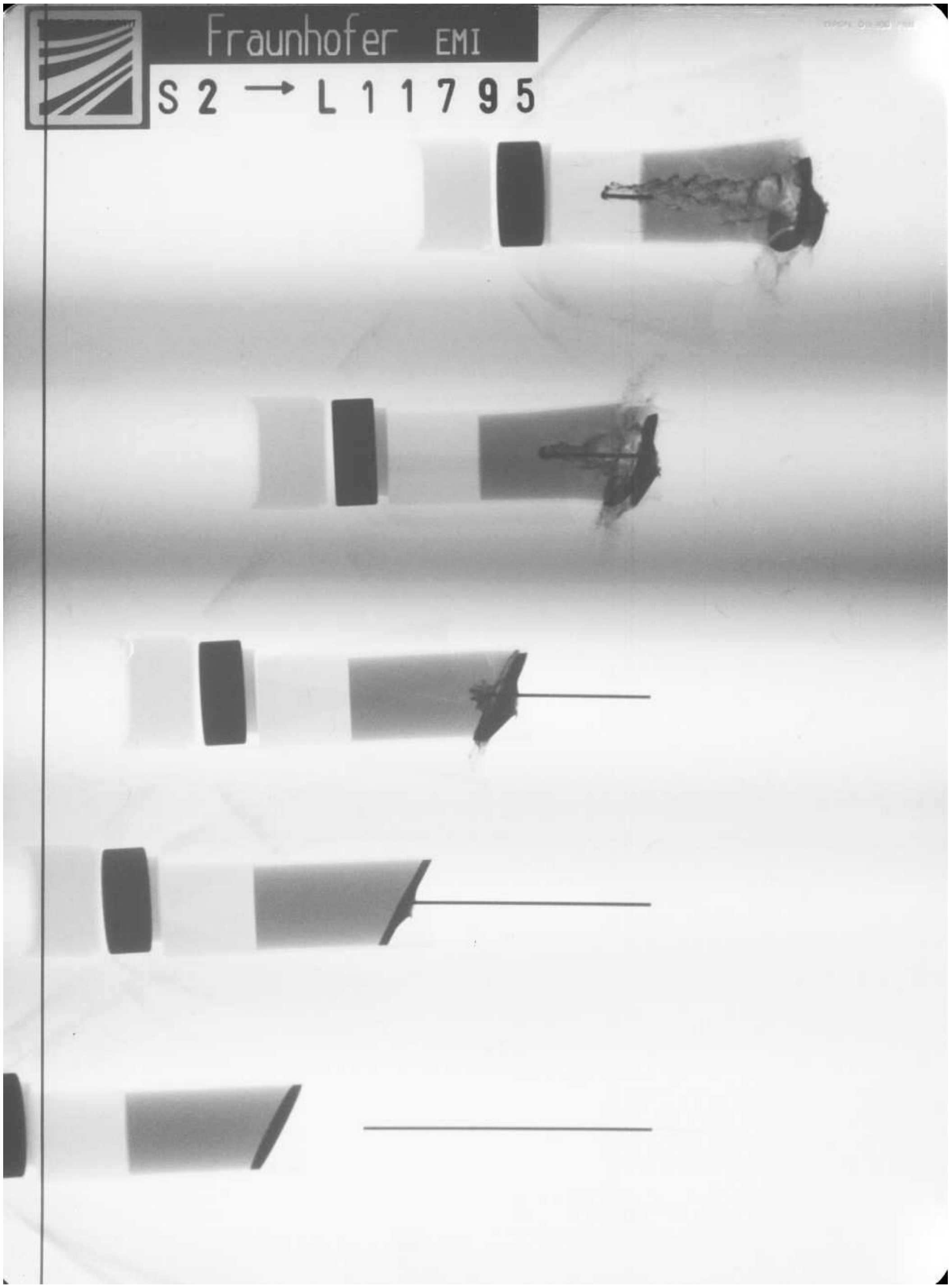

Figure A-19. X-ray picture for Exp. 11795: 30° with buffer, v_p = 1.552 km/s.

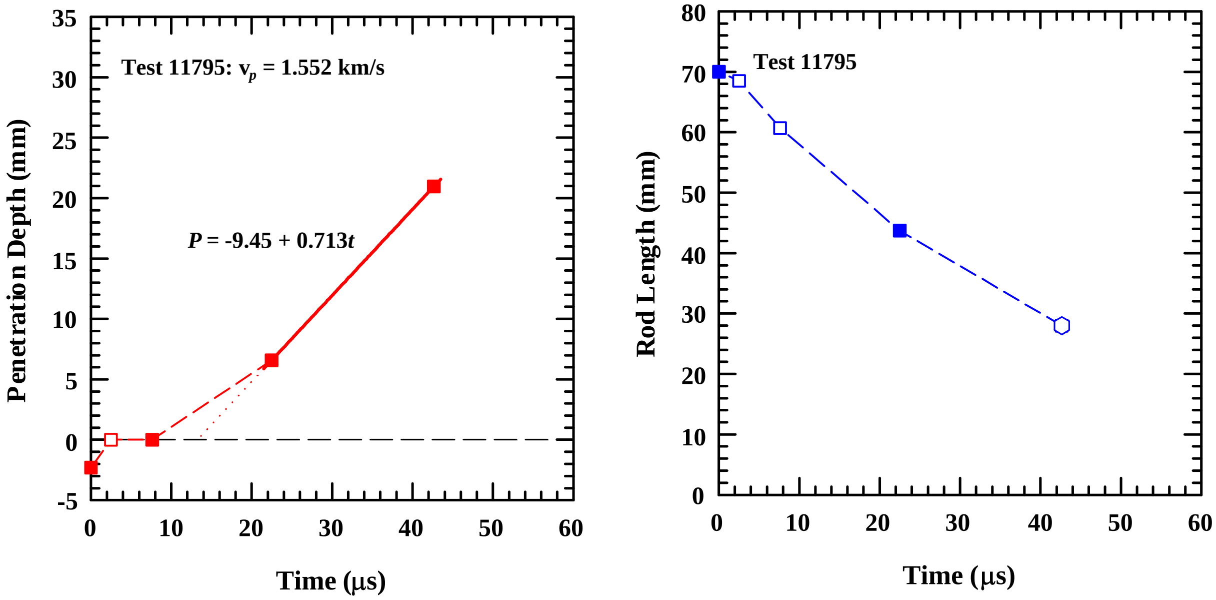

Figure A-20. Position and rod length vs. time for Exp. 11795: 30° with buffer, v_p = 1.552 km/s.

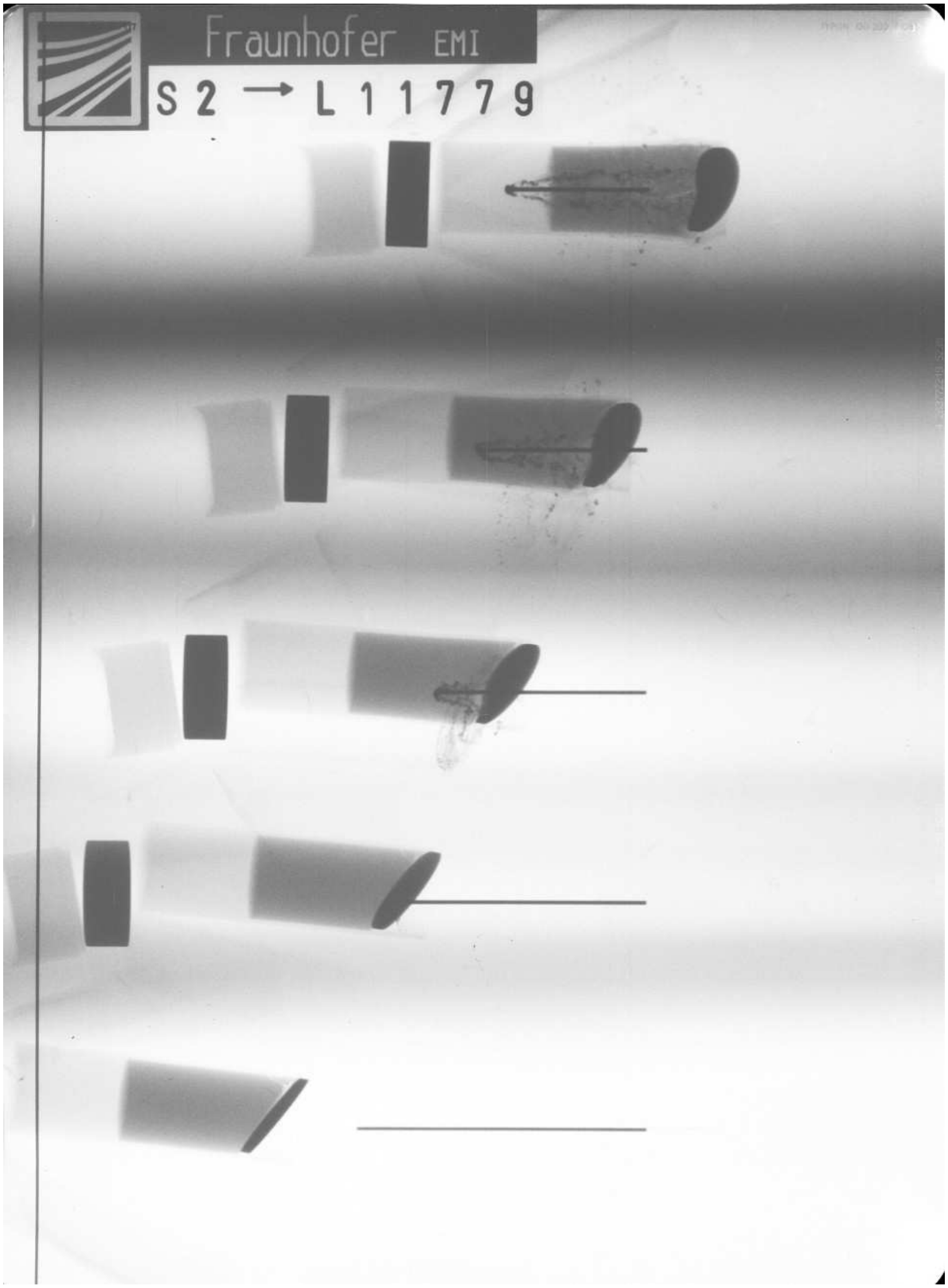

Figure A-21. X-ray picture for Exp. 11779: 30° with buffer, v_p = 1.588 km/s.

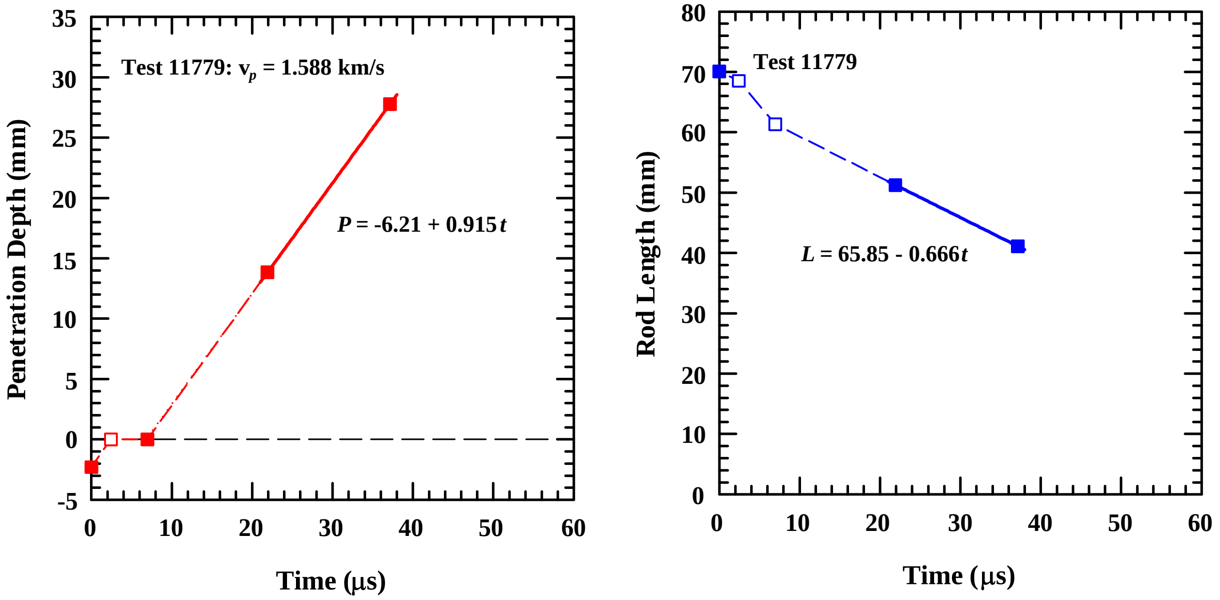

Figure A-22. Position and rod length vs. time for Exp. 11779: 30° with buffer, v_p = 1.588 km/s.

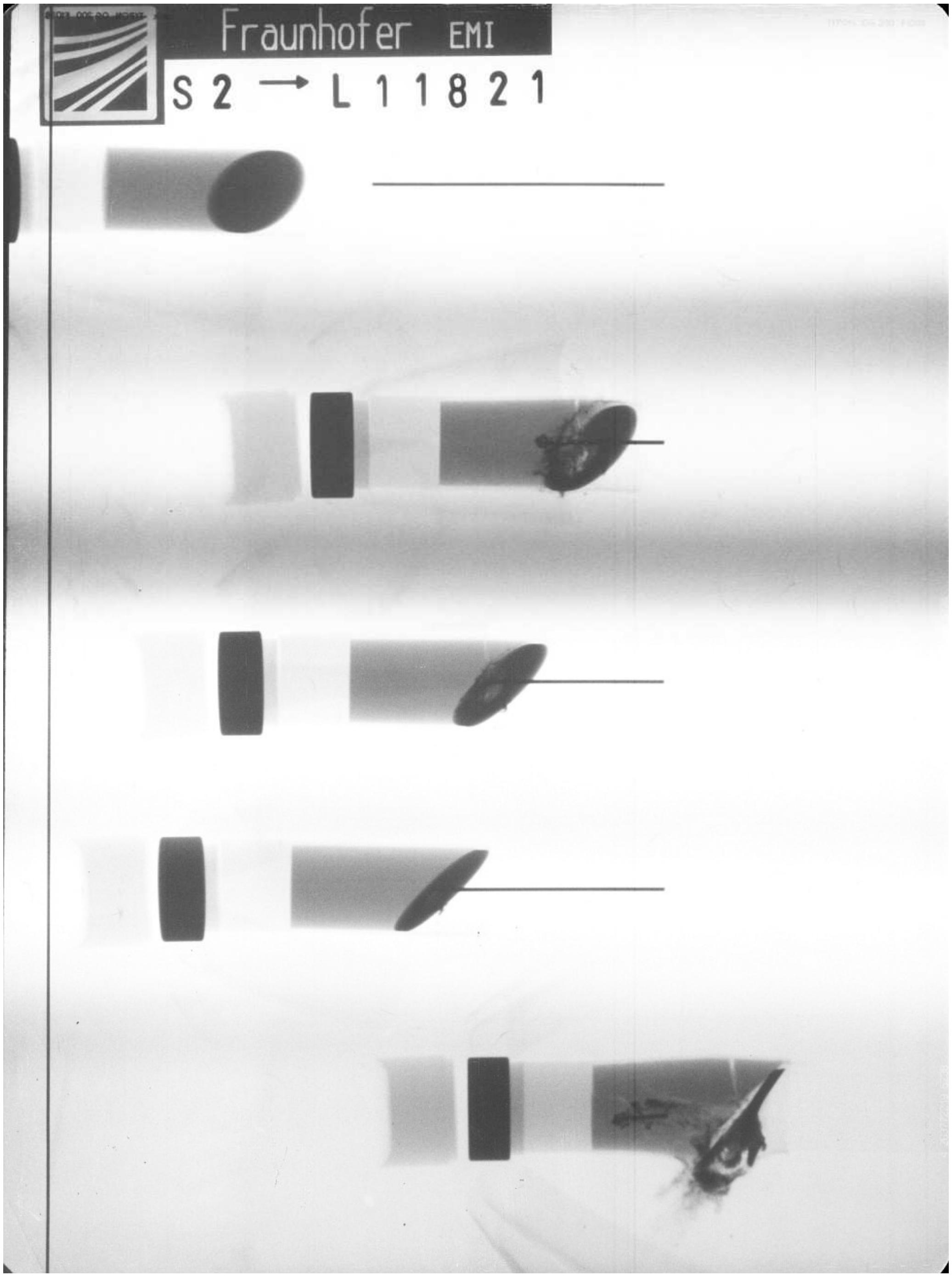

Figure A-23. X-ray picture for Exp. 11821: 45° with buffer, v_p = 1.434 km/s.

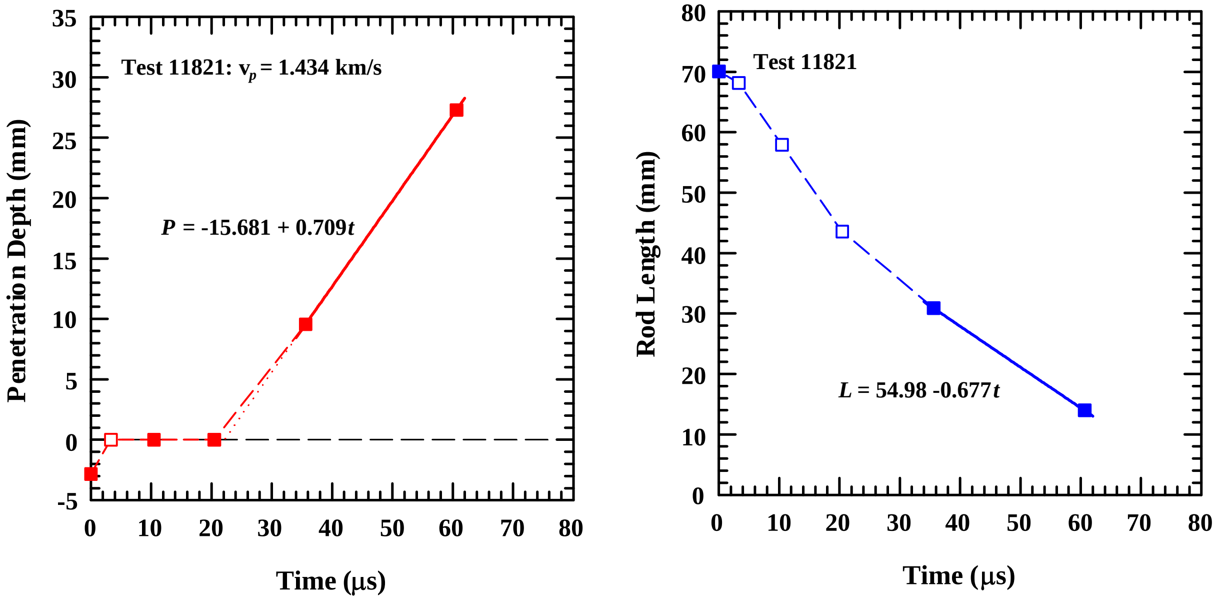

Figure A-24. Position and rod length vs. time for Exp. 11821: 45° with buffer, v_p = 1.434 km/s.

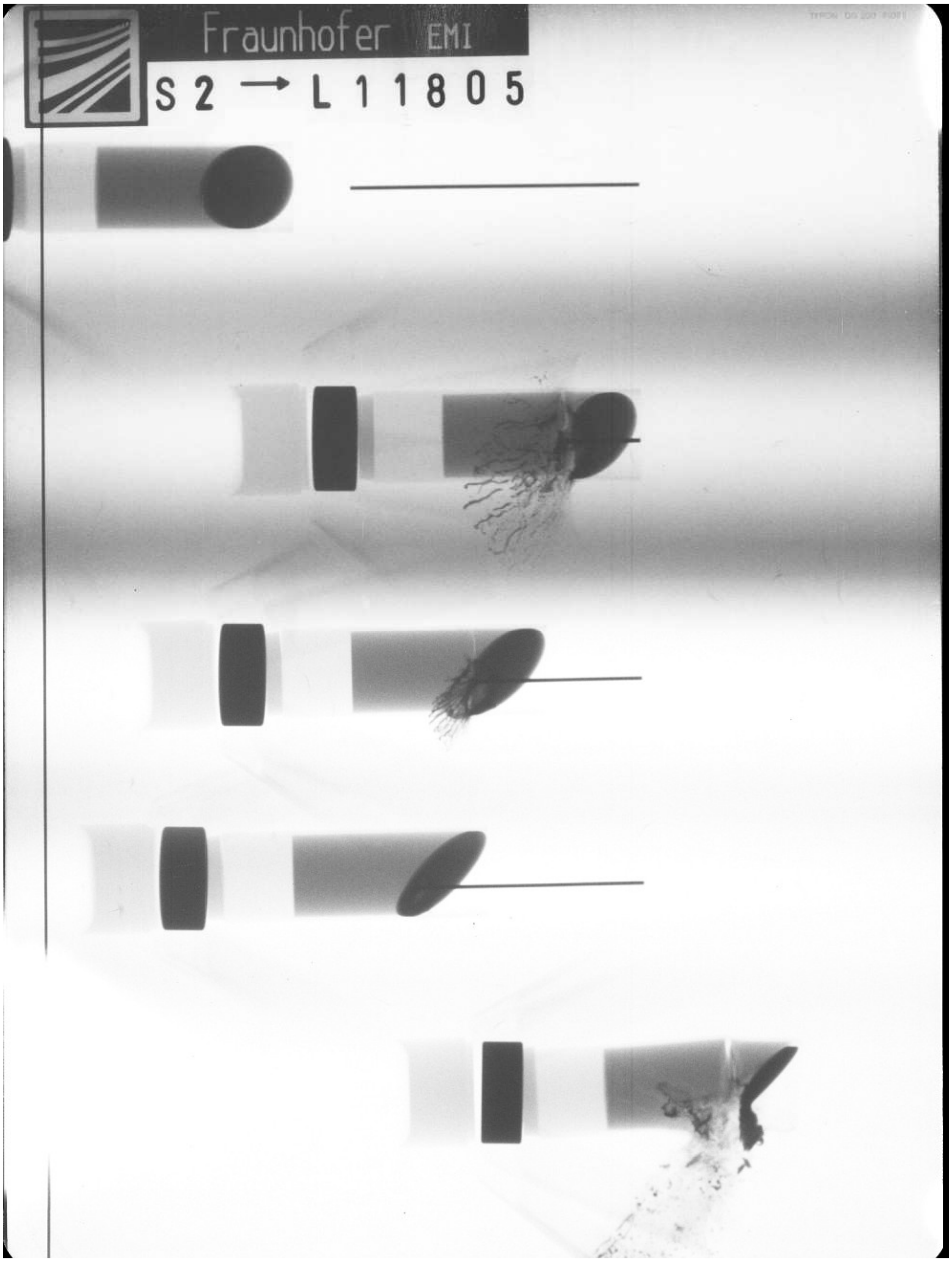

Figure A-25. X-ray picture for Exp. 11805: 45° with buffer, v_p = 1.522 km/s.

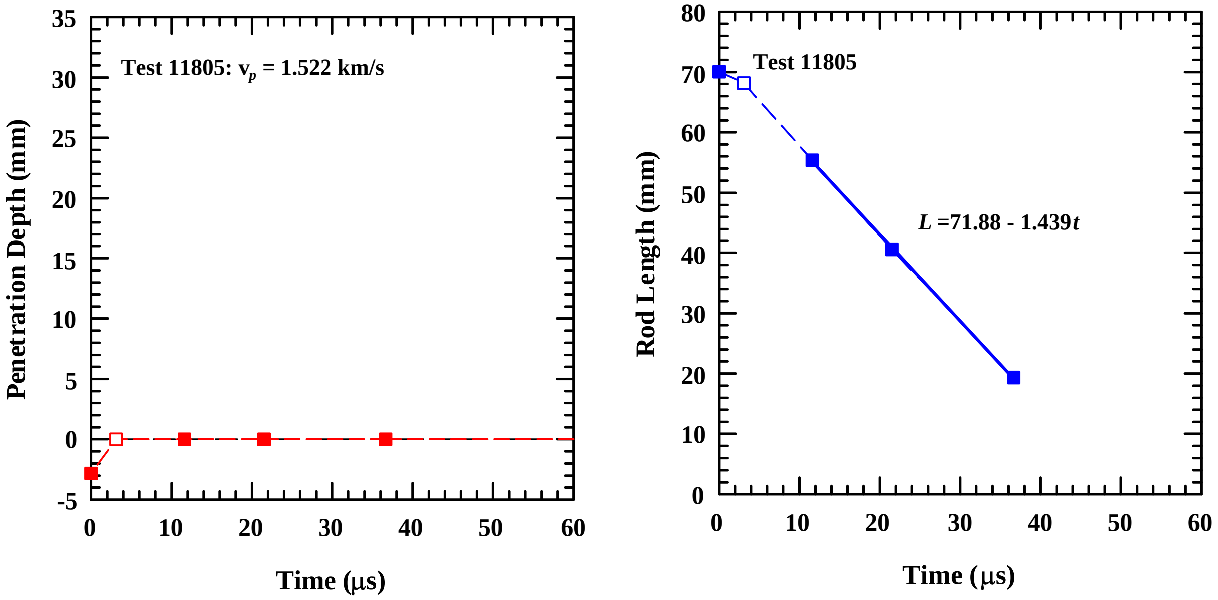

Figure A-26. Position and rod length vs. time for Exp. 11805: 45° with buffer, v_p = 1.522 km/s.

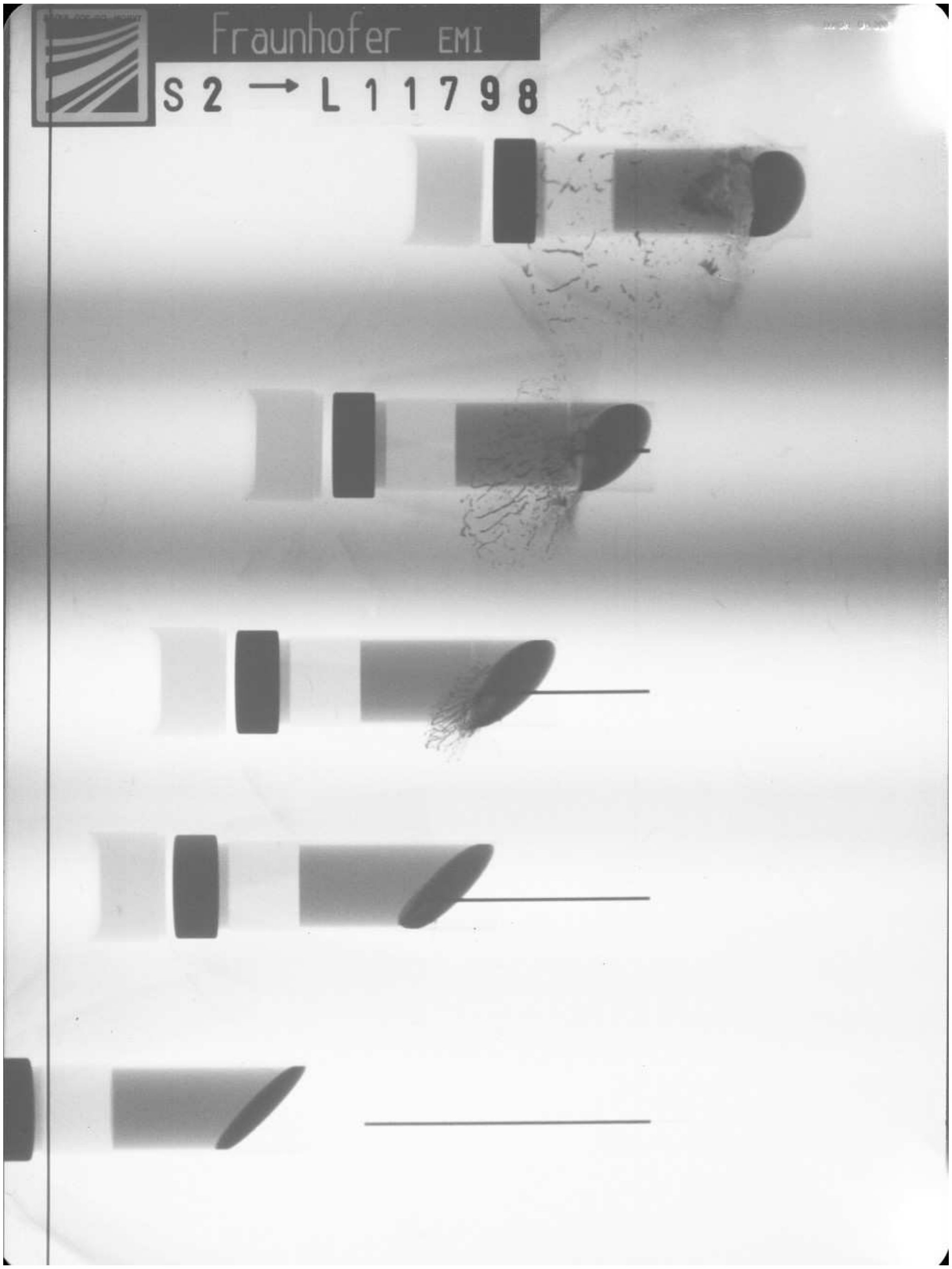

Figure A-27. X-ray picture for Exp. 11798: 45° with buffer, v_p = 1.535 km/s.

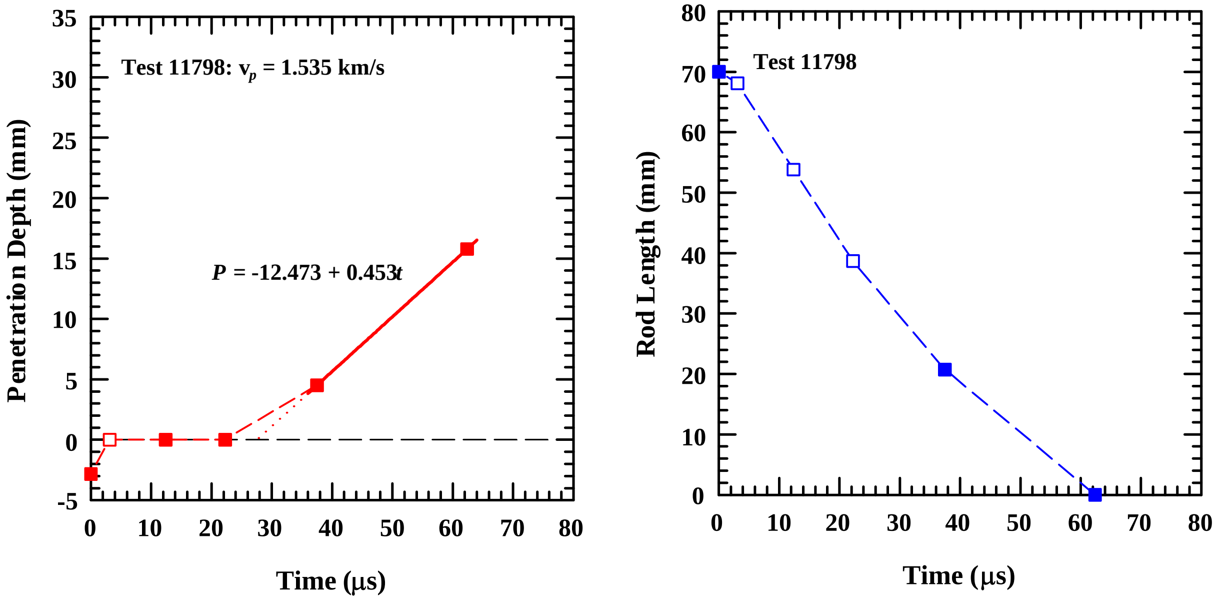

Figure A-28. Position and rod length vs. time for Exp. 11798: 45° with buffer, v_p = 1.535 km/s.

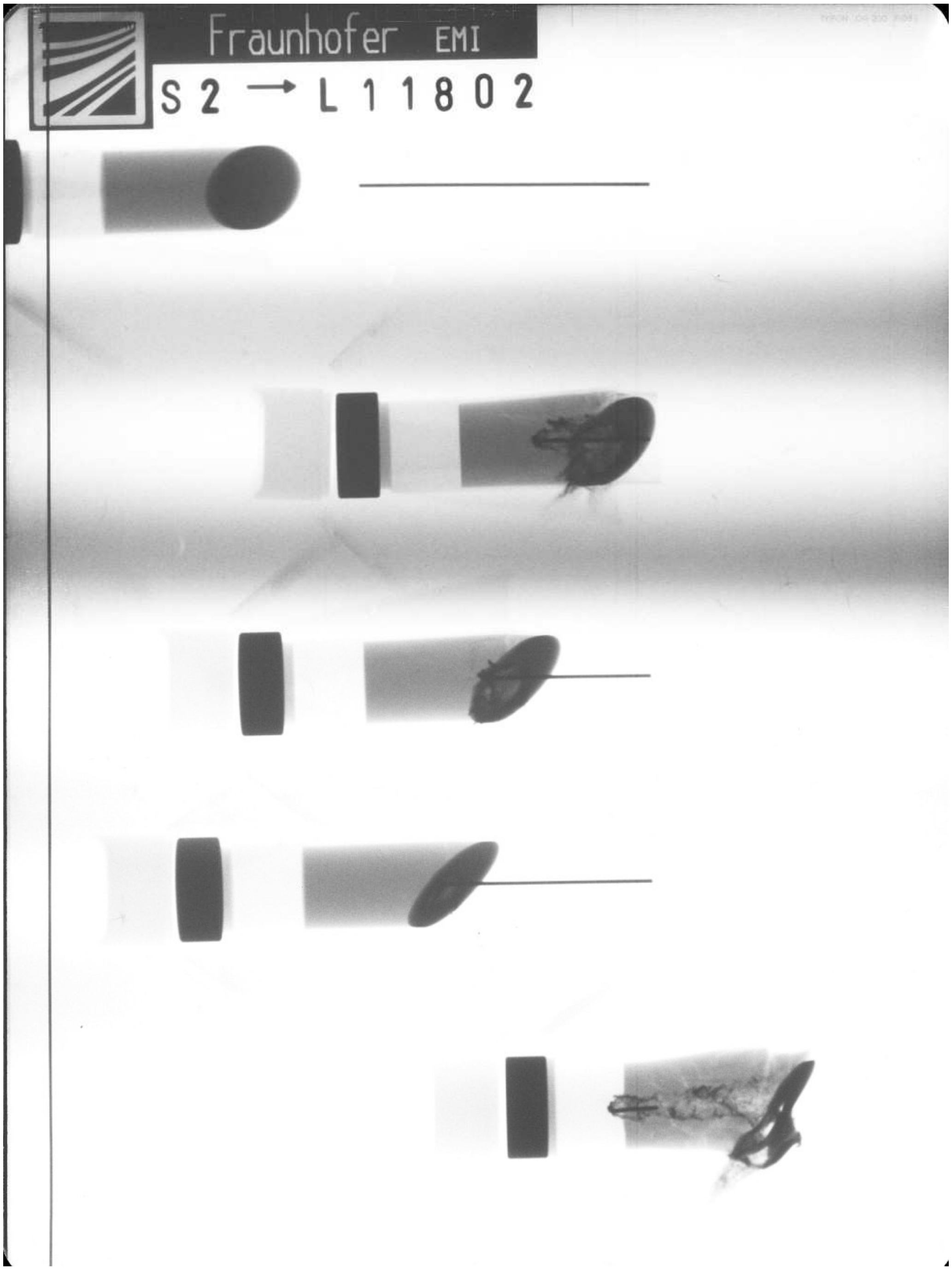

Figure A-29. X-ray picture for Exp. 11802: 45° with buffer, v_p = 1.545 km/s.

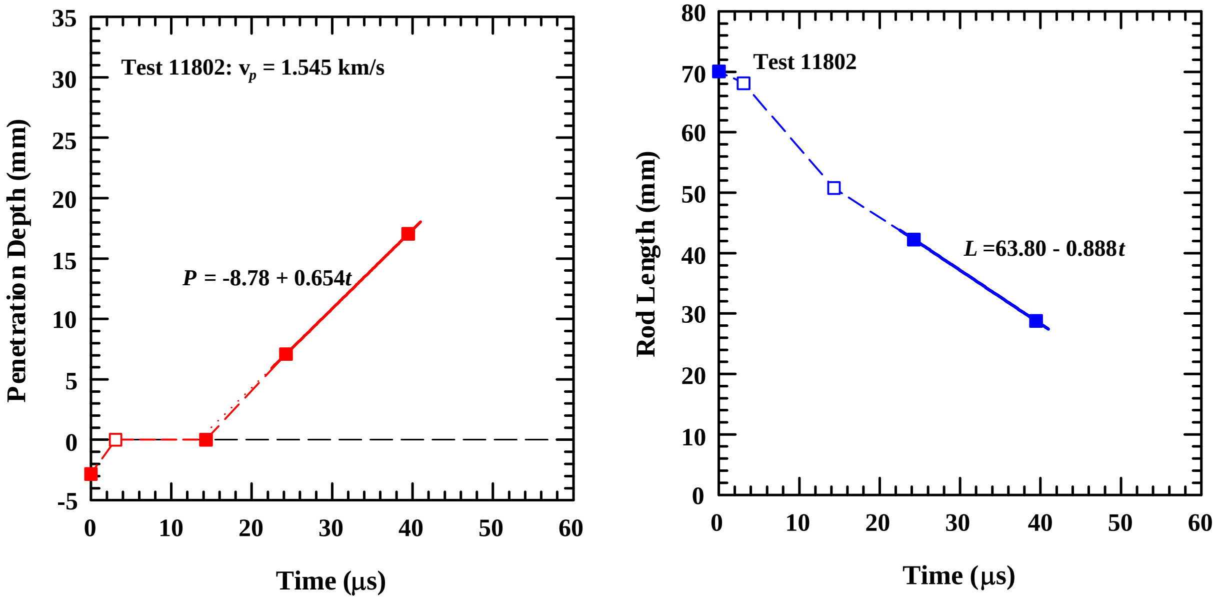

Figure A-30. Position and rod length vs. time for Exp. 11802: 45° with buffer, v_p = 1.545 km/s.

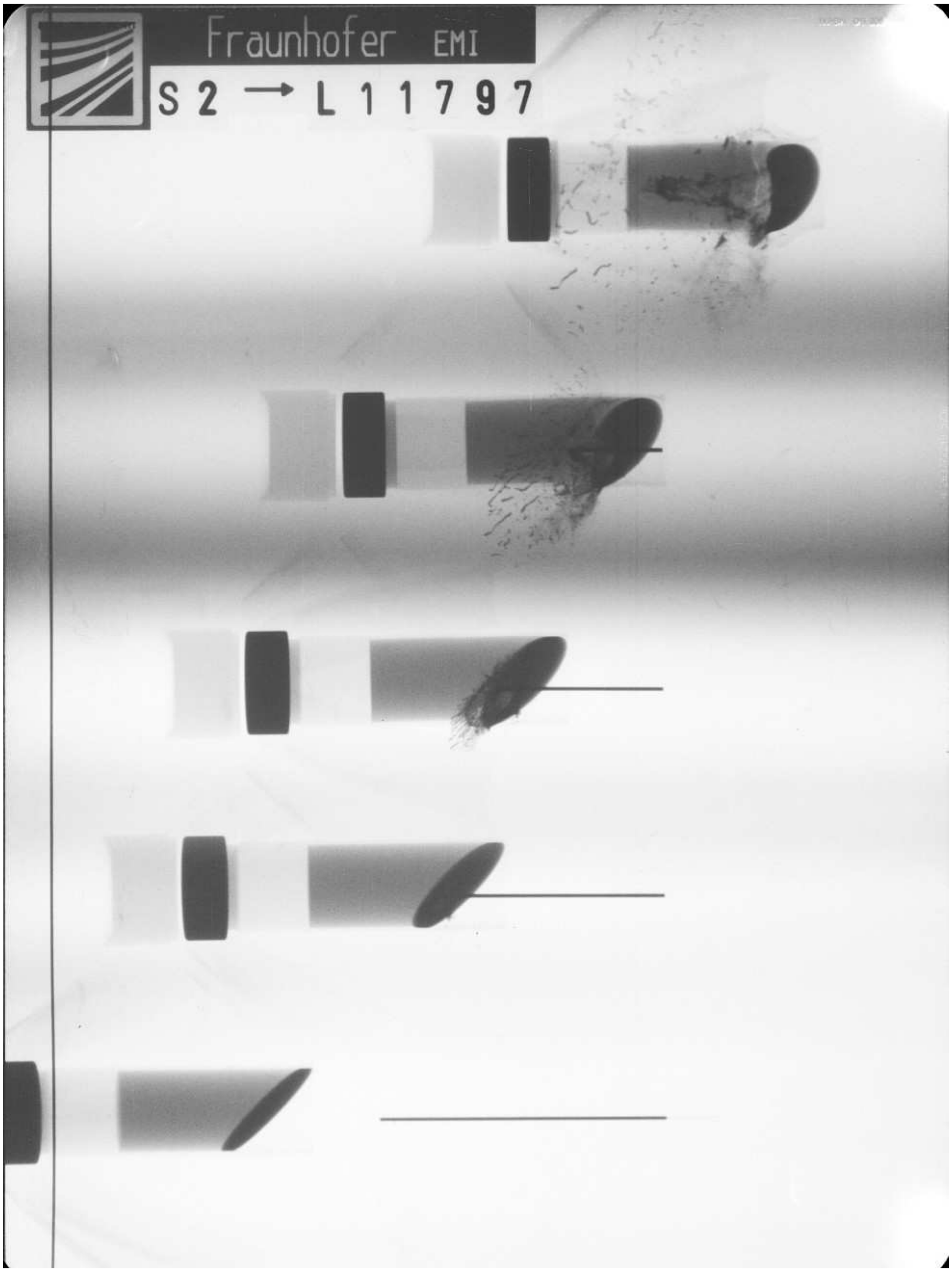

Figure A-31. X-ray picture for Exp. 11797: 45° with buffer, v_p = 1.568 km/s.

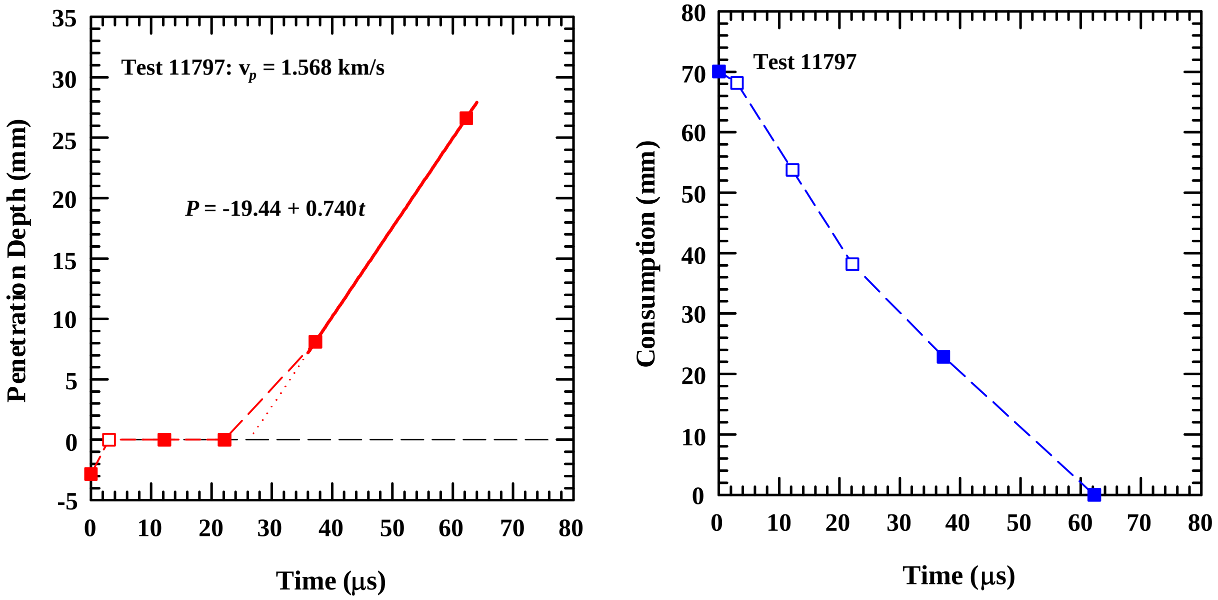

Figure A-32. Position and rod length vs. time for Exp. 11797: 45° with buffer, v_p = 1.568 km/s.

Figure A-33. X-ray picture for Exp. 11818: 45° with buffer, v_P = 1.593 km/s.

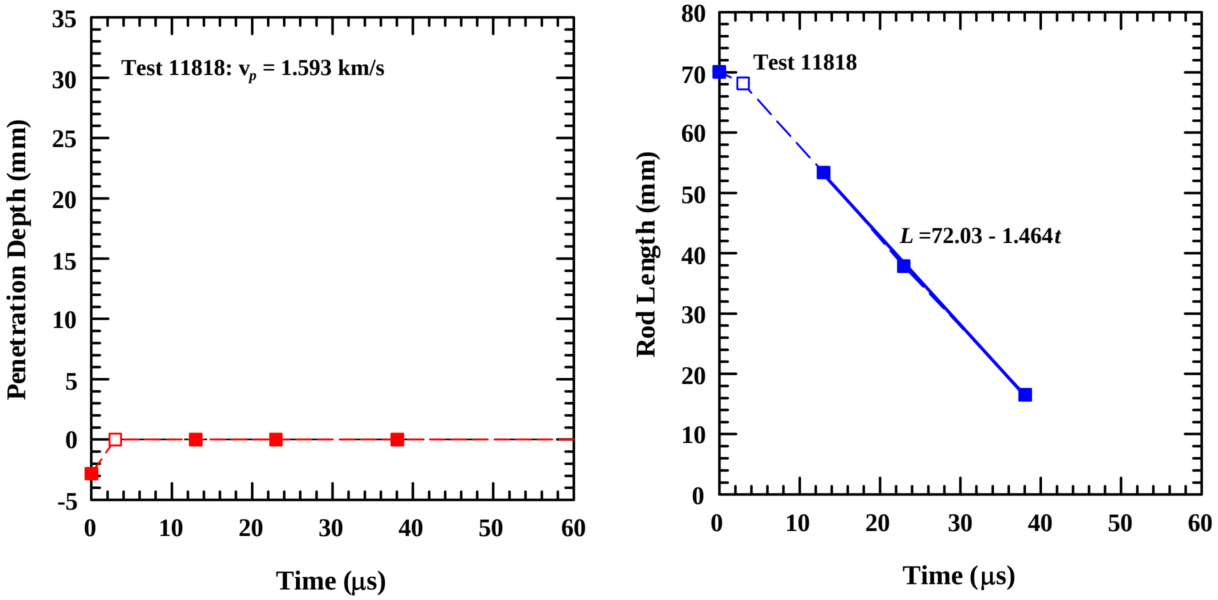

Figure A-34. Position and rod length vs. time for Exp. 11818: 45° with buffer, v_P = 1.593 km/s.

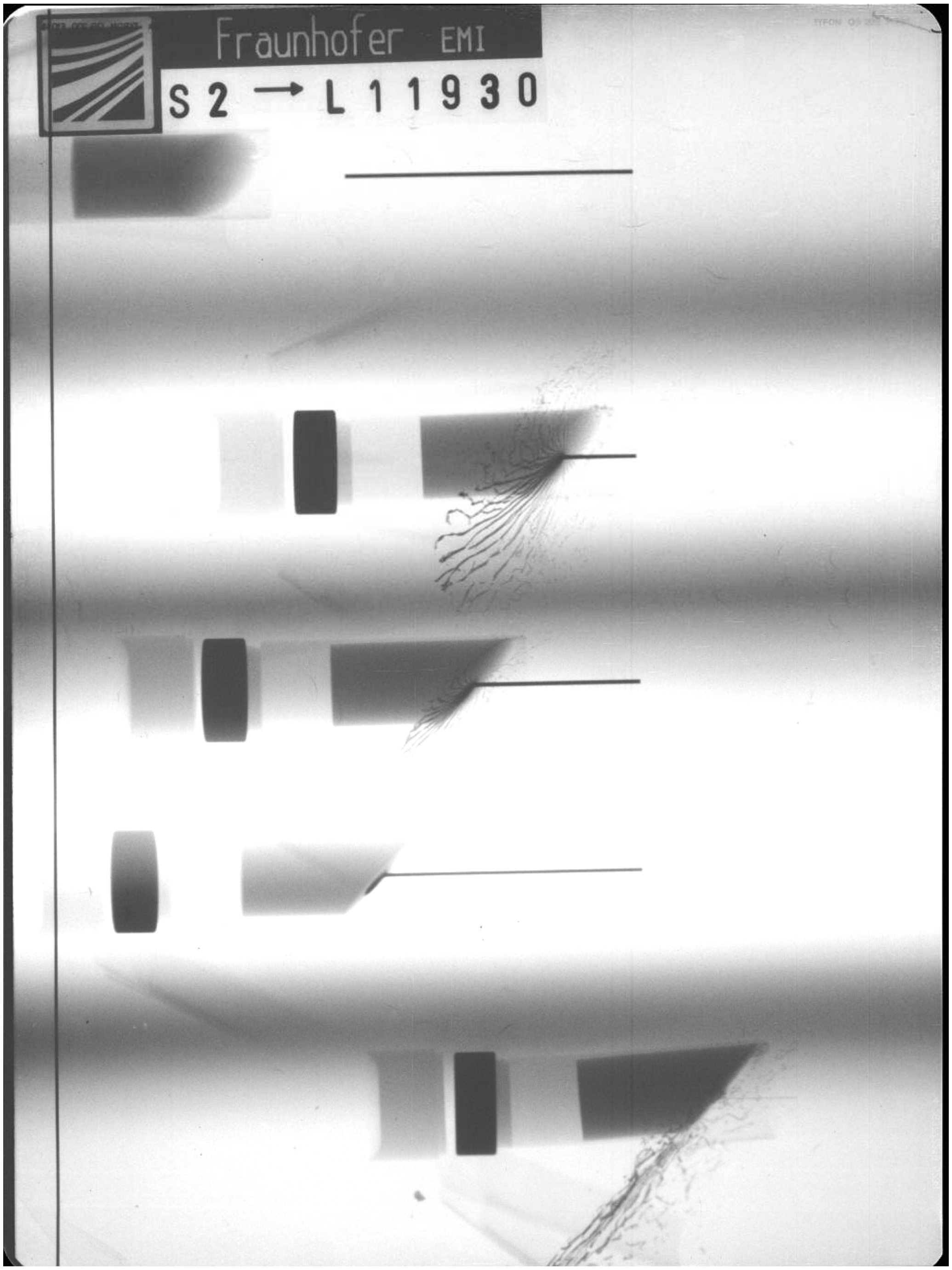

Figure A-35. X-ray picture for Exp. 11930: 45° bare, v_p = 0.928 km/s.

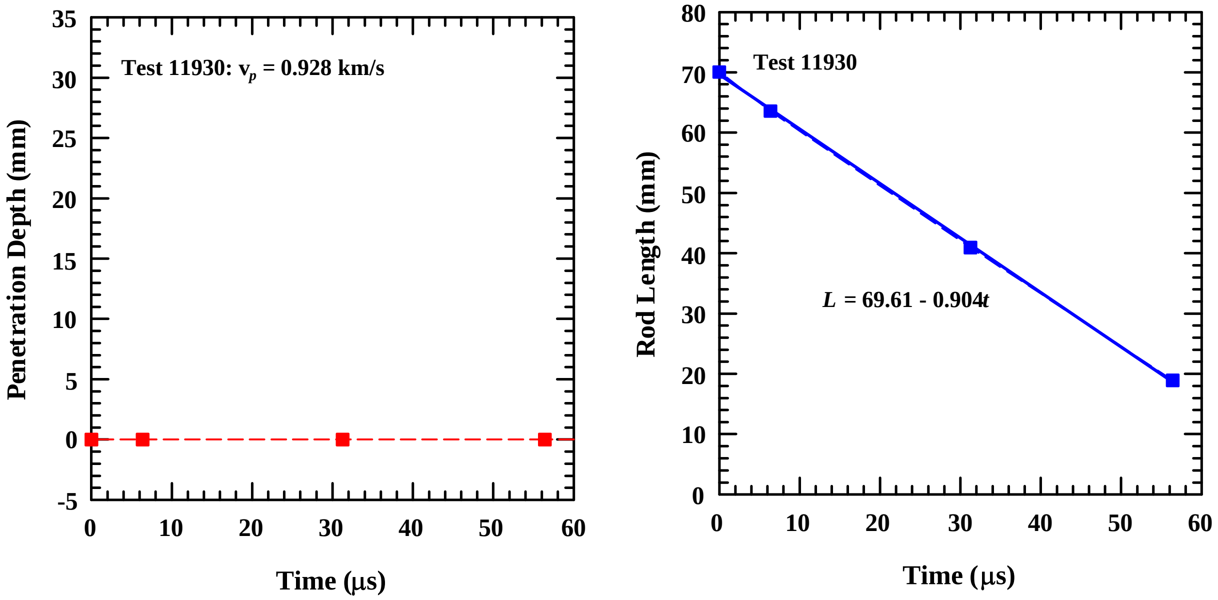

Figure A-36. Position and rod length vs. time for Exp. 11930: 45° bare, v_p = 0.928 km/s.

Figure A-37. X-ray picture for Exp. 11928: 45° bare, $v_P = 1.015$ km/s.

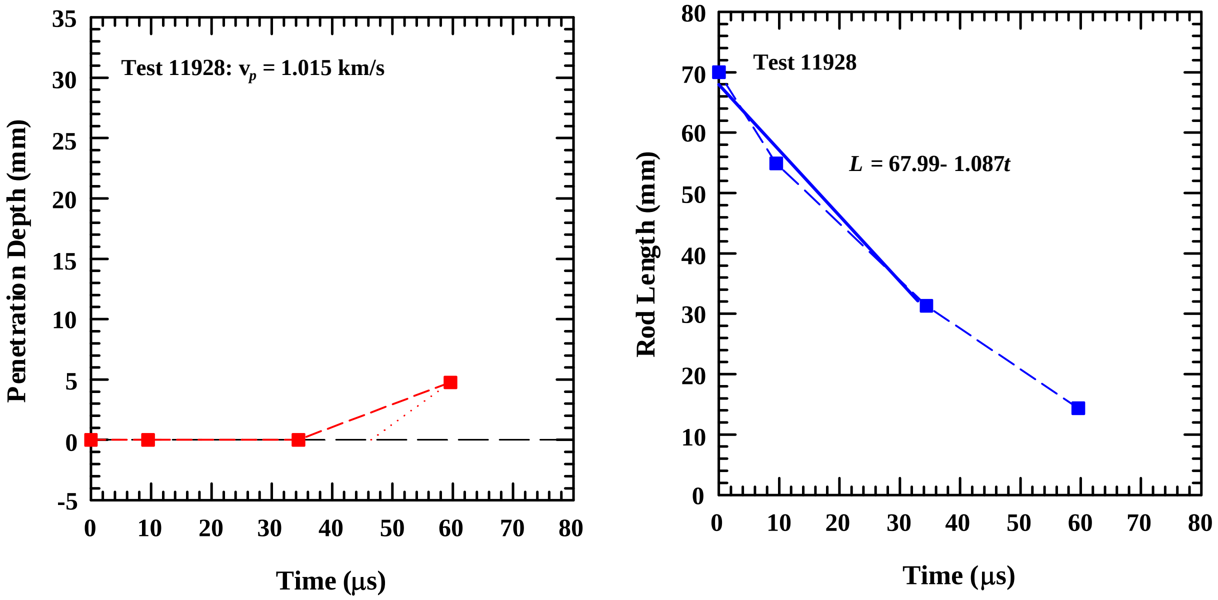

Figure A-38. Position and rod length vs. time for Exp. 11928: 45° bare, v_P = 1.015 km/s.

Figure A-39. X-ray picture for Exp. 11933: 45° bare, v_p = 1.024 km/s.

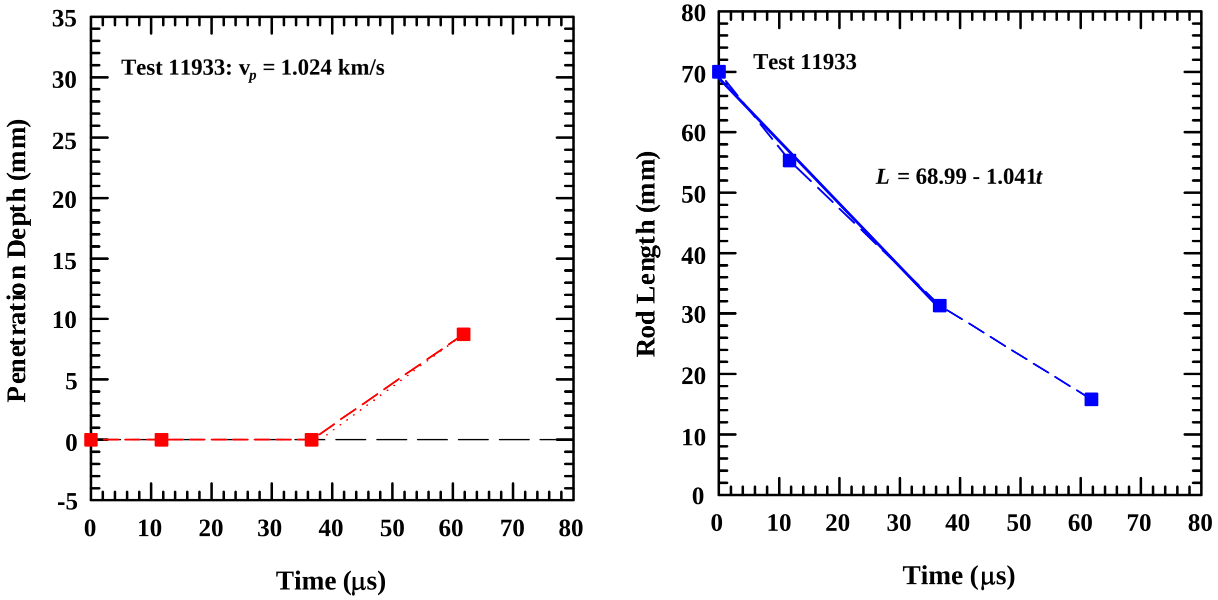

Figure A-40. Position and rod length vs. time for Exp. 11933: 45° bare, v_p = 1.024 km/s.

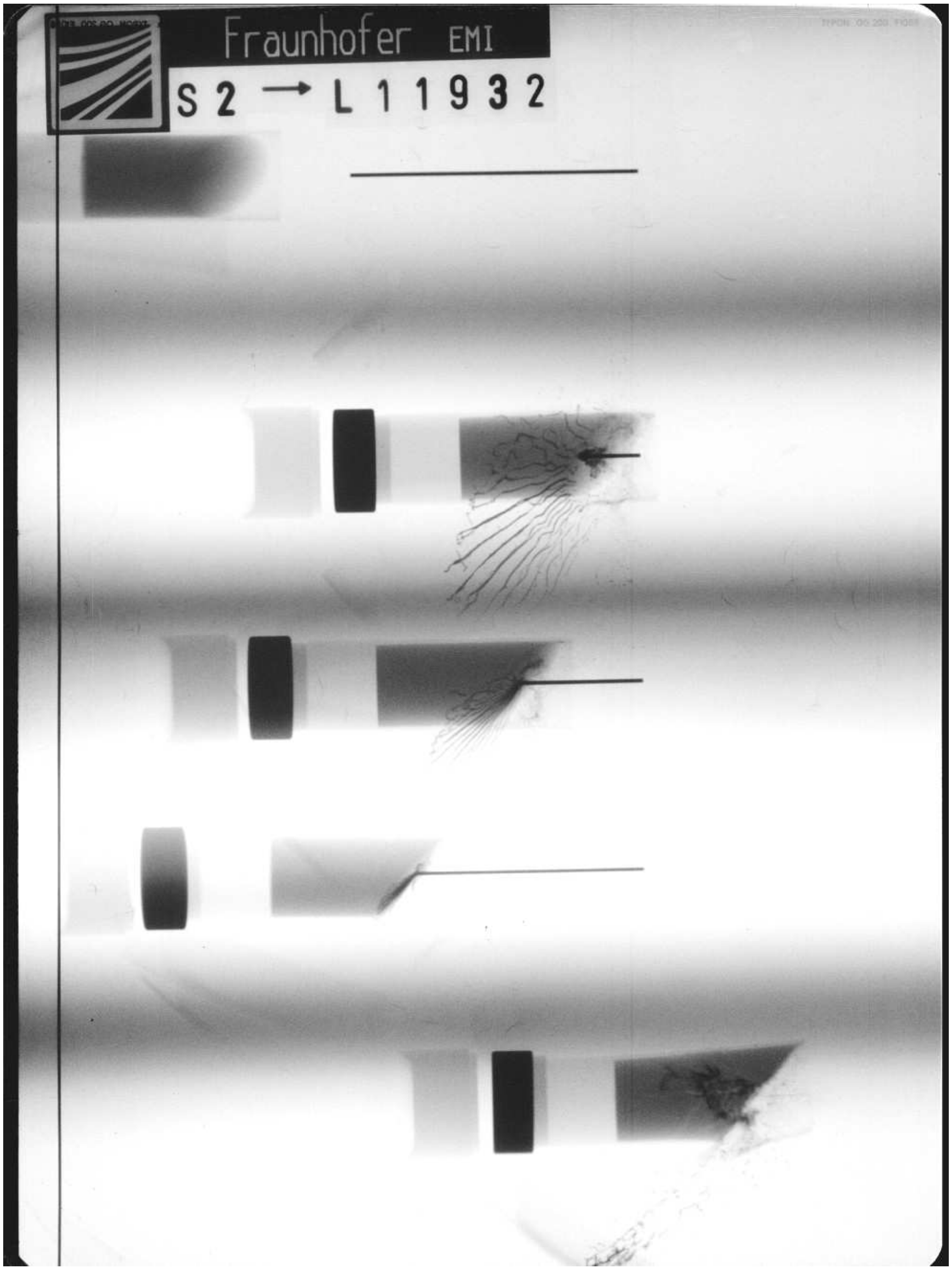

Figure A-41. X-ray picture for Exp. 11932: 45° bare, v_p = 1.070 km/s.

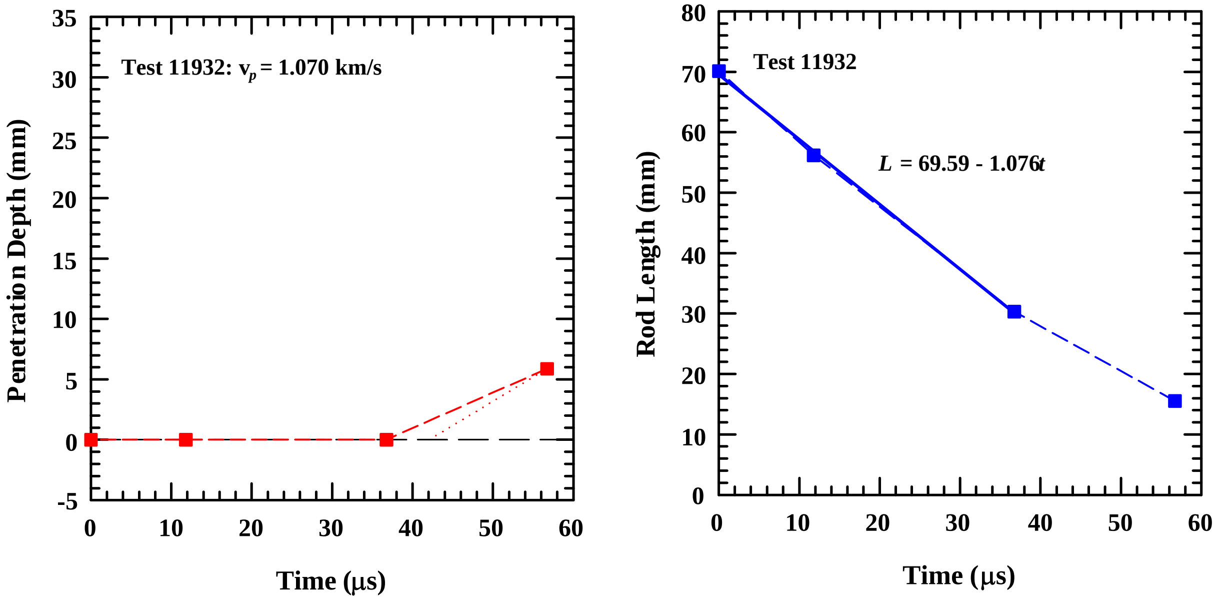

Figure A-42. Position and rod length vs. time for Exp. 11932: 45° bare, v_p = 1.070 km/s.

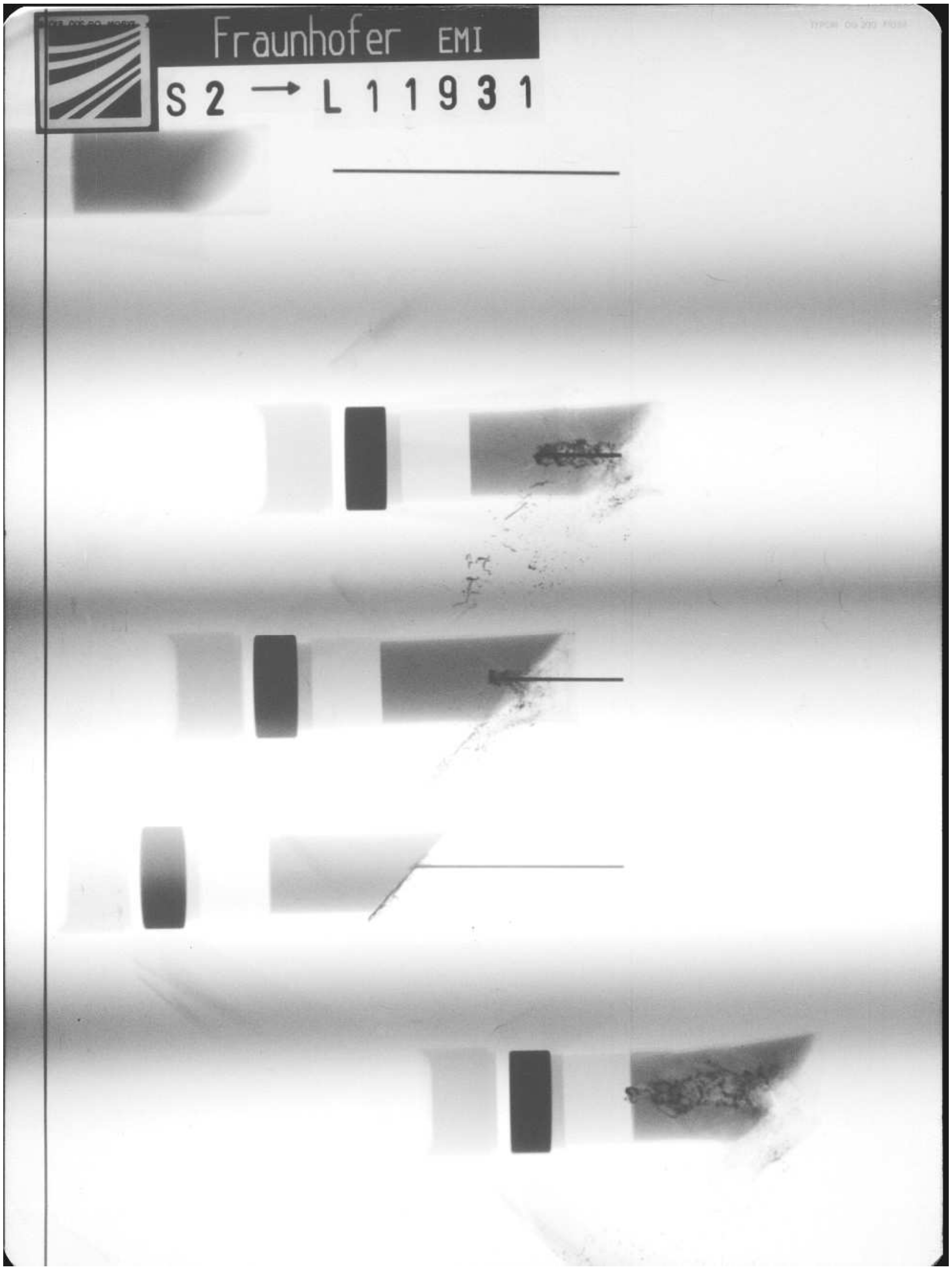

Figure A-43. X-ray picture for Exp. 11931: 45° bare, v_p = 1.128 km/s.

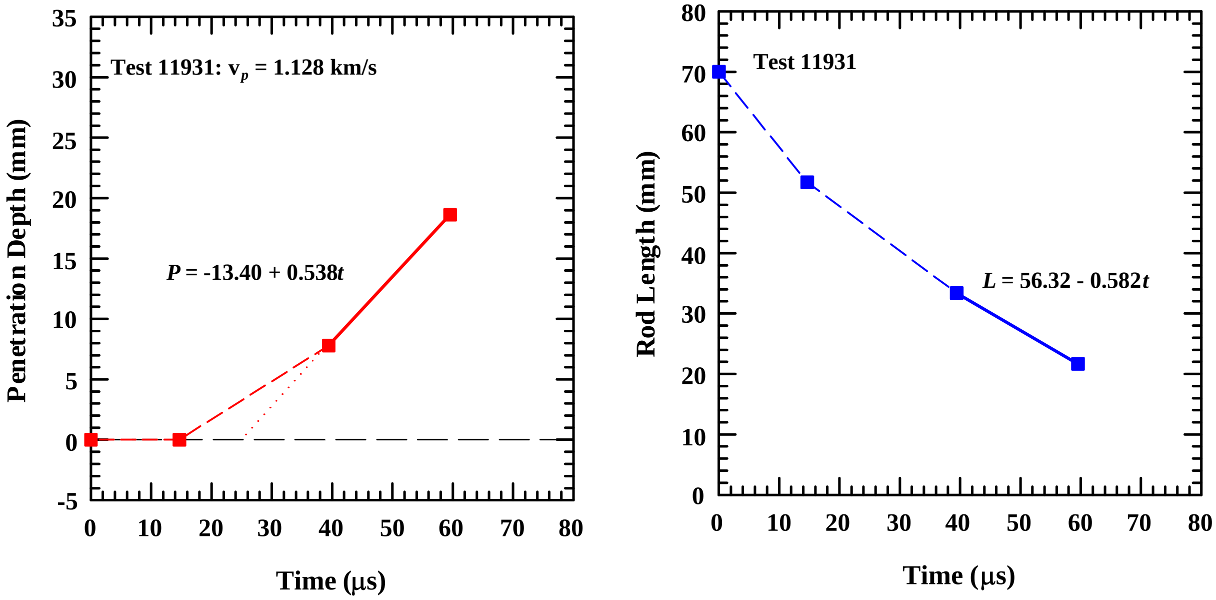

Figure A-44. Position and rod length vs. time for Exp. 11931: 45° bare, v_p = 1.128 km/s.

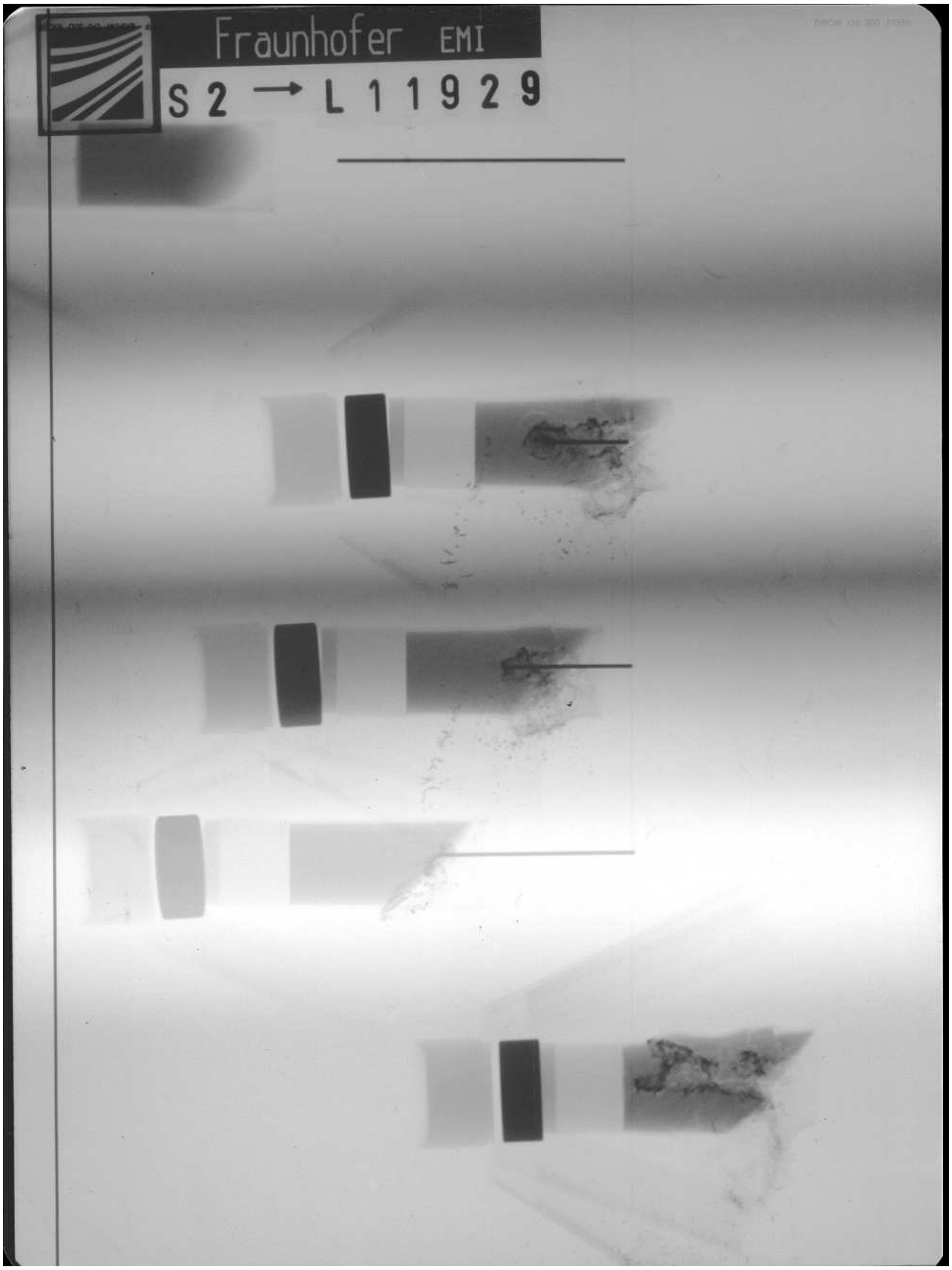

Figure A-45. X-ray picture for Exp. 11929: 45° bare, v_p = 1.191 km/s.

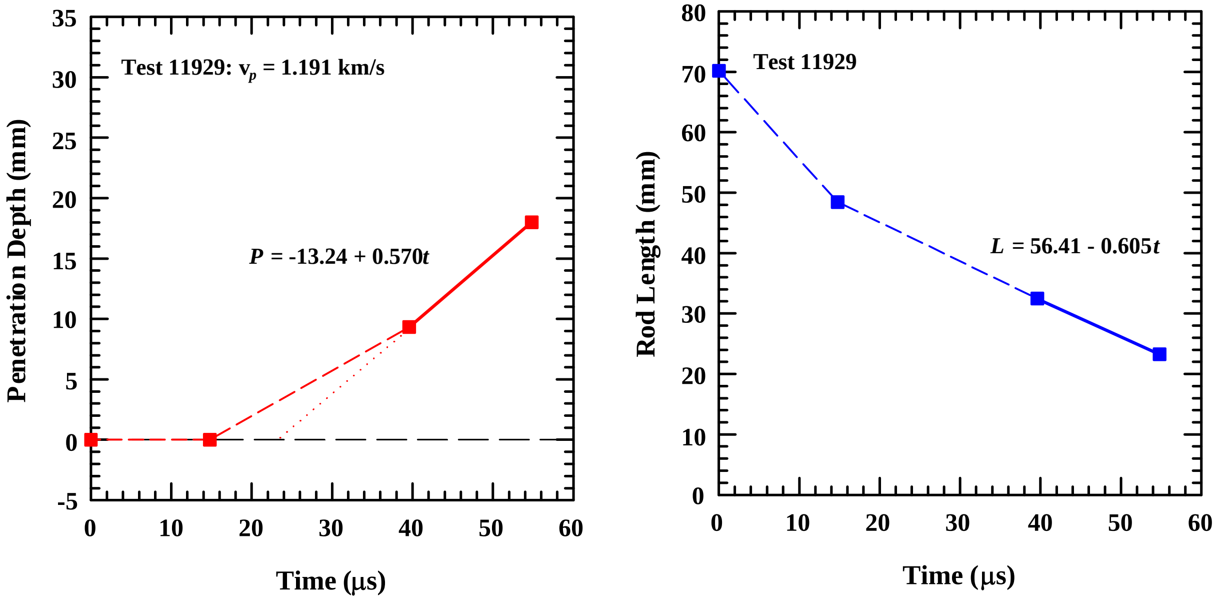

Figure A-46. Position and rod length vs. time for Exp. 11929: 45° bare, v_p = 1.191 km/s.

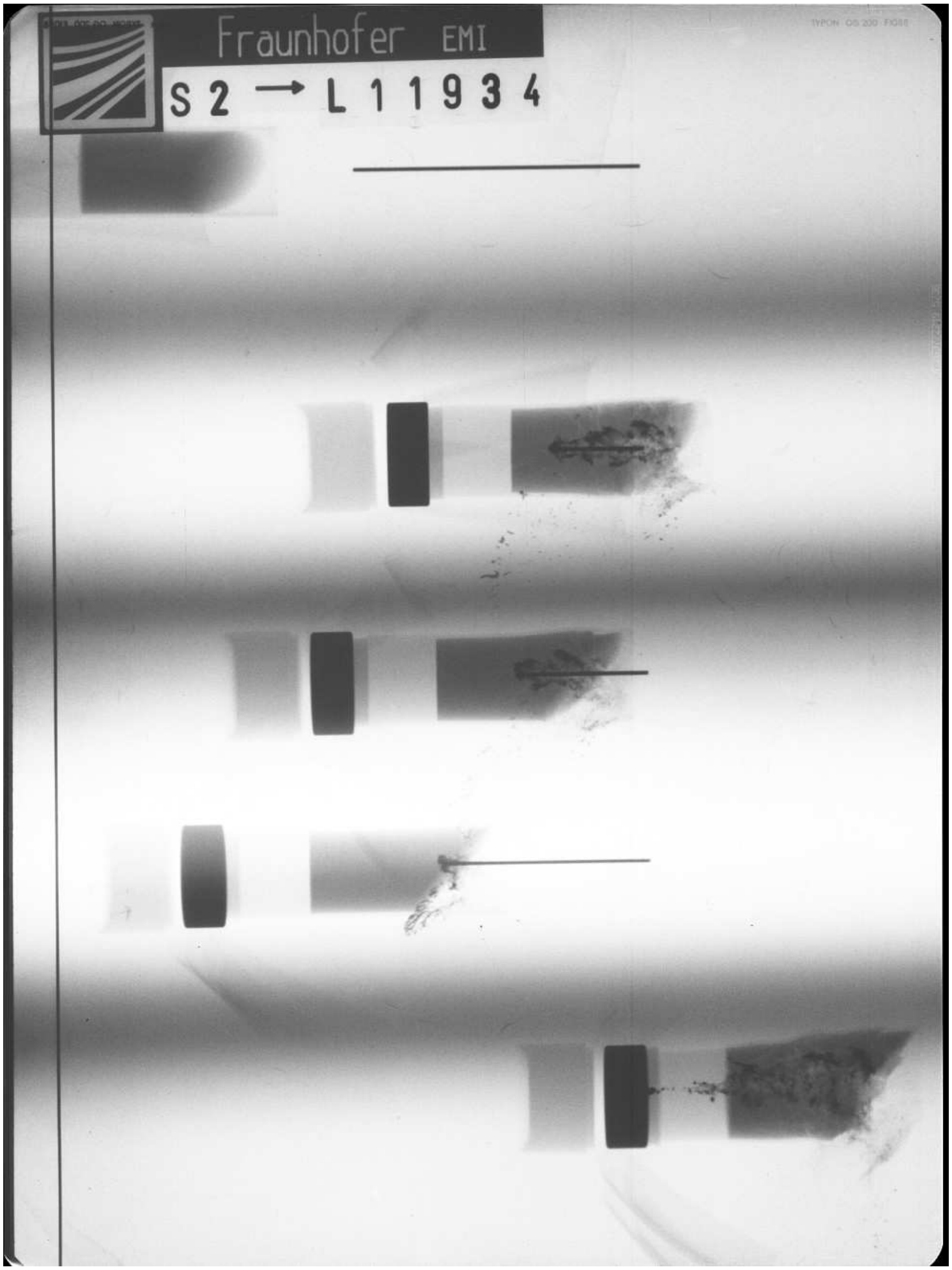

Figure A-47. X-ray picture for Exp. 11934: 45° bare, v_p = 1.292 km/s.

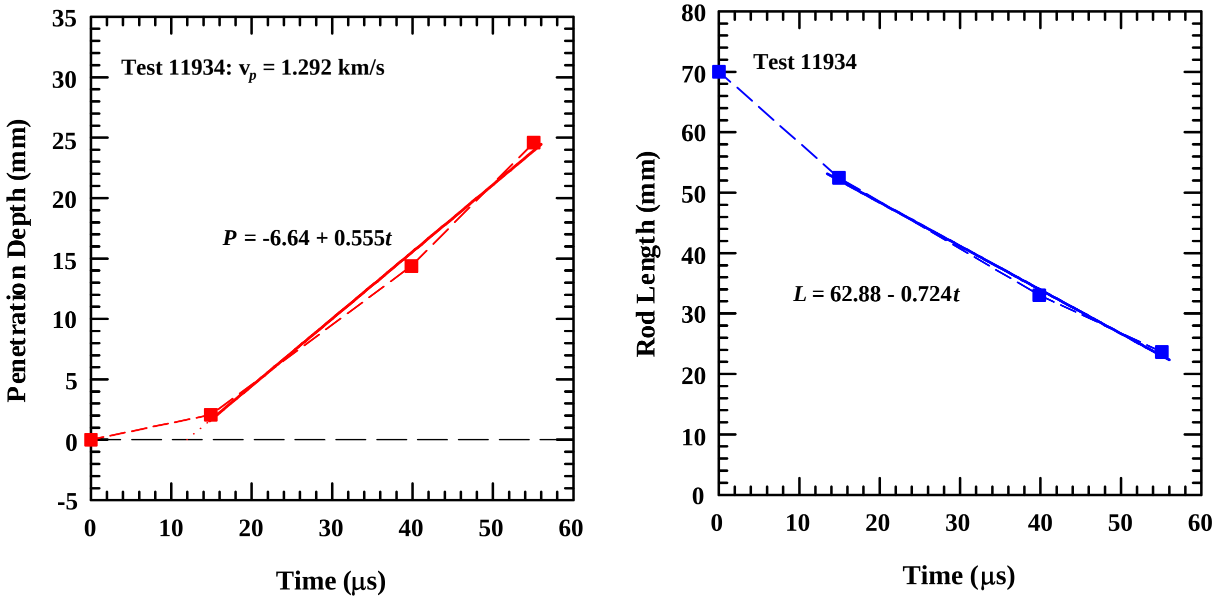

Figure A-48. Position and rod length vs. time for Exp. 11934: 45° bare, v_p = 1.292 km/s.

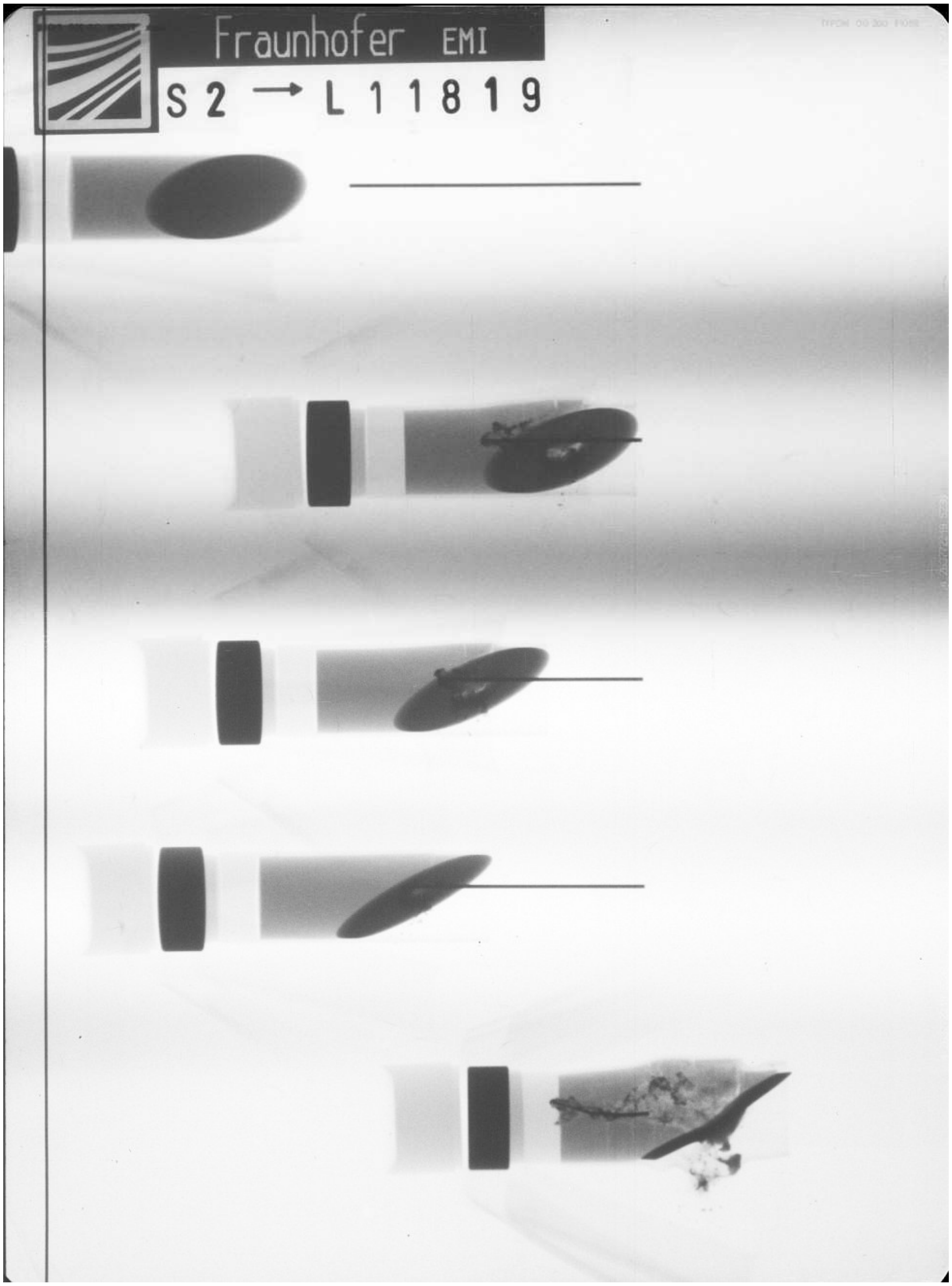

Figure A-49. X-ray picture for Exp. 11819: 60° with buffer, v_p = 1.430 km/s.

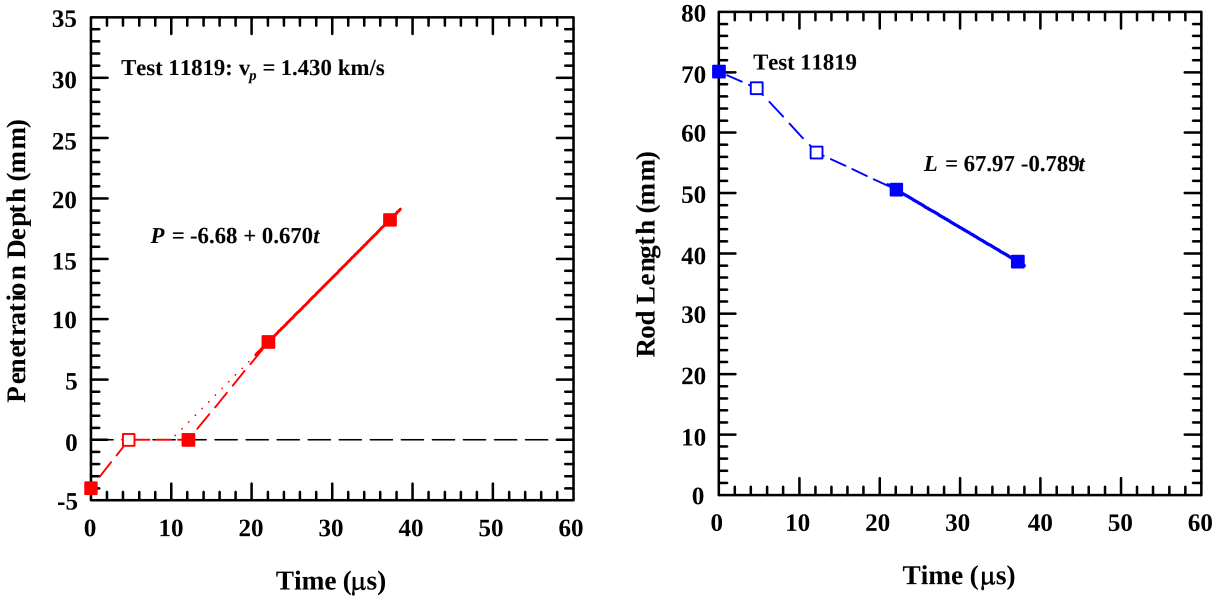

Figure A-50. Position and rod length vs. time for Exp. 11819: 60° with buffer, v_p = 1.430 km/s.

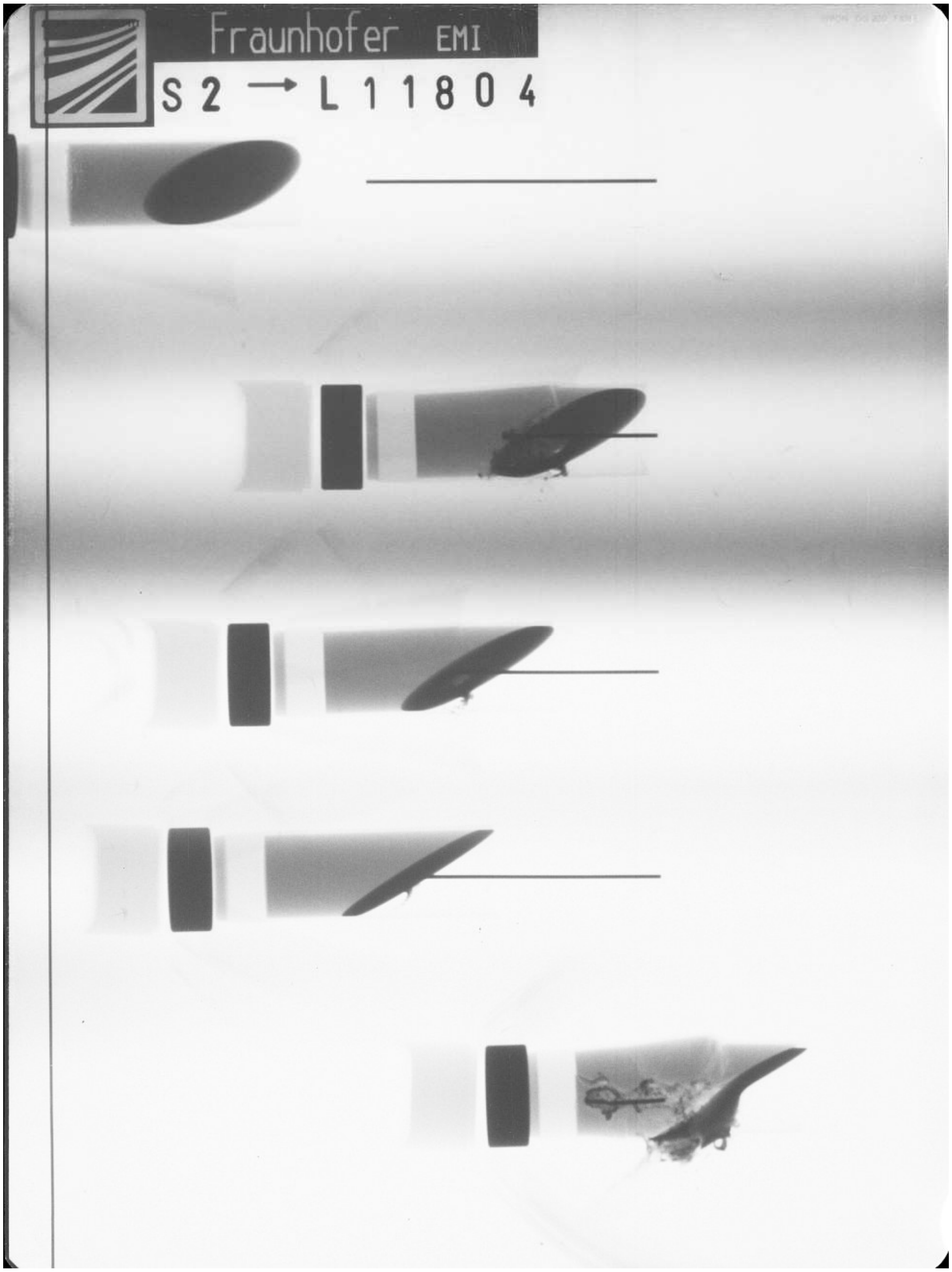

Figure A-51. X-ray picture for Exp. 11804: 60° with buffer, $v_p = 1.497$ km/s.

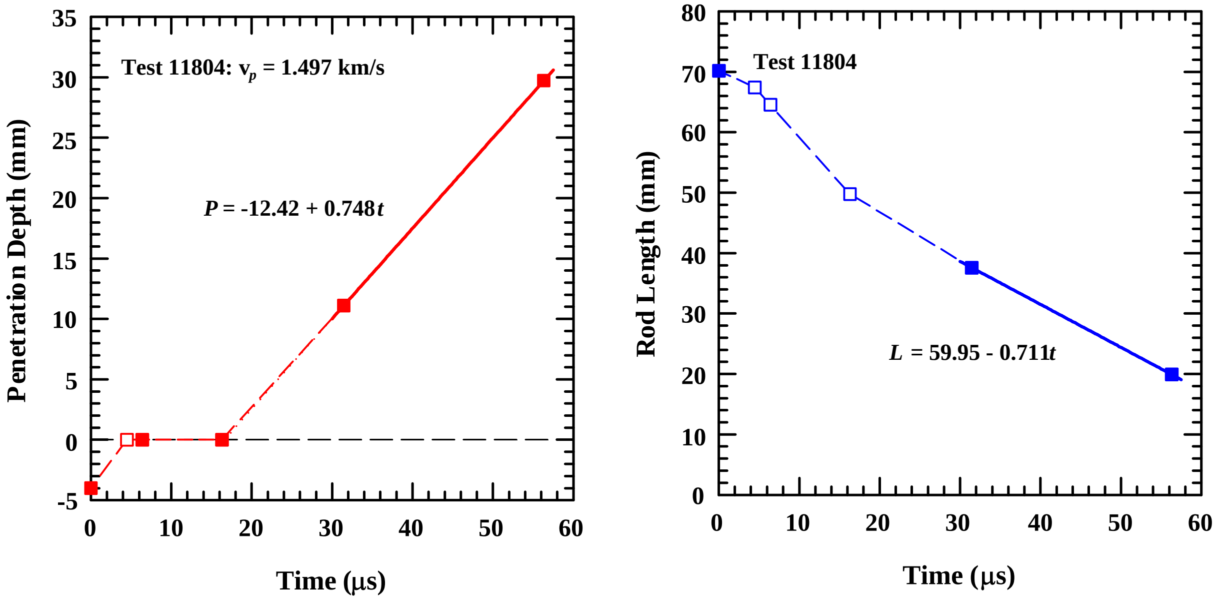

Figure A-52. Position and rod length vs. time for Exp. 11804: 60° with buffer, v_p = 1.497 km/s.

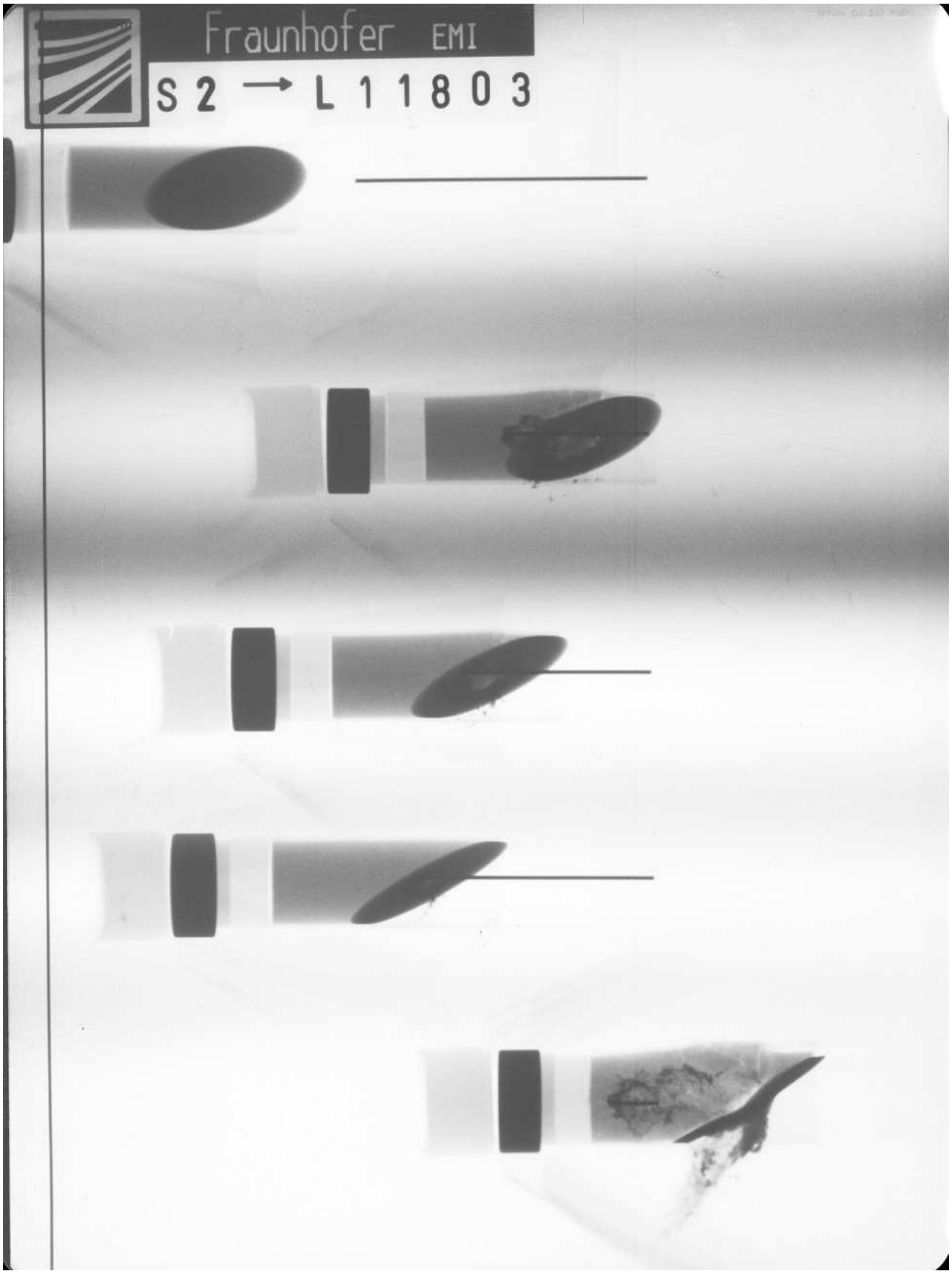

Figure A-53. X-ray picture for Exp. 11803: 60° with buffer, v_p = 1.522 km/s.

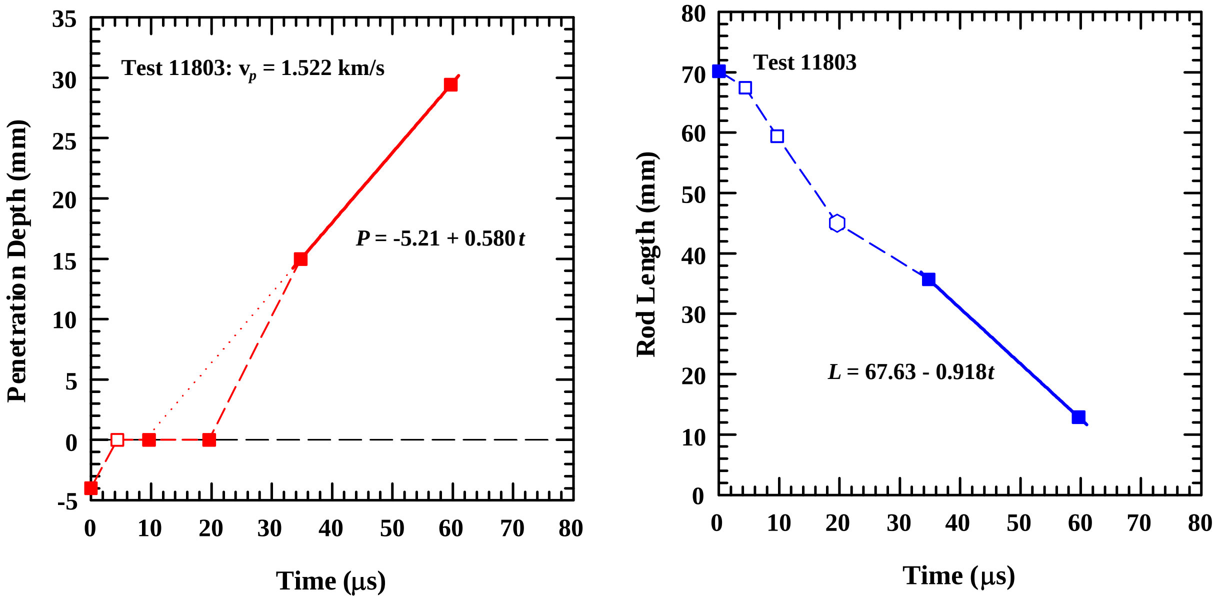

Figure A-54. Position and rod length vs. time for Exp. 11803: 60° with buffer, v_p = 1.522 km/s.

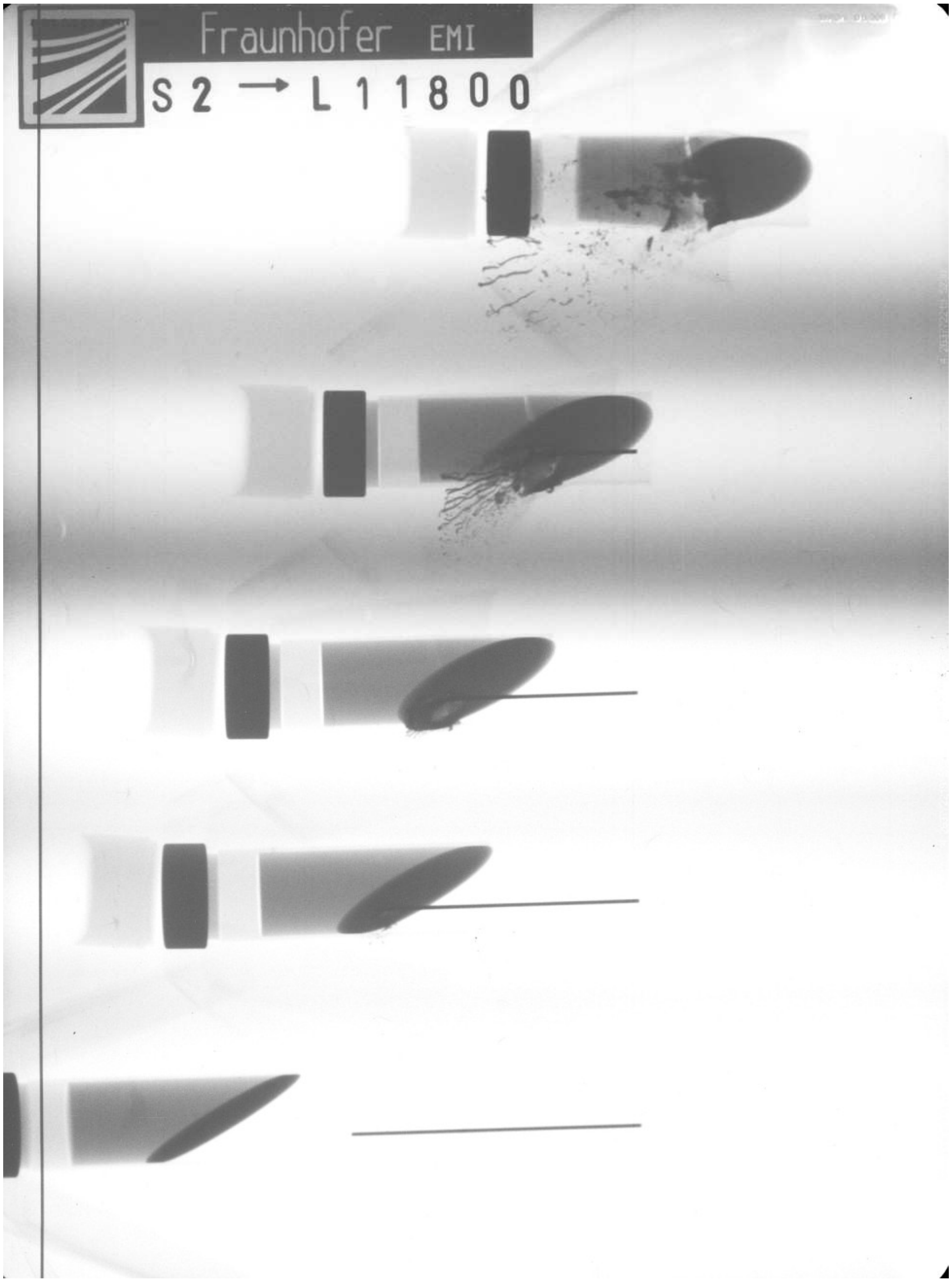

Figure A-55. X-ray picture for Exp. 11800: 60° with buffer, v_p = 1.537 km/s.

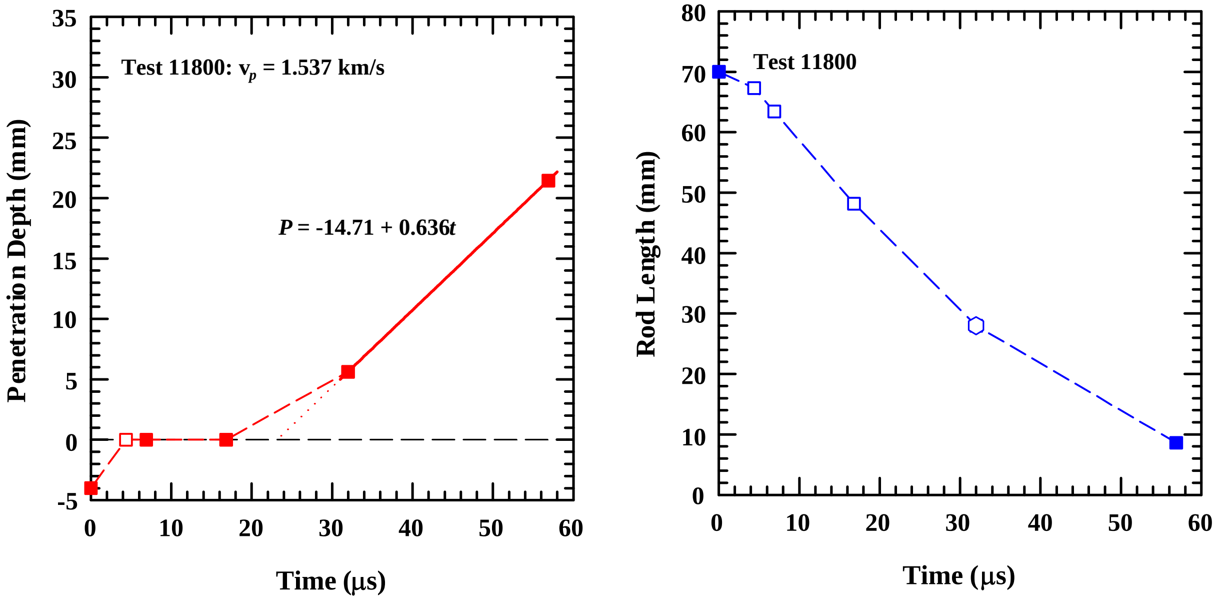

Figure A-56. Position and rod length vs. time for Exp. 11800: 60° with buffer, v_p = 1.537 km/s.

Figure A-57. X-ray picture for Exp. 11801: 60° with buffer, v_P = 1.548 km/s.

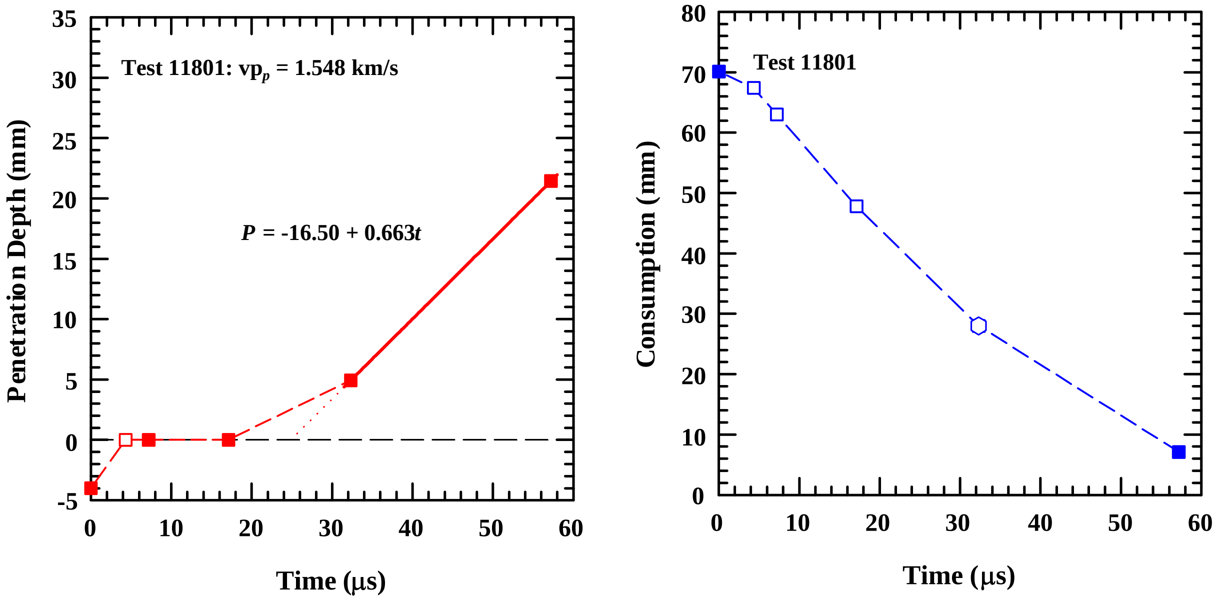

Figure A-58. Position and rod length vs. time for Exp. 11801: 60° with buffer, v_P = 1.548 km/s.

Figure A-59. X-ray picture for Exp. 11799: 60° with buffer, v_p = 1.570 km/s.

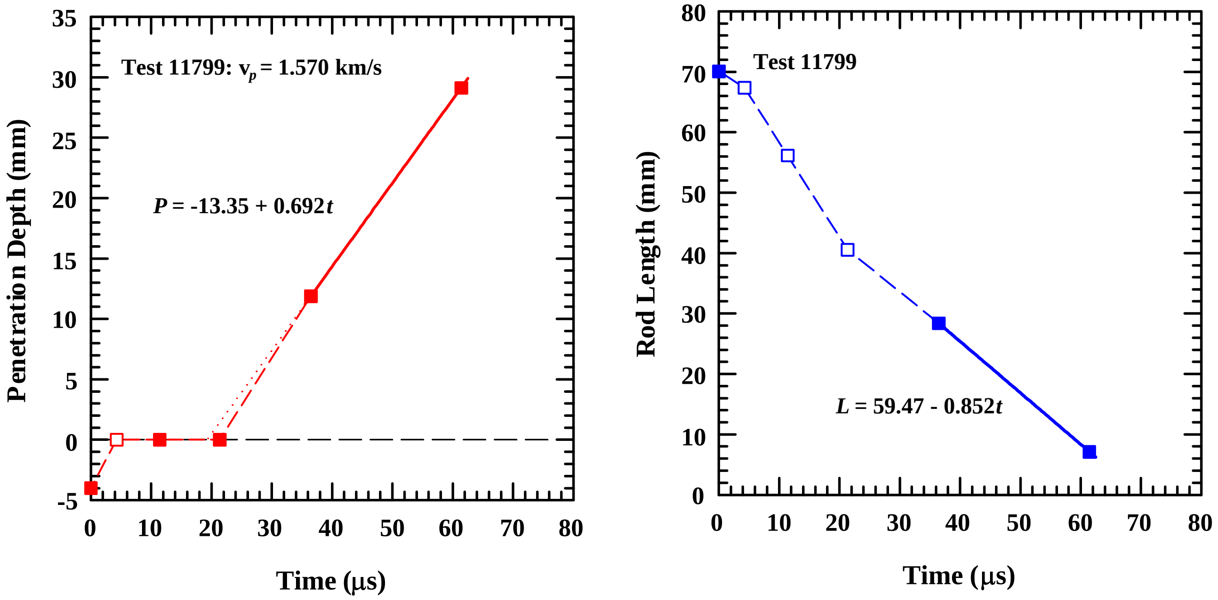

Figure A-60. Position and rod length vs. time for Exp. 11799: 60° with buffer, v_p = 1.570 km/s.

Figure A-61. X-ray picture for Exp. 11817: 60° with buffer, v_p = 1.569 km/s.

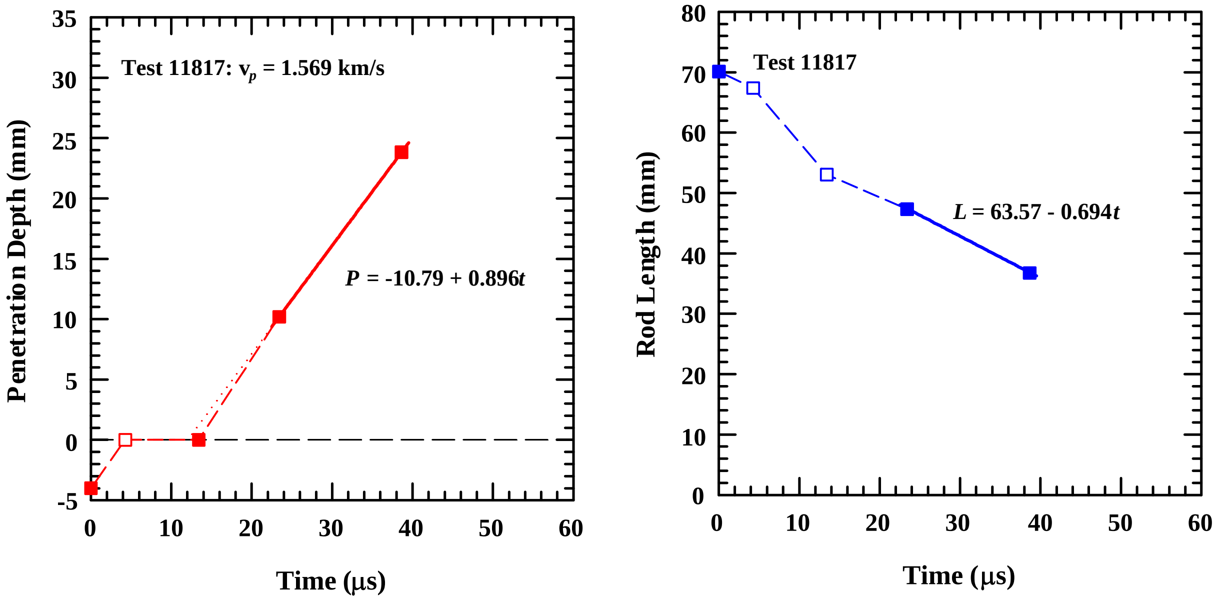

Figure A-62. Position and rod length vs. time for Exp. 11817: 60° with buffer, v_p = 1.569 km/s.

Figure A-63. X-ray picture for Exp. 11820: 60° with buffer, v_p = 1.613 km/s.

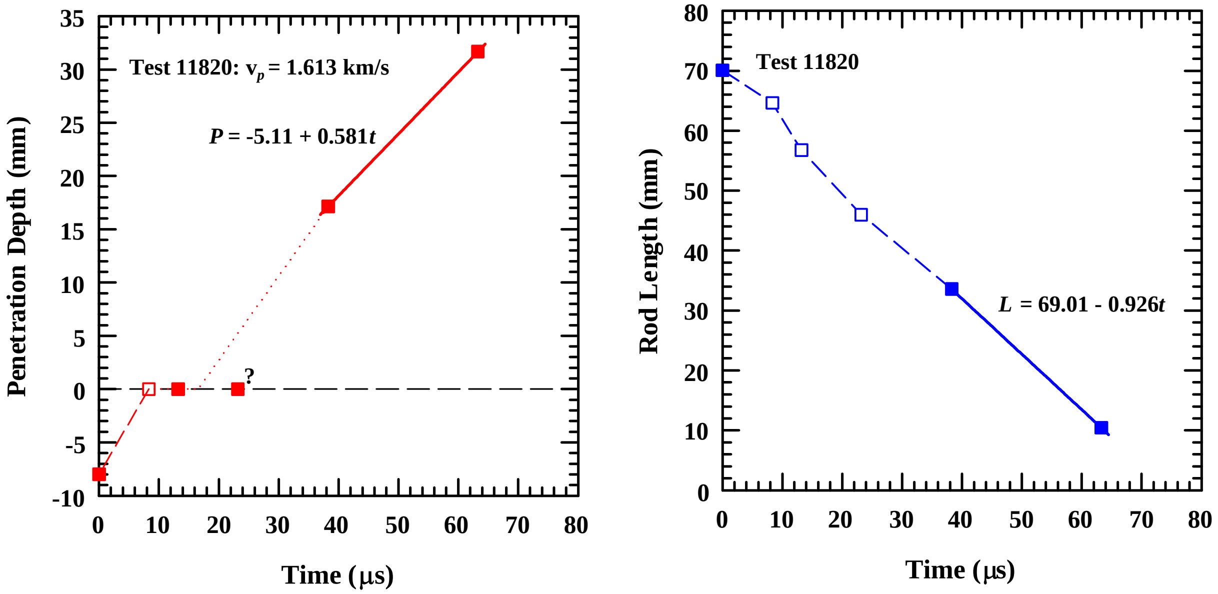

Figure A-64. Position and rod length vs. time for Exp. 11820: 60° with buffer, v_p = 1.613 km/s.

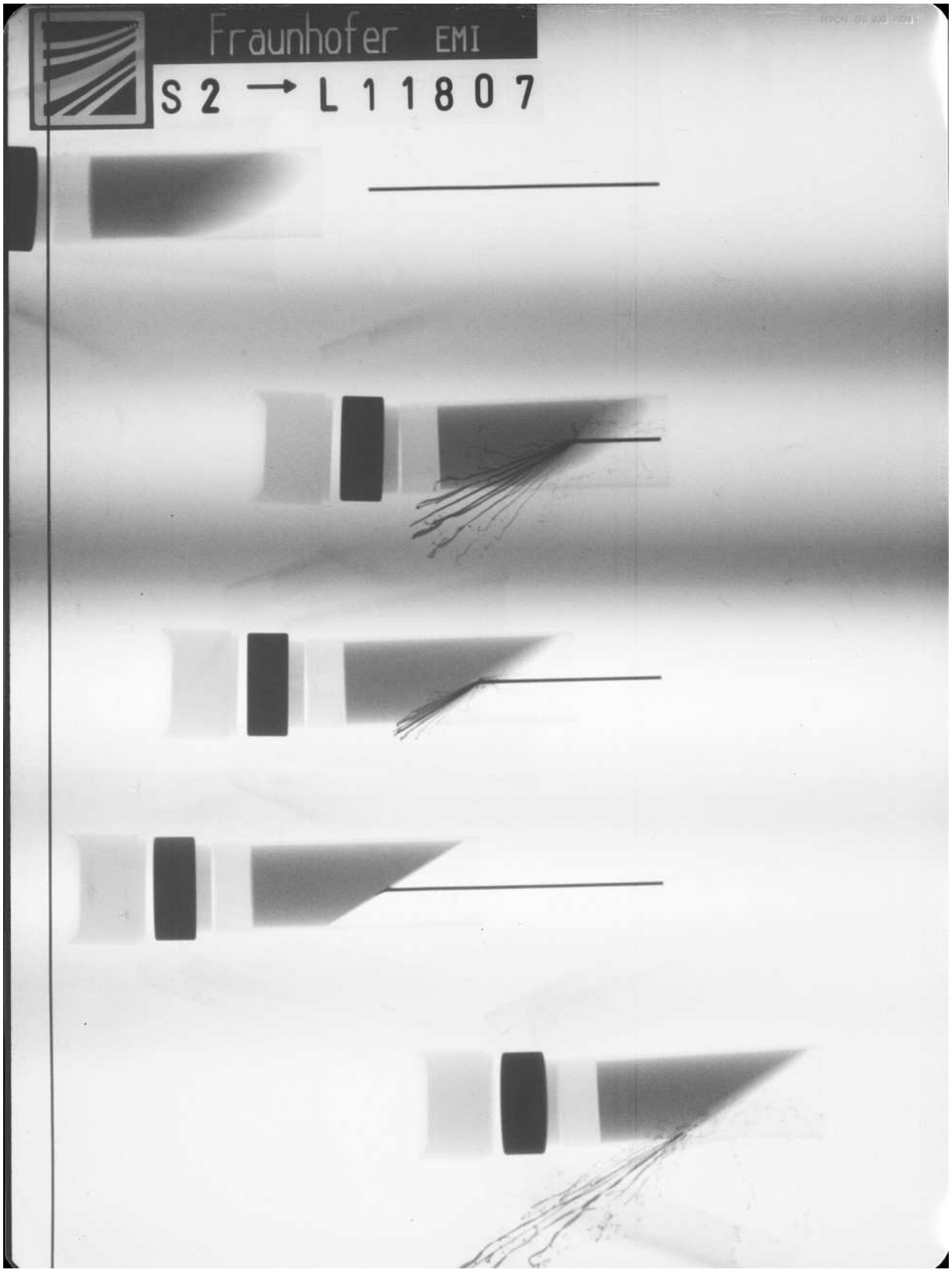

Figure A-65. X-ray picture for Exp. 11807: 60° bare, v_p = 0.921 km/s.

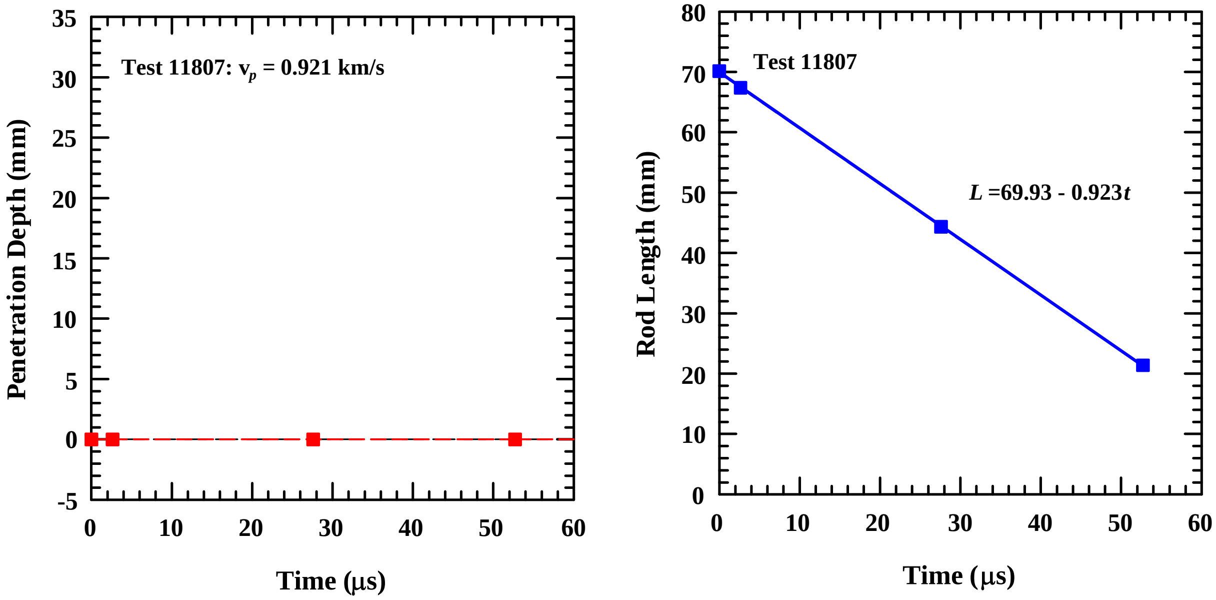

Figure A-66. Position and rod length vs. time for Exp. 11807: 60° bare, v_p = 0.921 km/s.

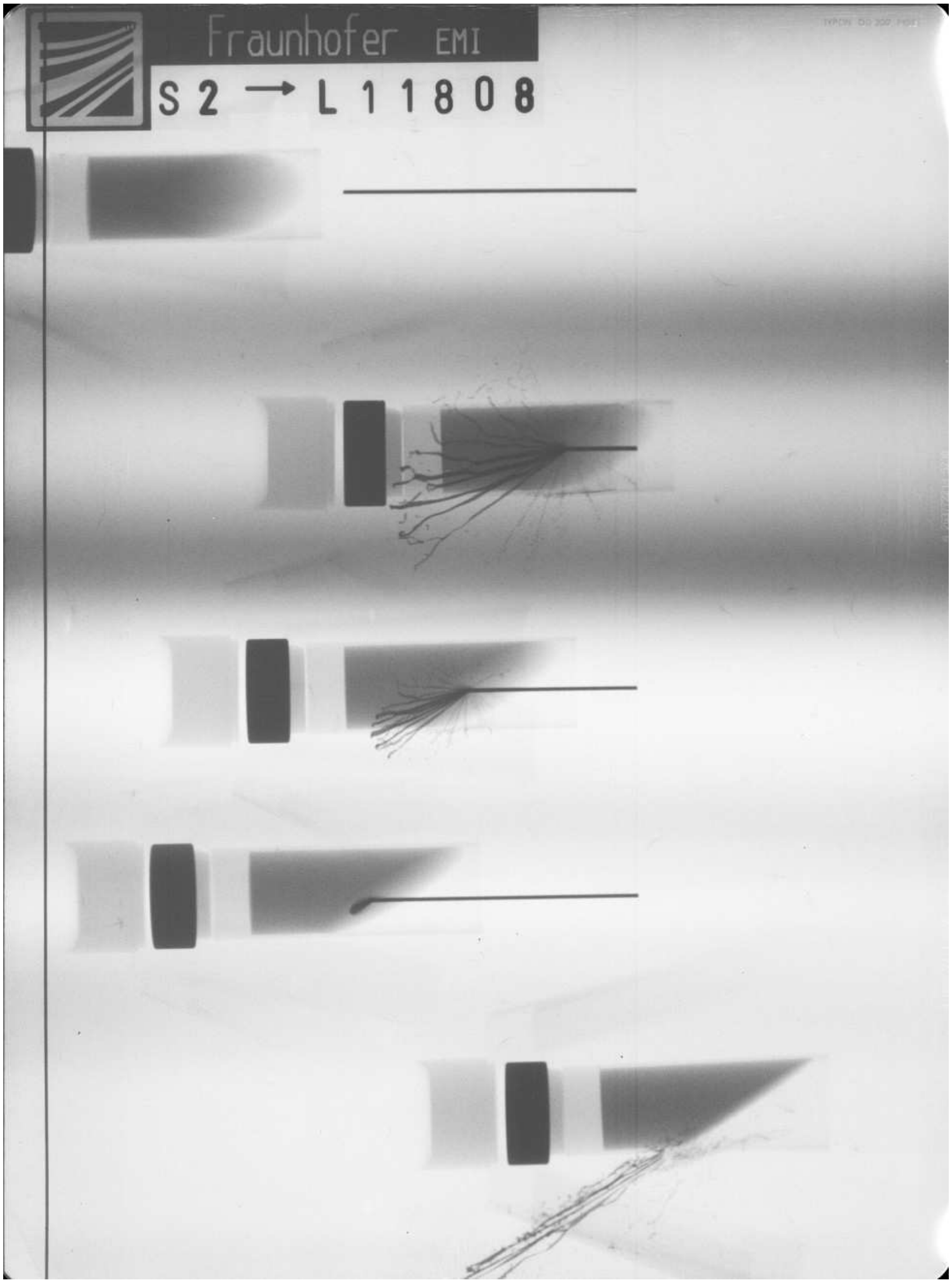

Figure A-67. X-ray picture for Exp. 11808: 60° bare, v_p = 0.932 km/s.

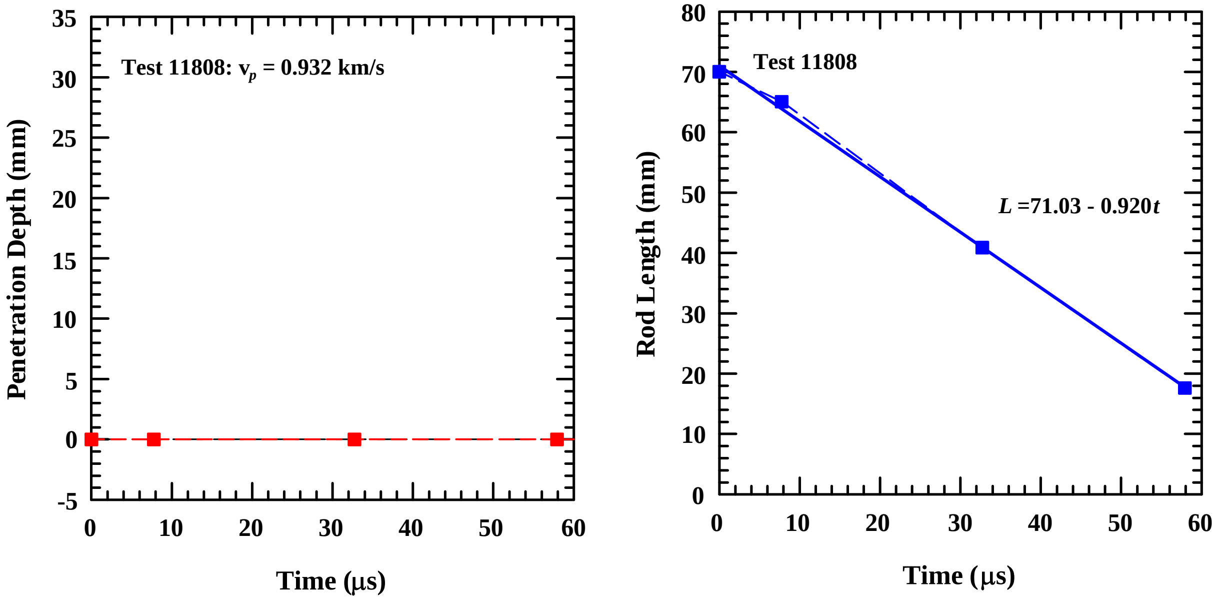

Figure A-68. Position and rod length vs. time for Exp. 11808: 60° bare, v_p = 0.932 km/s.

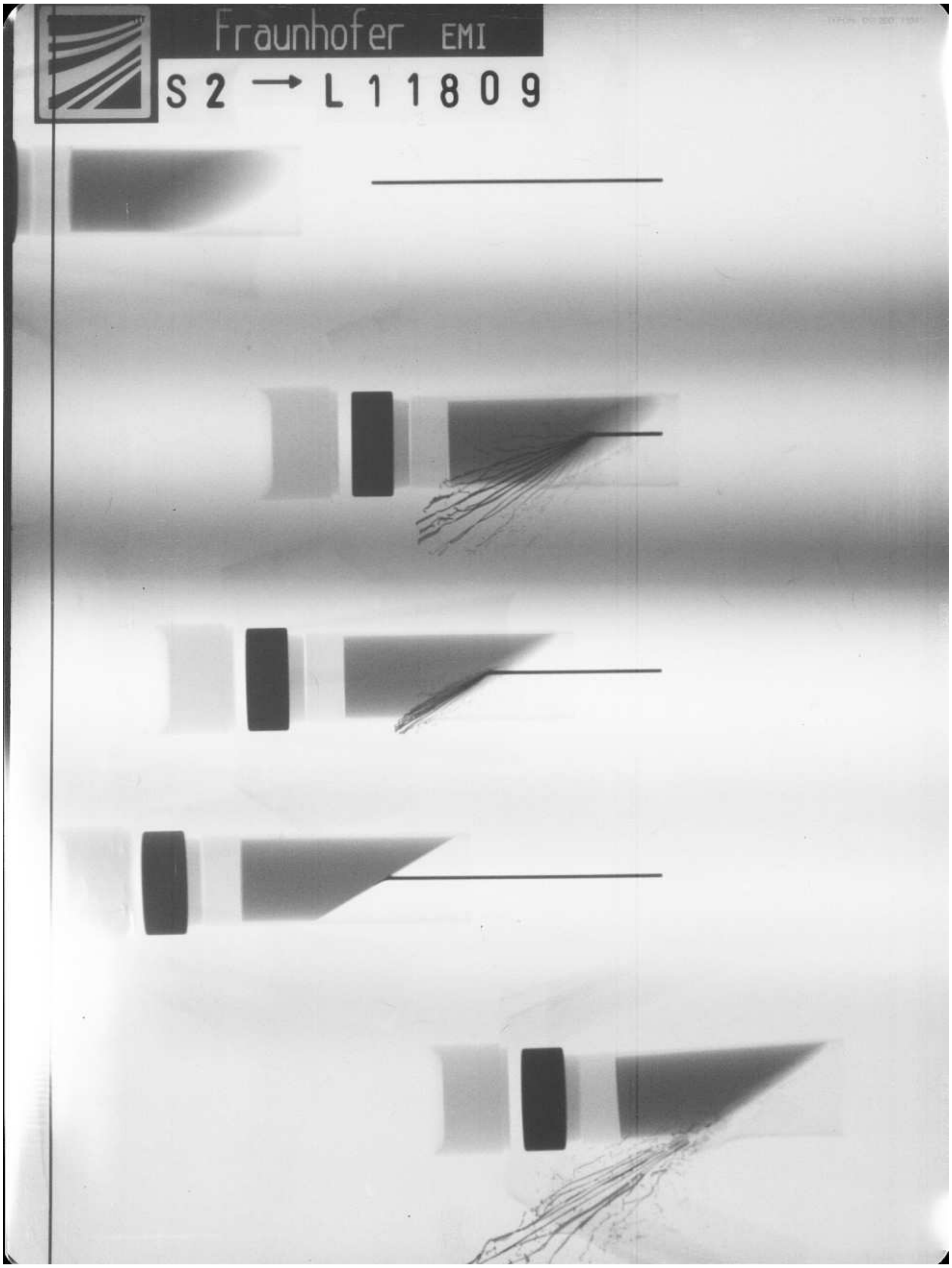

Figure A-69. X-ray picture for Exp. 11809: 60° bare, v_p = 1.008 km/s.

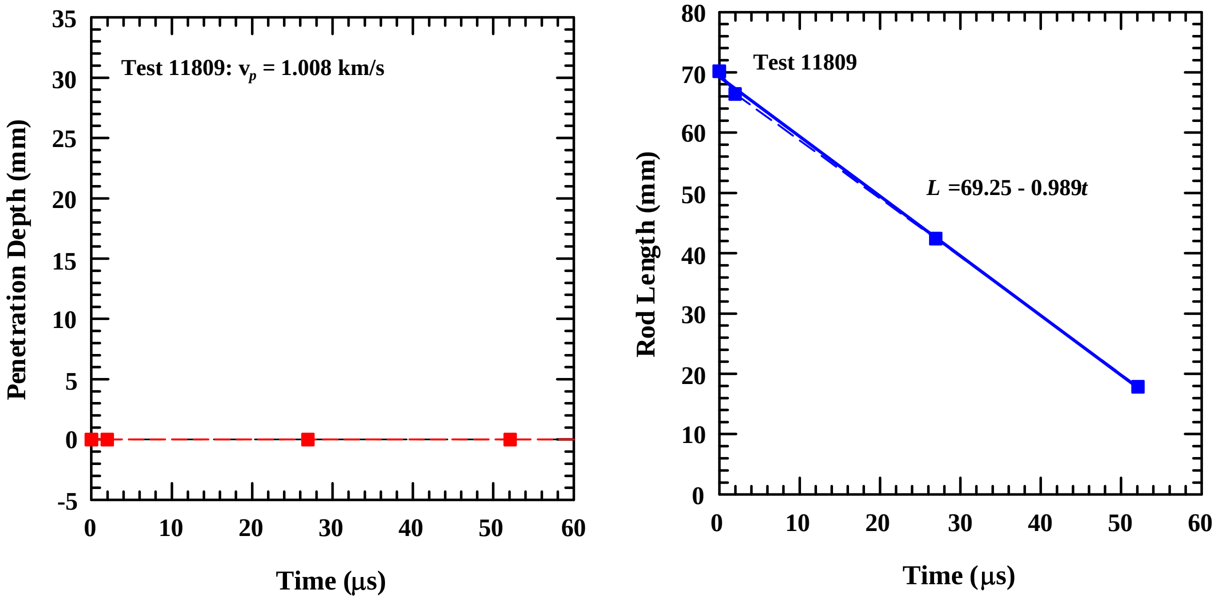

Figure A-70. Position and rod length vs. time for Exp. 11809: 60° bare, v_p = 1.008 km/s.

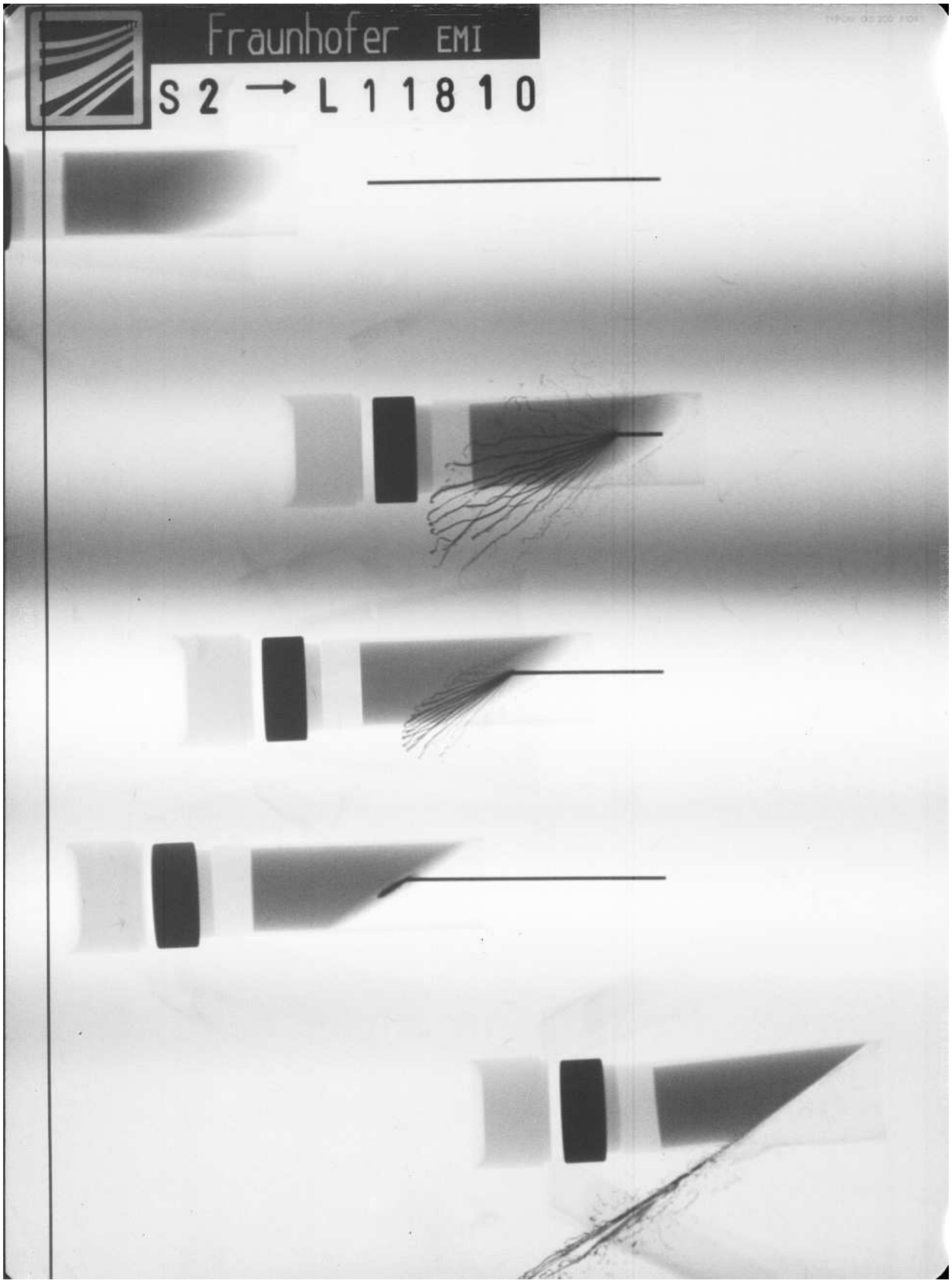

Figure A-71. X-ray picture for Exp. 11810: 60° bare, v_p = 1.067 km/s.

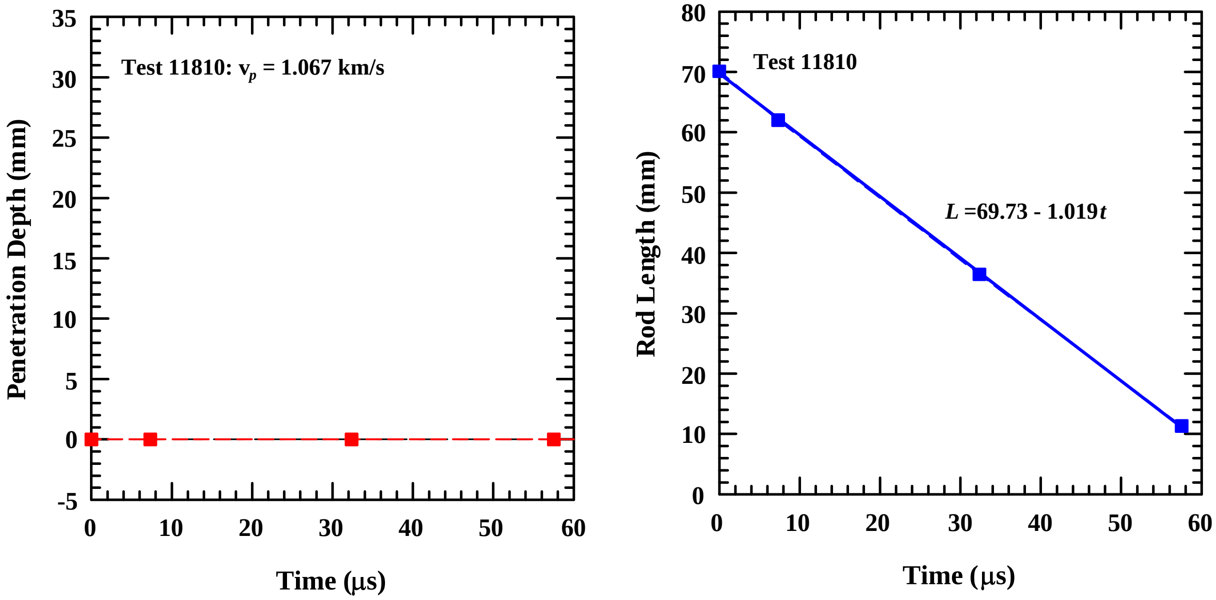

Figure A-72. Position and rod length vs. time for Exp. 11810: 60° bare, v_p = 1.067 km/s.

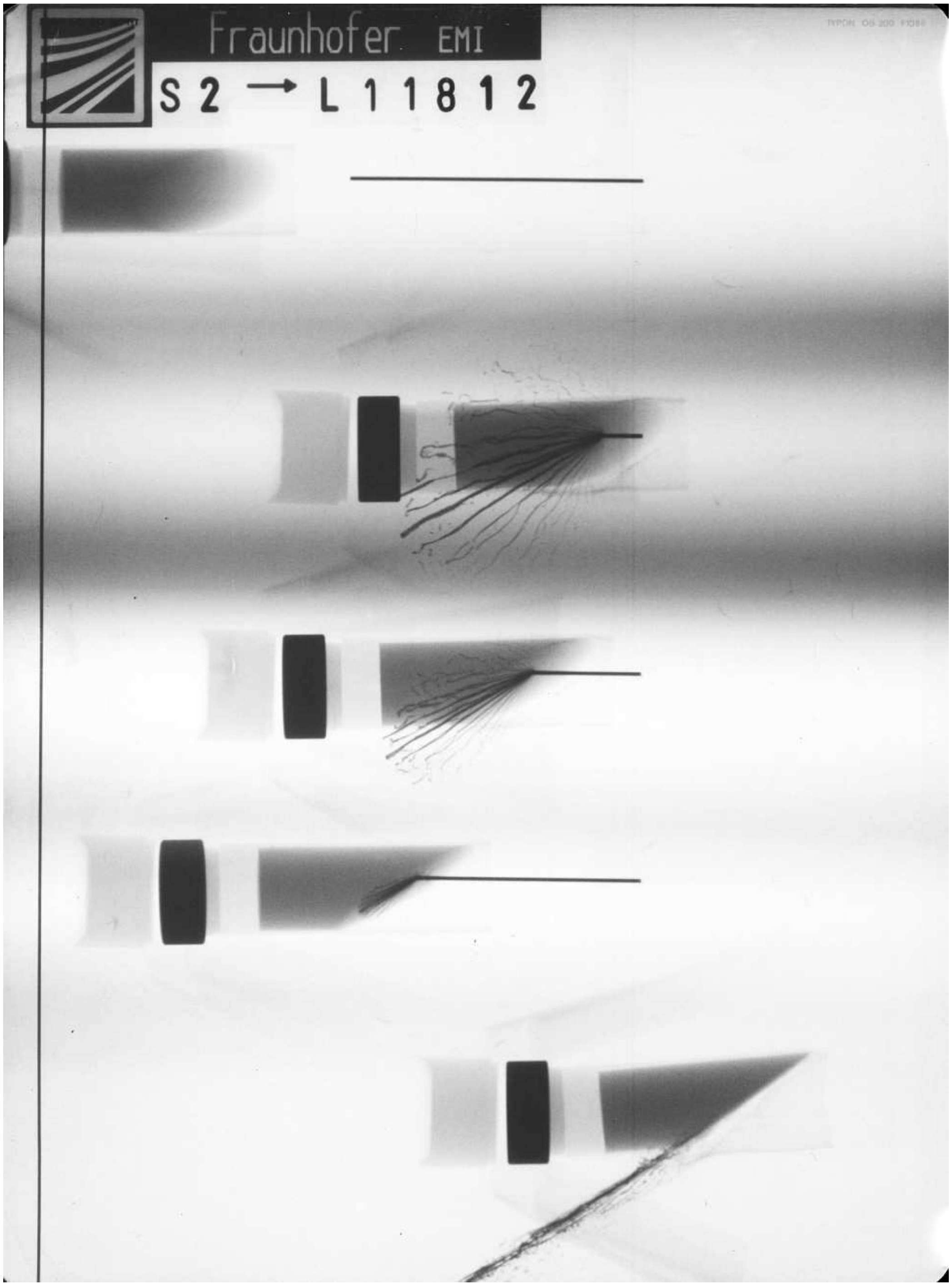

Figure A-73. X-ray picture for Exp. 11812: 60° bare, v_p = 1.162 km/s.

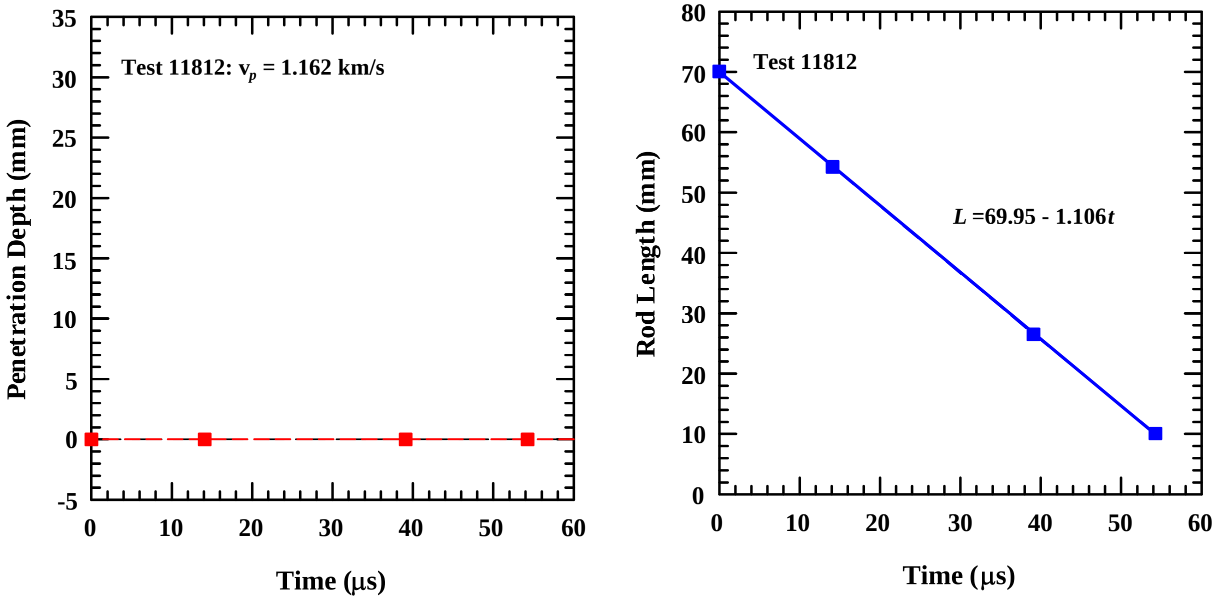

Figure A-74. Position and rod length vs. time for Exp. 11812: 60° bare, v_p = 1.162 km/s.

Figure A-75. X-ray picture for Exp. 11814: 60° bare, v_p = 1.408/ km/s.

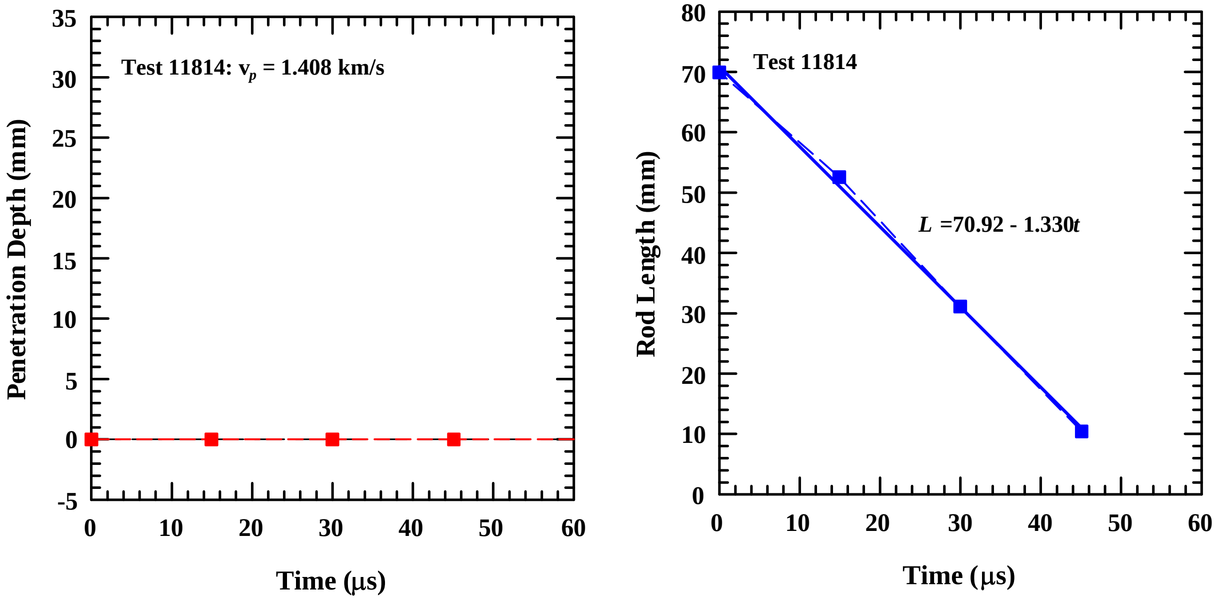

Figure A-76. Position and rod length vs. time for Exp. 11814: 60° bare, v_p = 1.408/ km/s.

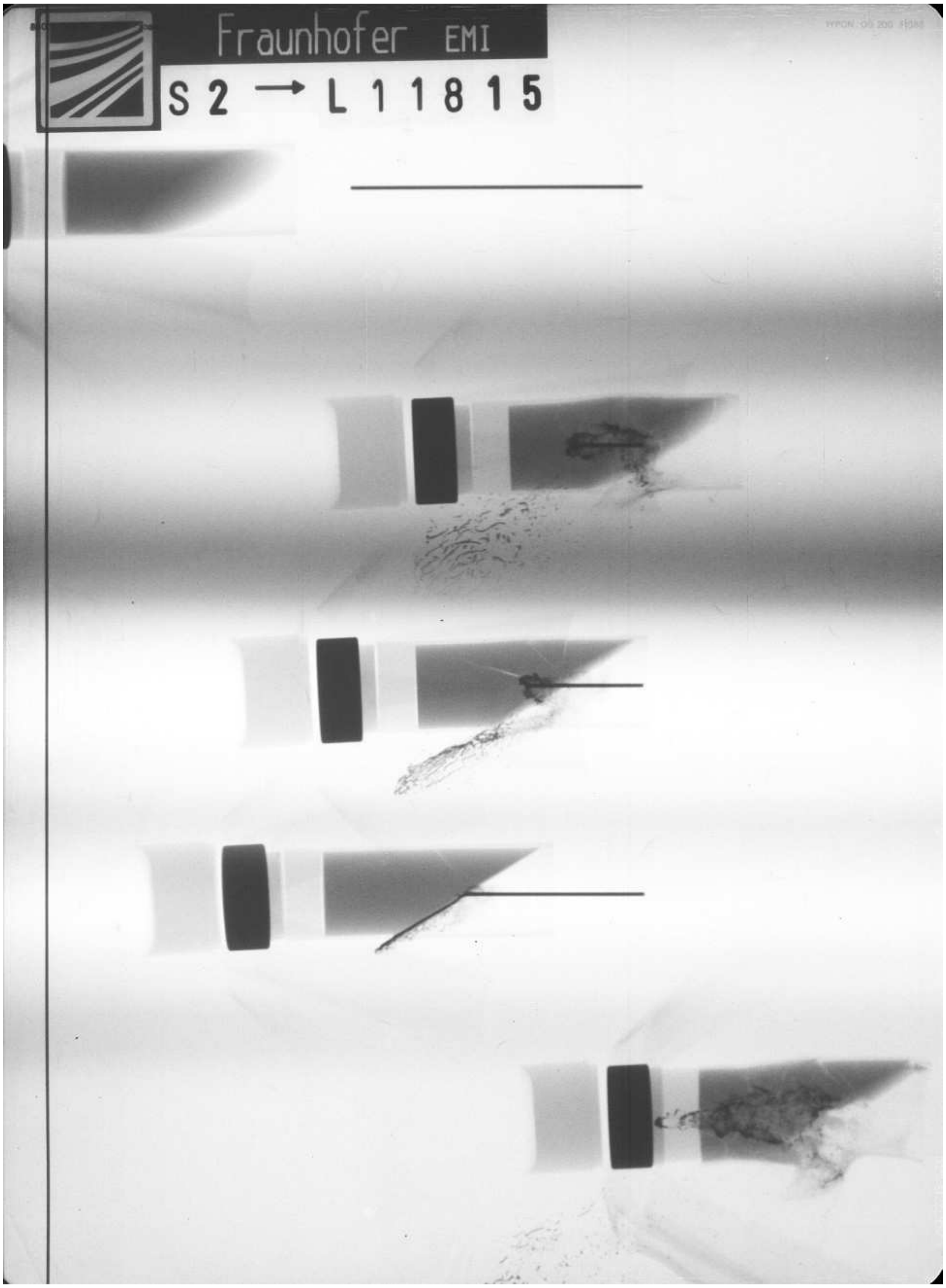

Figure A-77. X-ray picture for Exp. 11815: 60° bare, v_p = 1.515 km/s.

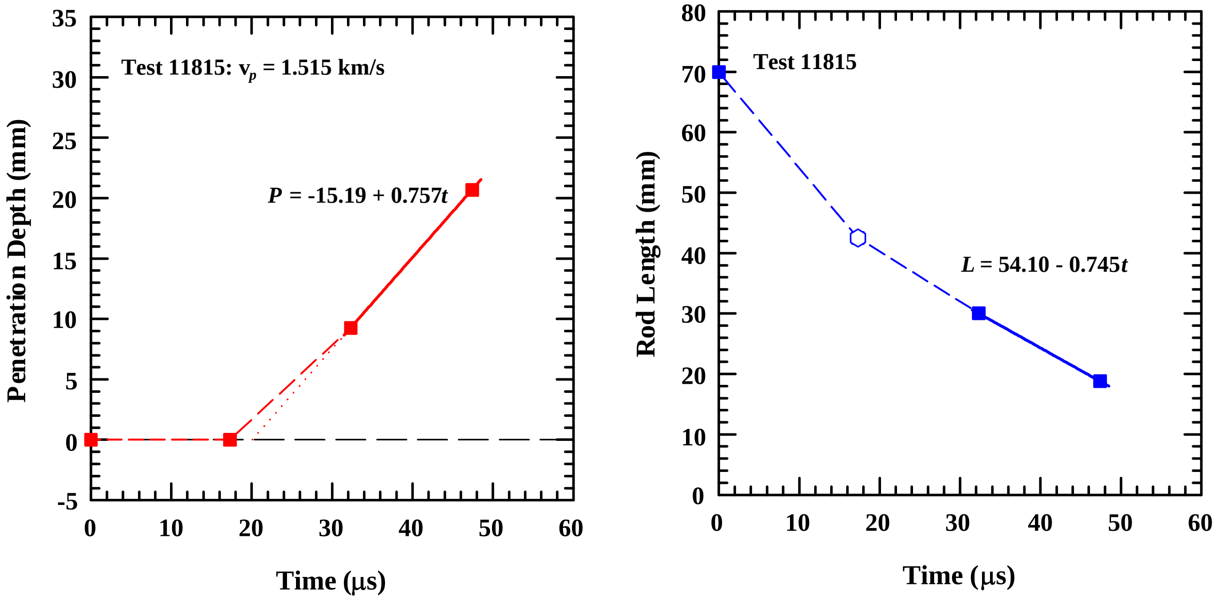

Figure A-78. Position and rod length vs. time for Exp. 11815: 60° bare, v_p = 1.515 km/s.

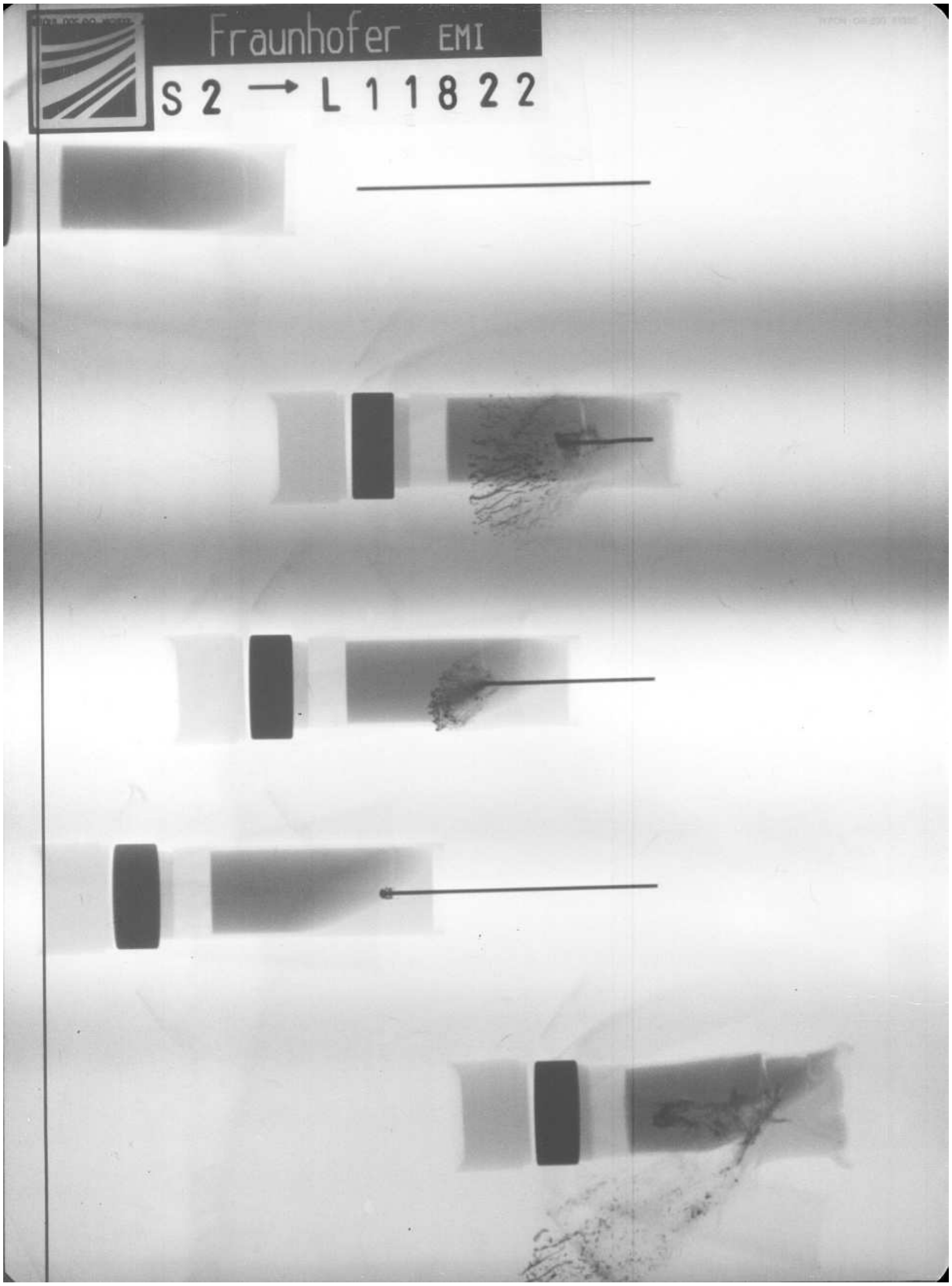

Figure A-79. X-ray picture for Exp. 11822: 60° bare with PC cover, v_p = 1.650 km/s.

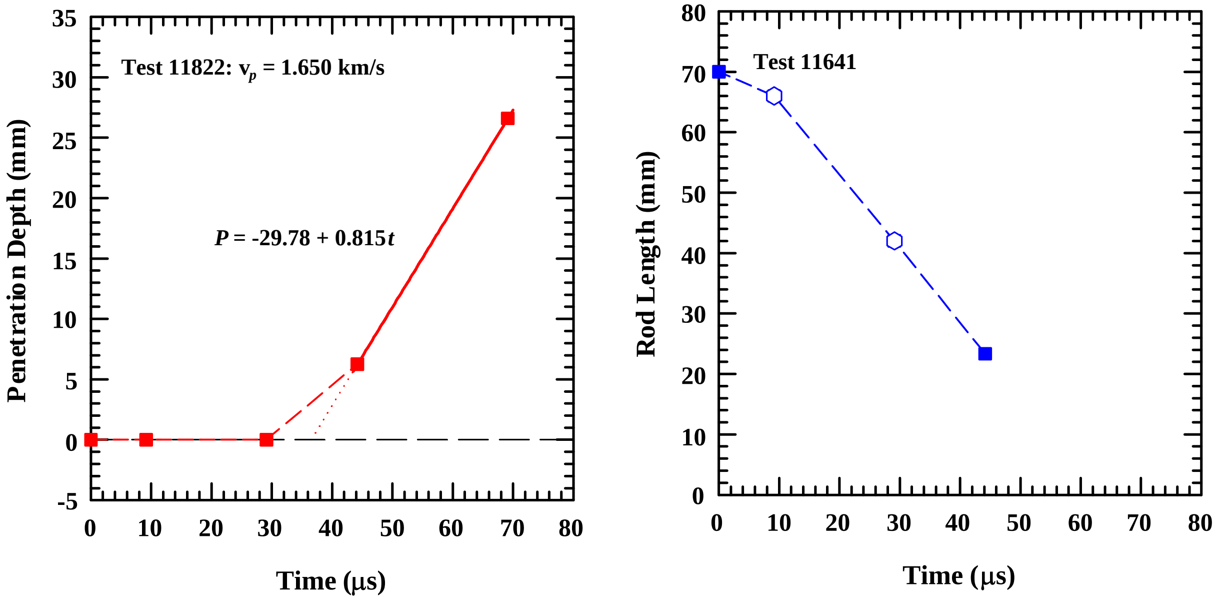

Figure A-80. Position and rod length vs. time for Exp. 11822: 60° bare with PC cover, v_p = 1.650 km/s.

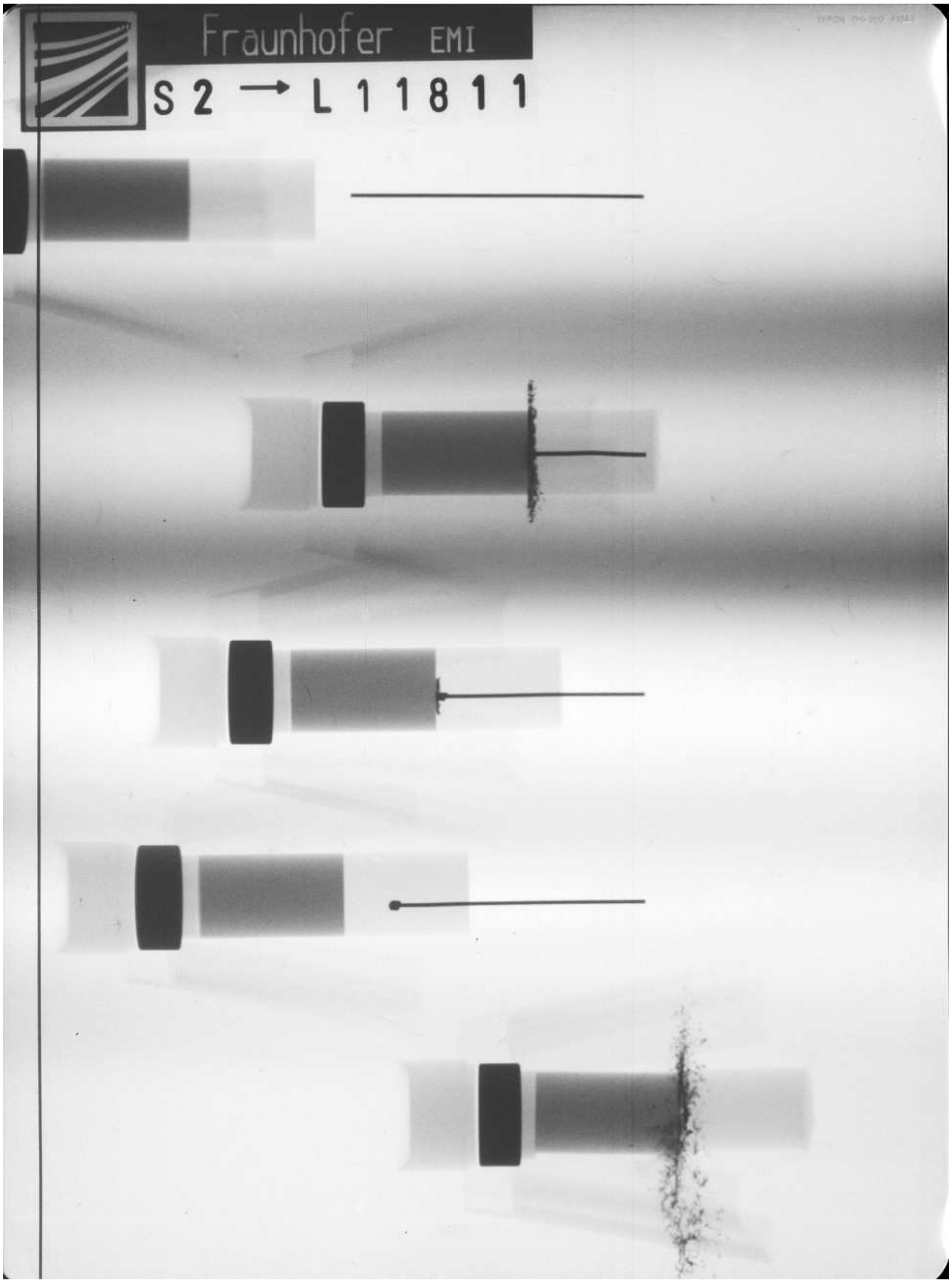

Figure A-81. X-ray picture for Exp. 11811: 0° bare with polycarbonate cover, v_p = 0.883 km/s.

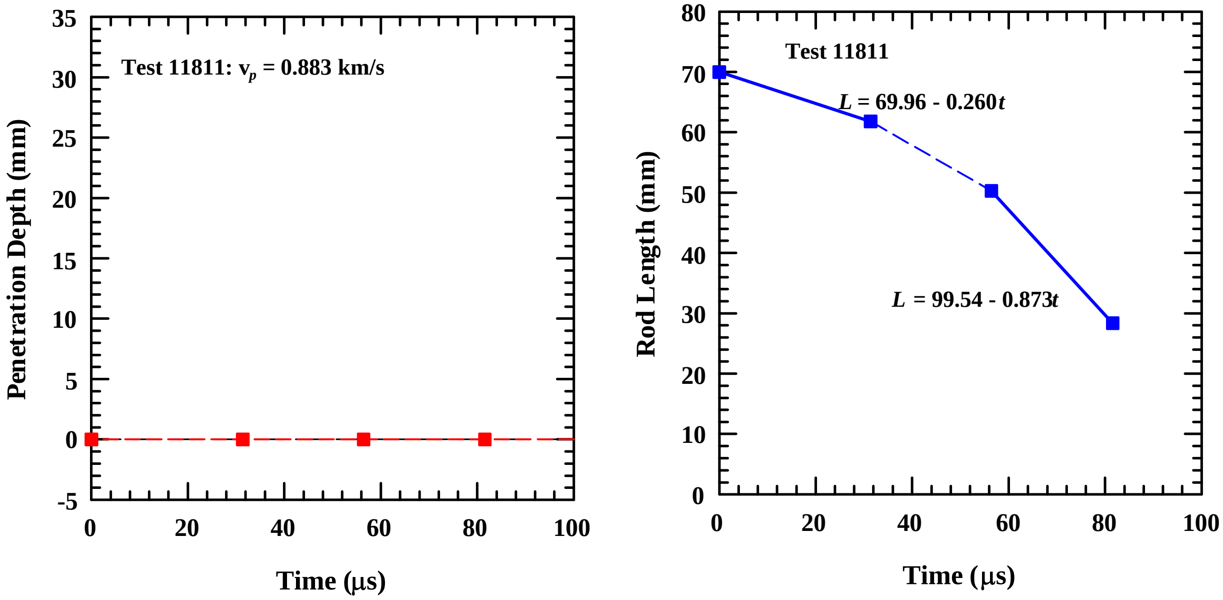

Figure A-82. Position and rod length vs. time for Exp. 11811: 0° bare with polycarbonate cover, v_p = 0.883 km/s.

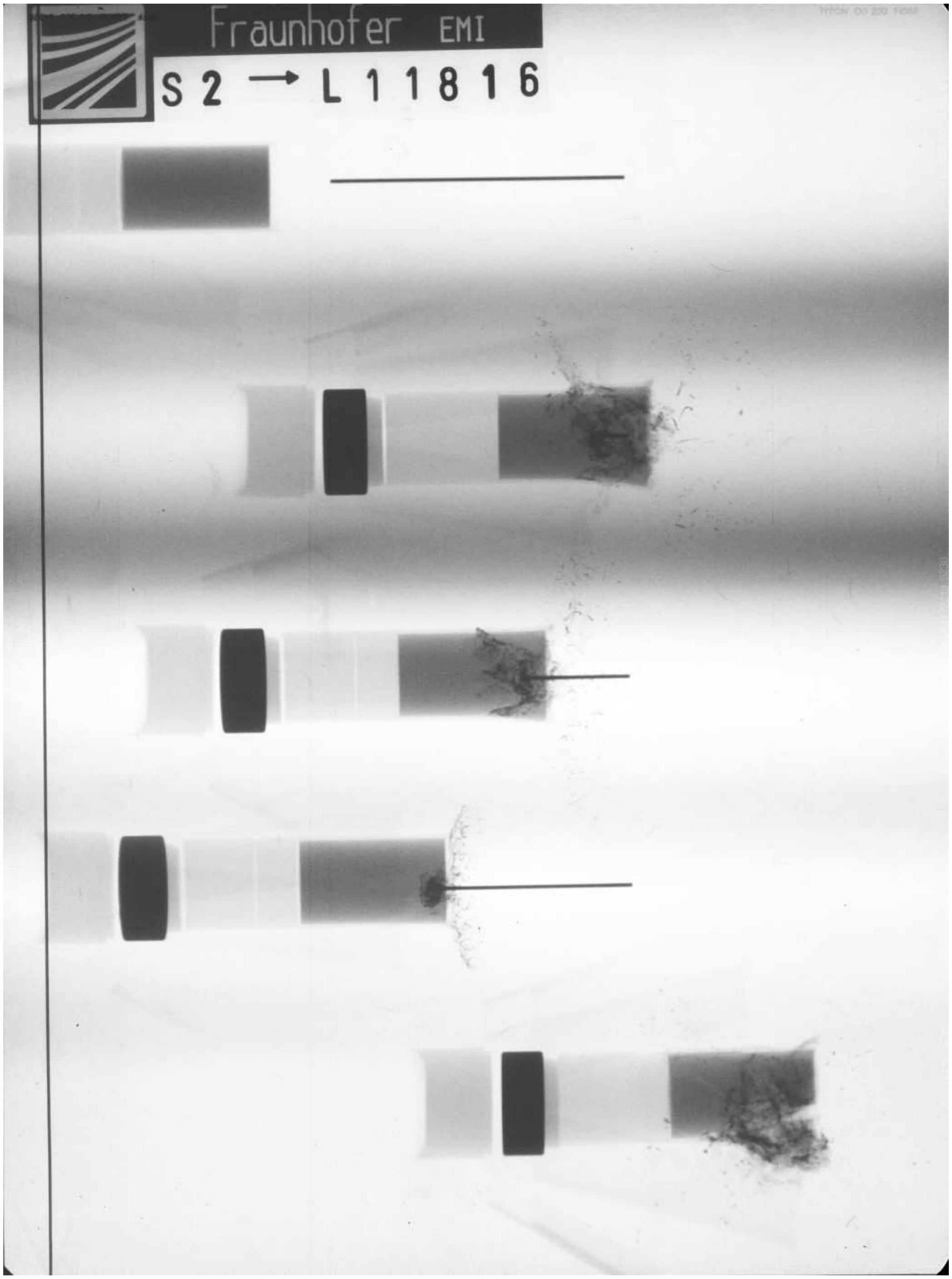

Figure A-83. X-ray picture for Exp. 11816: 0° bare, v_p = 0.978 km/s.

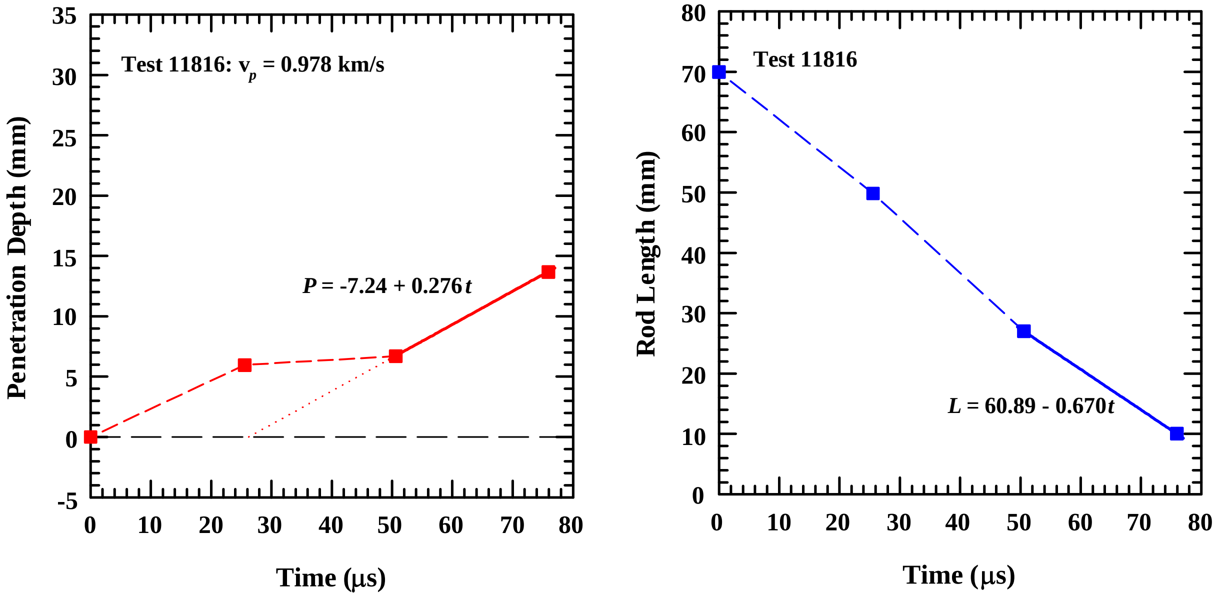

Figure A-84. Position and rod length vs. time for Exp. 11816: 0° bare, v_p = 0.978 km/s.